The Thesis Committee for Sawsan Almalki
Certifies that this is the approved version of the following Thesis:

The Value of Stratigraphic Well Data for a Geological Carbon Storage Project

APPROVED BY
SUPERVISING COMMITTEE:

Seyyed A. Hosseini , Supervisor

Carlos A. Uroza, Co-Supervisor

Brahim Hamouche, Reader

The Value of Stratigraphic Well Data for a Geological Carbon Storage Project

by

Sawsan Almalki

Thesis

Presented to the Faculty of the Graduate School of

The University of Texas at Austin

in Partial Fulfillment

of the Requirements

for the Degree of

Master of Science in Energy and Earth Resources

The University of Texas at Austin

December 2024

Dedication

هذا من فضل ربي

I dedicate this work to My Mama and Papa for always believing in me.

To My siblings (Laila, Khalid and Heyam), my backbone.

To My second family, my angels on earth.

To My better version of myself.

Acknowledgements

I would like to express my deepest gratitude to my supervisors Seyyed Hosseini, Carlos Uroza and Brahim Hamouche for their tremendous support, guidance, and patience throughout this project. A special thank you to Carlos Uroza for helping to find the data for this project., and to the anonymous landowner who kindly provided all the data that made this work possible. I am incredibly grateful to Saudi Aramco for sponsoring and supporting this Master's degree.

I am grateful to the whole BEG-GCCC group, especially Sue Hovorka for always supporting students and sharing your vast knowledge in CCS, and Alex Bump for helping with soft skills. Thank you all for your friendly connections and unwavering assistance.

My sincere thanks go to William Wang Zhicheng and Romal Ramadhan for their help with dynamic modeling and simulations, to Robin Dommisse for his exceptional guidance in time-depth conversion and 3D fault modeling, and to the anonymous geophysicist, assigned by landowner, who worked the initial horizon and fault interpretation.

I am forever thankful to my loved ones for their unwavering emotional support, continuous encouragements, love and care. This research would have not been possible without everyone's contributions.

Abstract

The Value of Stratigraphic Well Data for a Geological Carbon Storage Project

Sawsan Almalki, M.S.

The University of Texas at Austin, 2024

Supervisors: Seyyed Hosseini, Carlos Uroza, and Brahim Hamouche

This study demonstrates the application of Value of Information (VOI) analysis during the pre-injection phase of a geological carbon storage (GCS) project in the Frio formation, South Texas. VOI analysis serves as a tool to calculate the dollar amount it should be paid for a test to reduce geological uncertainty given a test accuracy. This research integrates 3D seismic data, legacy well information, and geological insights from nearby fields. The workflow includes: (a) seismic interpretation for structural modeling, (b) well-log correlation to define stratigraphy, (c) petrophysical analysis to create a static model, and (d) dynamic simulations to predict CO_2 plume behavior, pressure front movement, storage capacity, and the area of review (AoR) definition. Geological uncertainties were identified to mitigate technical and financial risks, thereby reducing liability. The primary uncertainty in this analysis stems from data scarcity within the Area of Interest (AoI). To address this, multiple models with varying heterogeneity and porosity were developed for VOI assessment, storage capacity estimation, and business feasibility analysis for a Direct Air Capture (DAC) project. The research investigates the likelihood for the formation storing more than 1 $MtCO_2$ within the AoI and assesses the value of

drilling a stratigraphic well to reduce geological uncertainties. Based on this analysis and assuming a test accuracy of 100%, $4.86 million is the maximum amount the operator should pay for drilling a stratigraphic well. Although assuming a 100% accuracy may be idealistic, it provides a clear benchmark for capping the maximum amount it should be paid for any given test. Additionally, the study examines the impact of test accuracy variations, concluding that tests with an accuracy higher than 80% add value to the decision-making process. This research fills a critical gap in the current understanding of VOI in GCS studies, particularly concerning stratigraphic well data. Although the VOI analysis is specific to the site and time frame studied, it establishes a VOI framework that can be applied to decision-making in other CO_2 storage projects.

Table of Contents

List of Tables 10

List of Figures 11

Chapter 1: Introduction 17

1.1 Previous work 17

1.2 Carbon Capture and Storage 18

1.3 Value of Information 19

1.4 Geologic Setting 21

1.5 Study Area and Dataset 28

1.6 Research Relevance 29

1.7 Research Goals 30

1.8 Project Workflow 31

Chapter 2: Reservoir Characterization of the Storage Site 33

2.1 Introduction 33

2.2 Structural Framework 37

2.3 Stratigraphic and Depositional Framework 46

2.4 Reservoir Quality Analysis 49

Chapter 3: 3D Geocellular Modeling for Upper Frio Zone 60

3.1 Reservoir 3D Geomodeling 60

3.2 Petrophysical Property Modeling 68

3.3 Uncertainty Analysis 74

Chapter 4: CO_2 Storage Capacity Analysis- Simulation Study 81

4.1 Dynamic Reservoir Modeling 81

4.2 Simulation Results And Discussion 86

Chapter 5: Value of Information....90
5.1 VOI Case....90
5.2 Decision Analysis....91
5.3 Value of Stratigraphic Well Information (VOI):....93
5.4 Value of Perfect Information (VOPI)....96
5.5 Value of Imperfect Information....99
5.6 Sensitivity Analysis....101
Chapter 6: Discussion and Future Work....102
6.1 Value of Information (VOI)....102
6.2 Site Characterization and Modeling....103
Chapter 7: Conclusions and Recommendations....106
Appendices....108
Appendix A....108
Appendix B....109
Appendix C....110
Appendix D....111
References....113

List of Tables

Table 1: Dataset of the study area.....29
Table 2: Available well logs 37
Table 3: Summary of input data available for constructing 3D geologic modeling.....61
Table 4: 3D Grid resolution parameters.....62
Table 5: Basecase variogram ranges for property modeling 71
Table 6: B+ variogram ranges for property modeling 71
Table 7: B++ variogram ranges for property modeling.....72
Table 8: Fluid Properties.....82
Table 9: Maximum injection pressure for CCS_well_Inj_1 and CCS_well_Inj_2. 84
Table 10: The outcomes of the AoR definitions in acre and SQFT for each realization...89

List of Figures

Figure 1: Northern Gulf (US) margin deposodes, sediment influx, calculated as total grain volume, and continental margin accretion rates 22

Figure 2: NW-SE cross section of Texas Gulf Coast basin, showing basin-margin faults (modified from Ewing, 1991) 22

Figure 3: Diagrammatic dip cross section showing formation of successive growth-faulted subbasins (Corpus Christi, Texas). Each subbasin is filled with genetically similar but diachronous depositional systems (from Brown et al, 2004) 23

Figure 4: Paleogeographic map of the Oligocene Frio deposode. Depositional system outlines and shelf edge reflect their positions at maximum progradation. Arrows point to the four major fluvial–deltaic axes: Mississippi, Houston, Rio Grande, and Rio Bravo. (GBDS, 2019).....25

Figure 5: Main sediment sources, basins and uplift, and depositional systems in the northern Gulf of Mexico during the late Oligocene (modified from Galloway and others, 2000). The Rio Grande embayment includes the area of interest.....26

Figure 6: Map displaying potential for high-quality, deep reservoirs (>3350 m, 11,000 ft) in Lower Tertiary strata along the Texas Gulf Coast. Good indicates permeability values commonly greater than 20 mD. Marginal indicates permeability values generally less than a md (from Loucks et al. 1984) 28

Figure 7: Size of the area in USft (~56,000 ft by 50,670 ft) about an area of 232 km^2.....34

Figure 8: Well-log correlation in the AOI, showing the total storage section (Frio Top-Frio FS7 marker) and the targeted section (Frio Top-Frio FS1 marker). The correlation line shown on the map 35

Figure 9: The SP and GR logs of the wells show normalization within the zone of interest (Upper Frio Zone). The SP logs are denser due to the higher number of wells with SP than the GR log. We ignore the outliers in the SP log, limiting the scale between 0 to -1 36
Figure 10: Seismic interpretation of Top Frio to base of Frio storage section (i.e., FS7) 38
Figure 11: QC visualization - The displayed surfaces on the Inline and Xline seismic are the depth grids intersecting the well tops at wells A and B. 39
Figure 12: Seismic Inline with some of the faults in AOI. The target zone between pink and green horizons (Top Frio – FS1), the red arrow indicates the total storage section. 41
Figure 13: Map view of the faults with the wells' location 42
Figure 14: Frio Top structure map tied with its correspondent well pick as the input data in the correction column to define the value in the velocity model 44
Figure 15: Map in time vs depth of the Top Frio, showing consistency following time-depth conversion process 45
Figure 16: Well cross-section showing the main three key wells - the highlighted zone is the Upper Frio Zone, the target injection interval. The datum is the Anahuac shale. 47
Figure 17: Stratigraphic cross-section of the Frio formation in the AOI, showing the multiple reservoir units. We are only focusing on the Upper Frio interval as the target injection interval for this study. Wells in cross-section contain the most complete suite of log curves 48
Figure 18: Highlighting the three key wells in the AOI where property modeling and VOI analysis was focused on 53

Figure 19: PHIE vs Vclay from key well no.1 to get the linear relationship for PHIE_base.....54
Figure 20: Key well-1 displaying sonic porosity (PHIS) compared to PHID_SONIC (regression relationship between density porosity and sonic). PHIS was used instead for better results.....55
Figure 21: PHIE_B+ case: PHIE vs Vclay plot from key well no.2 to get the linear relationship for PHIE_B+ 56
Figure 22 – PHIE_B++ case: PHIE vs Vclay from key well- 3 to get the linear relationship for PHIE_B++.....57
Figure 23: (a) Poro-Perm transform from a nearby field applied in the study (b) Two wells outside the AOI with core plug Poro-Perm with a lower R^2 (scattered and uncertain) that was not used 59
Figure 24: Boundary polygon indicating the extend of the AOI used for modeling.....60
Figure 25: Top Frio depth map, showing the 35 faults included in the geologic modeling 62
Figure 26: Frio top (above) and FS1 (below) horizons in 3D structure model. The blue represents deeper depth and the green up to red color represent shallower depth.....63
Figure 27: The 35 faults in the AOI showing the regional growth fault on the west 65
Figure 28: Before and after adjusting the horizon line. Adjustment of the horizon line circled in red 66
Figure 29: Target injection zone visualization of the Top Frio - Frio FS1in dark grey. This is the structural model under Structural Framework in Petrel (Geospace view).....67

Figure 31: The resulted upscaled log PHIE_base of the key well- No1 consistent with its input well log. The blue log is the PHIT. The datum is flattened in Anahuac shale. 69
Figure 32: Normal score transformation performed in Petrel modeling background for running stochastic simulation (property modeling). The histogram on the right shows the transformed values (standardized to follow a normal distribution with a mean of 0 and standard deviation of 1) 70
Figure 33: The effective porosity with low and high variogram ranges in the base case (Left histogram: base variogram at 20,000 ft, middle: low at 15,000, and right: high at 25,000 ft) 73
Figure 34: The resulted effective porosity model displayed as an extracted log (in the far right for the base case model) from the 3D grid in Petrel. Well-2 and well-3 are honoring its total porosity instead of PHIE when stochastically modeling in 3D property modeling since these two wells were not sampled in the base case model. The datum is flattened on Anahuac shale. 74
Figure 35: PHIE_basecase with variogram range (base at 20,000ft, low at 15,000ft and high at 25,000ft respectively).....76
Figure 36:PHIE_ B+ with variogram range (base at 20,000ft, low at 15,000ft and high at 25,000ft respectively).....76
Figure 37: PHIE_B++ with variogram range (base at 20,000ft, low at 15,000ft and high at 25,000ft respectively) 77
Figure 38: PHIE_basecase with low and high porosity respectively based on +/- 0.08 std from the mean with the same base variogram at 20,000 ft 77

Figure 39: PHIE_B+ with low and high porosity value based on +/- 0.06 std from the mean with the same base variogram at 20,000 ft.....78
Figure 40: PHIE_B++ low and high porosity value based on +/- 0.05 std from the mean with the same base variogram at 20,000 78
Figure 41: Basecase with porosity and variogram combined.....79
Figure 42: B+ with porosity and variogram ranges combined 79
Figure 43: B++ with porosity and variogram ranges combined.....80
Figure 44: Net pay map showing bullseyes where the CCS injection wells were placed 83
Figure 45: CO_2 Rate at the standard condition and Well Bottom-hole Pressure for the base case with data analytics (BC V). CCS_well_Inj_1 is set at 4496 psi and CCS_well_Inj_2 is at 4358 psi with different perforation layers. 85
Figure 46: Cumulative CO_2 in red and CO_2 Rate in green at standard conditions for the base case scenarios in data analytics (low, base, high variogram values). The reason why the cumulative CO_2 is not a straight linear line is due to the different perforation layers, injecting at 4e+06 ft^3/day for the first ten years, then at 4.5e+06 ft^3/day for the five years, then at to 6.24+06 ft^3/day for the last five years of the injection period 86
Figure 47: CO_2 plume model after 20 years. The plume is touching the minor faults that are considered not critical to the storage capacity and would not impact leakage for the study. The bar legend indicates the CO_2 saturation.....87
Figure 48: AoR delineation for all 15 realizations.....88
Figure 49: The outcomes of the cumulative storage capacity in tCO_2 for each realization for 20 years (total of 15 realizations).....89

Figure 50: The influence diagram (or relevance) in the assessed form (prior belief).....92
Figure 51: The influence diagram (or relevance) in the inferential form (posterior) 92
Figure 52: Bootstrap distribution of the 15 realizations (storage capacity predictions) 93
Figure 53: Prior probability (without additional information) of the storage capacity greater than 1MtCO_2. The circle represents uncertainty.....94
Figure 54: Decision tree without stratigraphic well (VOI). The rectangular represents decision, and the circle represents uncertainty. 96
Figure 55: Information gathering relevance (VOPI) 97
Figure 56: Decision tree of value of perfect information (VOPI) 98
Figure 57: Probability tree of storage capacity 100
Figure 58: Decision tree with value of imperfect information (VOII) 101
Figure 59: Sensitivity of operator's VOI to Test Accuracy for the storage capacity 101

Chapter 1: Introduction

1.1 PREVIOUS WORK

Carbon capture and storage (CCS) technologies have advanced significantly, especially as the pressure to reduce carbon emissions intensifies. There is an increasing demand for effective and cost-efficient CO_2 sequestration solutions that enable companies to achieve their emission targets (DePaolo et al., 2013). However, challenges remain in identifying suitable and safe geologic sites, particularly concerning storage capacity and risk assessment.

In the last years, considerable attention has been focused on the use of Value of Information (VOI) framework for reducing uncertainties and optimizing decision-making in geological and carbon storage projects (add references).

Eidsvik et al. (2015) highlighted the integration of VOI analysis with spatial modeling, demonstrating its relevance in domains like geology and environmental systems. Similarly, Puerta-Ortega et al. (2013) applied VOI-based methodologies to evaluate the value of permeability data in a CCS project, illustrating how reduced uncertainty can improve subsurface characterization and project outcomes. Sato (2011) explored VOI applications for monitoring CO_2 storage, emphasizing how advancements in information accuracy can directly influence decision quality.

Elvaretta (2021) investigated VOI in CO_2 sequestration projects by combining Monte Carlo simulations with regression techniques to assess decisions under reservoir uncertainties, focusing on maximizing storage efficiency and minimizing risks like leakage. Bratvold et al. (2009) and Bickel (2015) underscored the need to contextualize VOI within specific decision frameworks to ensure effective resource allocation.

Additionally, Allen et al. (2018) examined the influence of geological uncertainties, such as porosity and fault transmissibility on CO_2 storage capacities in saline aquifers.

All in all, Geological Carbon Storage (GCS) projects involve significant uncertainties regarding subsurface characteristics and the behavior of CO_2 once injected. VOI method has been a critical framework for decision analysis in complex projects mentioned above with significant uncertainties.

1.2 Carbon Capture and Storage

Carbon capture and sequestration is a "reliable and affordable" technology to mitigate climate change (IPCC et al., 2023). The Gulf Coast Carbon Center (GCCC) is a global leader in research that develops technologies for effectively monitoring CO_2 in the subsurface, as well as understanding the ideal subsurface conditions for CO_2 storage. Some of GCCC's studies have focused on estimating storage capacity and other critical factors to secure the injected CO_2 and prevent its release into the atmosphere and oceans.

CCS is an option to reduce emissions from large-scale fossil-fuels energy and other industry sources, provided geological storage is available. It involves capturing CO_2 from industrial sources or directly from the atmosphere using DAC (IPCC et al., 2023). CO_2 capture and subsurface injection is a mature technology for gas processing and enhanced oil recovery. However, CCS is less mature in the power generation sector, as well as in cement and chemicals production, where it is a critical mitigation option (IPCC et al., 2023). The technical geological storage capacity is estimated to be around 1000 $GtCO_2$, which exceeds the CO_2 storage requirements through 2100 to limit global warming to 1.5°C (IPCC et al., 2023). Regional availability of geological storage could be a limiting factor. On the other hand, the US has significant geological storage capacity, estimated between 3,000 to 8,600 $GtCO_2$, suggesting storage capacity is unlikely to be a limiting factor. However, economic potential might be lower (Dual Challenge, 2021). Properly

selected and managed geological storage sites are estimated to permanently isolate CO_2 from the atmosphere (IPCC et al., 2023).

Generally, effective CO_2 storage requires robust regulatory frameworks, public support, and technological advancements to address challenges like induced seismicity, injectivity, and long-term monitoring.

1.3 VALUE OF INFORMATION

1.3.1 Value of Information (VOI)

The concept of Value of Information (VOI) in decision analysis evaluates the benefits of acquiring additional information before making a decision. It helps to distinguish between useful and necessary information gathering by assessing whether the new information will likely change the decision that would be made without it (Bratvold et al., 2009). VOI assigns values based on how much information improves decision making, rather than simply reducing uncertainty or boosting confidence (Bratvold et al., 2009). VOI analysis involves specifying potential information-gathering activities, quantifying the accuracy of this information, modeling decisions influenced by the information, and finally determining whether the improvement in decision-making justifies the cost of obtaining the information (Bickel, 2015).

For an information-gathering activity to add value, it must meet these four criteria (Howard & Matheson, 2005):

- **Observable**: The results must be measurable
- **Relevant**: The results must influence the understanding of the decision at hand
- **Material**: The information must have the potential to change decisions
- **Economic**: The value gained must exceed the cost of obtaining the information

The VOI for a specific uncertainty $\boldsymbol{x}$ and a decision $\boldsymbol{a}$ is defined as the amount at which a decision maker is equally satisfied with either obtaining the information or making the decision based on the current information alone (Eidsvik, 2015). In other words, VOI represents the maximum price the decision maker is willing to pay for the information, reflecting their personal preferences (Eidsvik, 2015) . At this price, the decision maker does not prefer having the information over not having it, and vice versa. Consequently, any price below this threshold would be acceptable, making VOI the highest amount the decision maker should consider investing in acquiring the information (Eidsvik, 2015)

1.3.2 Value of Perfect Information (VOPI)

Now suppose the decision maker can know for certain the information is always correct. Assuming the decision maker is risk-neutral, the VOI is computed as the difference between expected value with additional information and expected value without information (Bratvold et al., 2009) or:

$$VOI = Expected\ Value\ with\ additonal\ information - Expected\ Value\ without\ additional\ information$$

1.3.3 Value of Imperfect information (VOII)

In real world situations, the information obtained is imperfect but still helps the decision maker to know how valuable the information gathering is. Assume that the decision maker can conduct a test to observe the uncertainty with an accuracy less than 100%. Now, the probability of each of the outcomes can be updated based on the test results using Bayes' theorem

$$p(y) = p(y|x)p(x)$$

Also, the posterior probabilities for each outcome (***x)*** given the different test result of (***y***) are calculated.

$$p(x|y) = \frac{p(y|x)p(x)}{p(y)}$$

1.4 GEOLOGIC SETTING

The Oligocene Frio Formation, a significant oil and gas reservoir in the South Texas Gulf Coast, has produced an estimated 70 trillion cubic feet of gas and 8 billion barrels of oil (Bonnaffé et al., 2008). Understanding the Oligocene Frio Formation, its sequence stratigraphy framework, structural setting, depositional environments, and reservoir quality is essential for efficient CO_2 storage site evaluation and management.

1.4.1 Regional understanding of the Frio Formation

The Frio deposode constitutes one of the important episodes in the depositional history of the Gulf of Mexico (Snedden & Galloway, 2019). An important sediment influx and margin accretion occurred during the Frio deposode (Figure 1). Structurally, contemporaneous growth faults developed parallel to the shelf margin and syndepositional movement resulted in sediment thickening on the downthrown side of the faults (Figure 2). The Oligocene Frio structure along the Texas Gulf Coast developed in response to third-order sea-level falls where coarser-grained sediments were shed from the exposed shelf and differentially loaded the slope, thus triggering down to the basin growth-faults (Brown et al., 2004).

Extensive Frio research has been done in the Corpus Christi area (South Texas), which is about 130 km away from our storage site(Bonnaffé et al., 2008; Brown et al., 2004; Hammes et al., 2006). For instance, Bonnaffé et al. (2008), divided the Frio Formation in Corpus Christi area into six third-order sequences, each comprising basin-

floor and slope-fan deposits, along with a prograding wedge deposited during third-order sea-level lowstands (Bonnaffé et al., 2008). Growth faulting was important in the area and significantly influenced sediment distribution and stratigraphy (i.e., Figure 3).

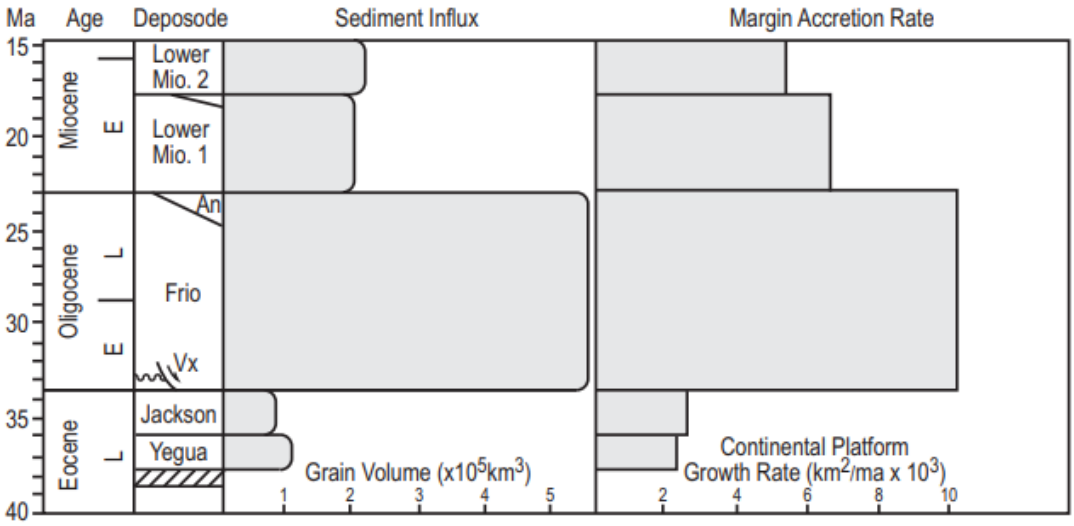

Figure 1: Northern Gulf (US) margin deposodes, sediment influx, calculated as total grain volume, and continental margin accretion rates

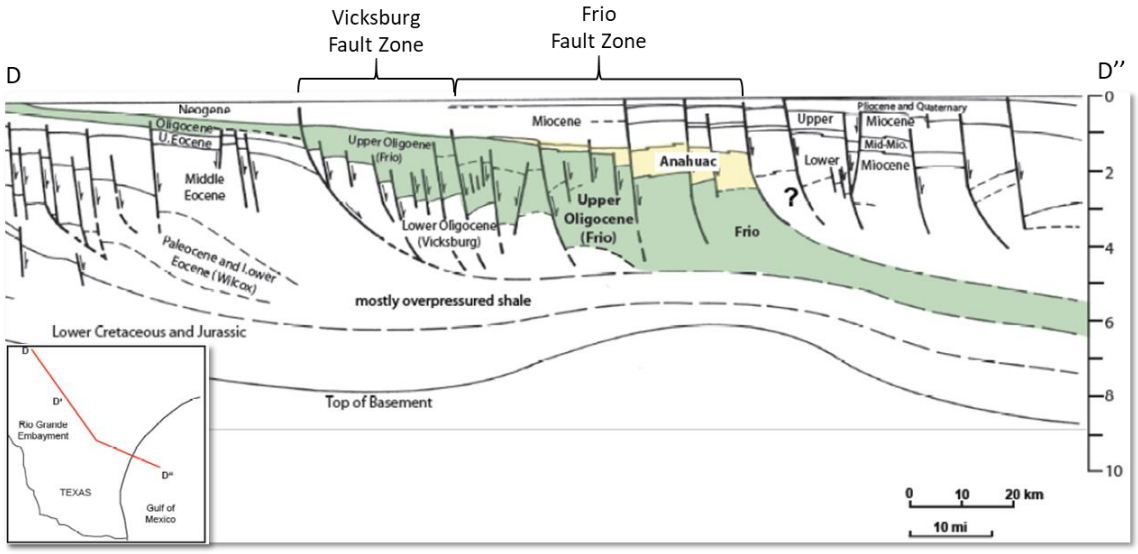

Figure 2: NW-SE cross section of Texas Gulf Coast basin, showing basin-margin faults (modified from Ewing, 1991)

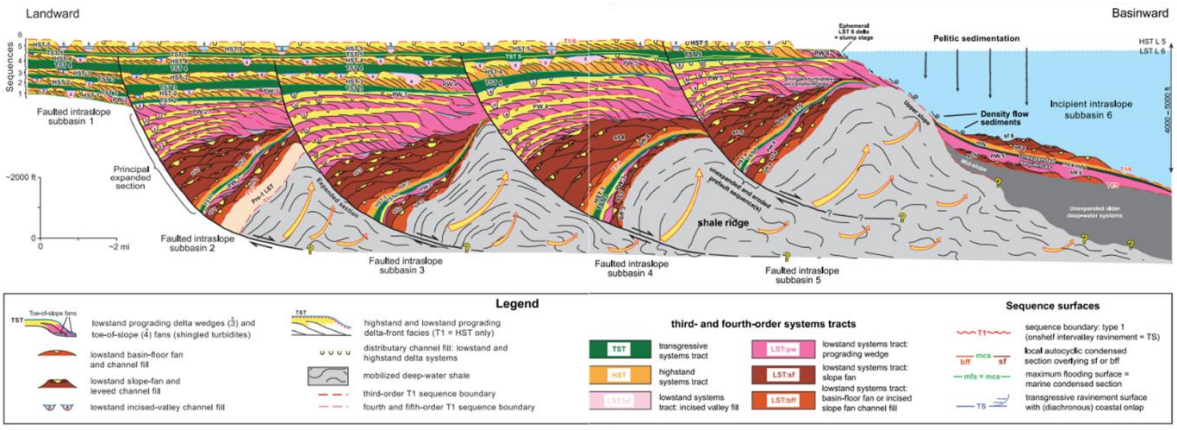

Figure 3: Diagrammatic dip cross section showing formation of successive growth-faulted subbasins (Corpus Christi, Texas). Each subbasin is filled with genetically similar but diachronous depositional systems (from Brown et al, 2004)

1.4.2 Depositional setting

During the Oligocene, massive sediment influx from sources in Mexico and the southwestern United States occurred as a result of uplift and erosion that started in Mexico and migrated along the western margin of the Gulf Coast basin (Galloway and others, 1982, 2000). Explosive volcanism and caldera formation in Mexico combined with regional uplift to create an influx of recycled sedimentary rocks, volcaniclastics, and reworked ash into the western and central Gulf of Mexico (Galloway, 1977).

Multiple large, bedload-rich rivers delivered sediment to the northwest and central Gulf, focusing into four major fluvial–deltaic axes (Figure 4). These include the Mississippi, Houston, Rio Grande, and Rio Bravo. Together, these rivers constructed a robust, highly progradational continental margin that buried the basal Oligocene Vicksburg fault zone and advanced the shelf edge 95–145 km (60–90 miles) basinward of its Eocene position. Rapid accumulation triggered a succession of arcuate growth faults (the Frio growth fault belt) that advanced basinward in tandem with shelf edge progradation, greatly expanding upper slope and shelf-margin delta facies(Snedden & Galloway, 2019). The Rio

Grande and Rio Bravo converged to supply a single composite depocenter. Downdip, the deltas of the Rio Bravo and Rio Grande fluvial systems merged to form the composite, sand-rich, wave-dominated Reynosa–Norias system, which bridges the Burgos basin in Tamaulipas and Rio Grande Embayment of south Texas (Figure 5). Our storage site sits within the Rio Grande embayment.

More details on the stratigraphy and depositional setting of the storage site are provided in Chapter 2 of this thesis.

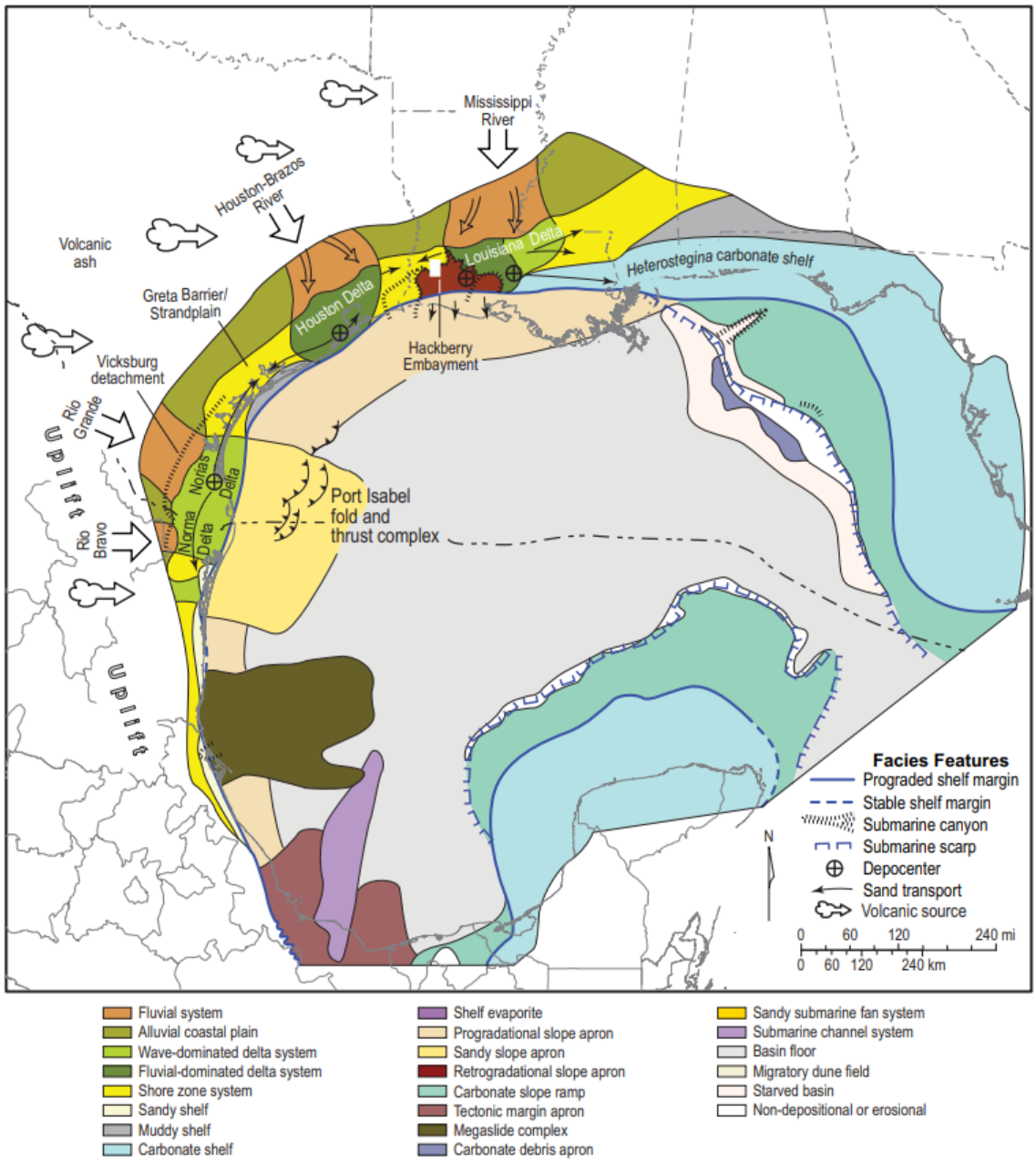

Figure 4: Paleogeographic map of the Oligocene Frio deposode. Depositional system outlines and shelf edge reflect their positions at maximum progradation. Arrows point to the four major fluvial–deltaic axes: Mississippi, Houston, Rio Grande, and Rio Bravo. (GBDS, 2019)

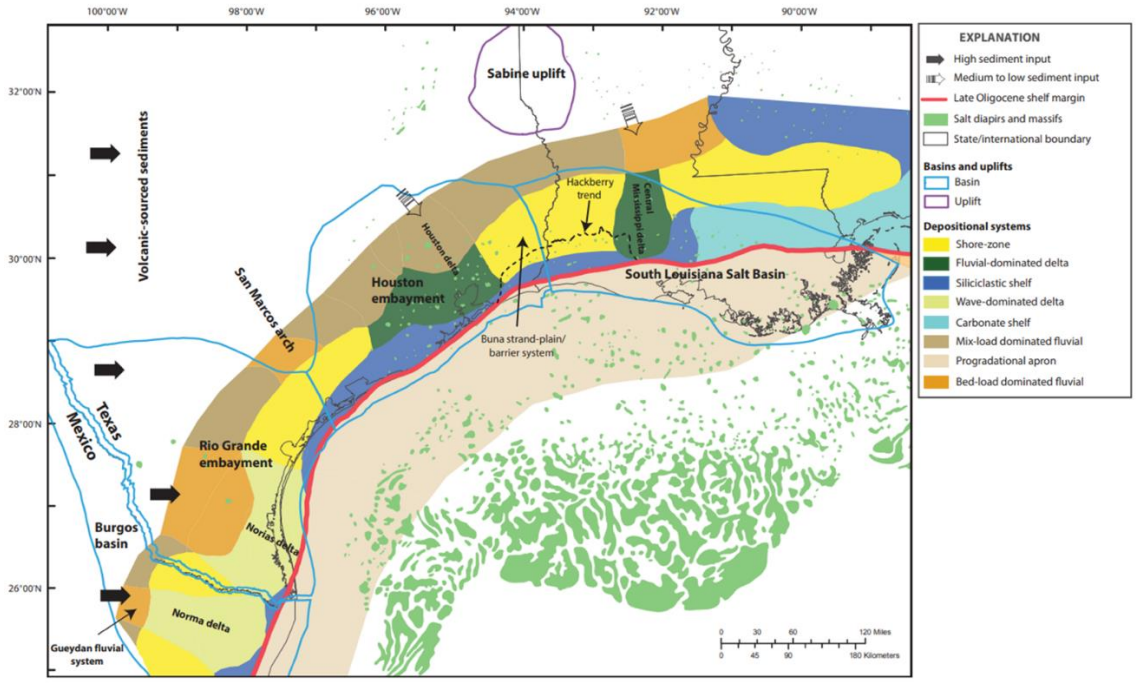

Figure 5: Main sediment sources, basins and uplift, and depositional systems in the northern Gulf of Mexico during the late Oligocene (modified from Galloway and others, 2000). The Rio Grande embayment includes the area of interest.

1.4.3 Reservoir Quality

The reservoir quality of the Frio Formation in the Texas Gulf Coast varies significantly due to several regional factors, including mineral composition, geothermal gradient, and diagenetic processes. These factors contribute to the variability in porosity and permeability, which are crucial for determining the reservoir's ability to store CO_2.

Frio sandstones are mineralogically diverse (Galloway 1977; Loucks et al. 1984). A strong west-to-east decrease in abundance of volcanic grains and plagioclase feldspar (and commensurate increase in quartz) parallels the increasing distance between river drainage axes and the Oligocene volcanic uplands.

Frio sandstones are poorly sorted, fine-grained, feldspathic litharenites to lithic arkoses along the lower Texas Gulf Coast (South Texas) to poorly sorted, fine-grained,

quartzose lithic arkoses to subarkoses along the upper Texas Gulf Coast. Volcanic and carbonate rock fragments are common in the lower Texas Gulf Coast and decrease in abundance up the coast (Loucks et al. 1984). Volcanic and carbonate rock fragments are common in the lower Texas Gulf Coast and decrease in abundance up the coast. Frio sandstones show a systematic improvement in reservoir quality from the lower to the upper Texas Gulf Coast that is related to grain composition and geothermal gradient (Figure 6) (Loucks et al. 1984).

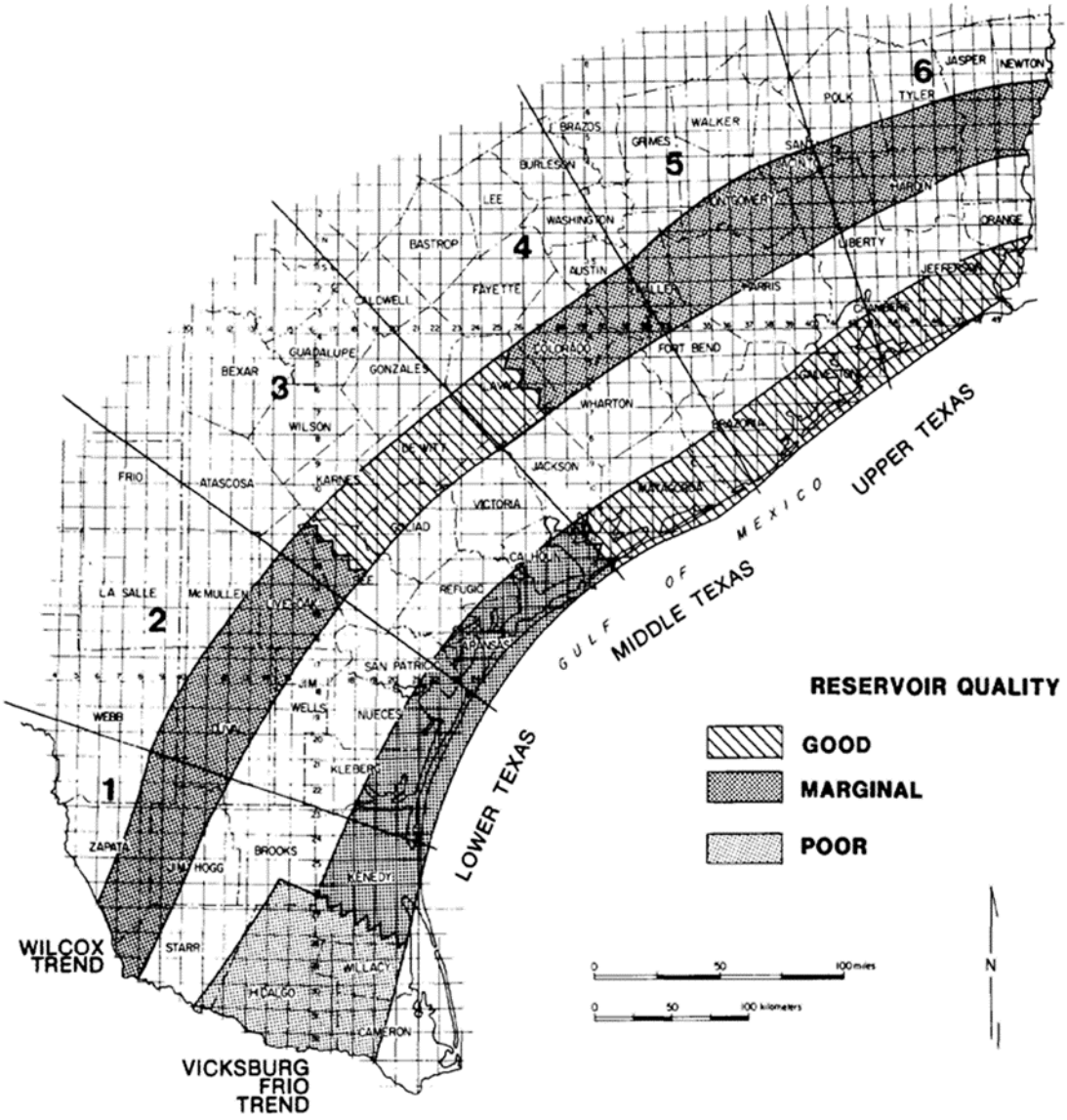

Figure 6: Map displaying potential for high-quality, deep reservoirs (>3350 m, 11,000 ft) in Lower Tertiary strata along the Texas Gulf Coast. Good indicates permeability values commonly greater than 20 mD. Marginal indicates permeability values generally less than a md (from Loucks et al. 1984)

1.5 Study Area and Dataset

We chose this area in a field in South Texas to study the potential of a GCS site. The dataset consists of existing 14 wells with logs such as gamma ray, spontaneous

potential, density and sonic, (Table 1). These wells are located in the periphery of the area of interest. In addition, the dataset consists of 3D seismic cube where seismic horizons and faults were interpreted. The details will be explained in the next chapters. Most of these wells are wildcats and plugged and abandoned (P&A). These wells are more than 3000 and up to 50,000 ft apart from each other in the N-S direction.

Table 1: Dataset of the study area

Conceptual	**Input Data**
Area of Interest	3D Seismic cube
Structure position	Legacy wells
Geometry	Well Tops
Lithology	Seismic horizons
	Faults
	Well logs (GR, SP, DT, RHOB, RD..)

1.6 RESEARCH RELEVANCE

Geological carbon storage (GCS) projects in the United States are regulated by the Environmental Protection Agency (EPA) under the Safe Drinking Water Act, which sets standards to protect Underground Sources of Drinking Water (USDW). The EPA's "Geologic Sequestration of Carbon Dioxide: Underground Injection Control (UIC) Program Class VI Well Site Characterization Guidance" (2013) emphasizes the importance of comprehensive site characterization for Class VI wells, typically involving drilling stratigraphic wells within the project area. However, the decision to drill such wells is site-specific and left to the discretion of the permit applicant. Consequently, uncertainties persist regarding the value of investing in stratigraphic wells or other data acquisition methods to mitigate storage capacity risks.

Significant research has been conducted on carbon capture and storage (CCS) operations, including models that inform decision-making for GCS projects (Hosseini et al., 2024). While previous studies on the VOI primarily focus on monitoring technologies, there is a gap in understanding the value of stratigraphic well data in addressing geological uncertainties such as reservoir quality and sand continuity. This research aims to fill that gap by applying VOI analysis to stratigraphic well data during the pre-injection stage of a GCS project.

Our study examines a potential GCS site in South Texas, USA, characterized by limited data and low reservoir quality. Available information comes from legacy wells located on the periphery of the area of interest (AoI). The primary challenges include faulting, low reservoir quality, and the absence of wells at the preferred site location. The most significant geological risk is reservoir quality, which affects injectivity and, consequently, total storage capacity.

Determining whether to drill stratigraphic wells based on current information is a critical decision, especially considering the site's low reservoir quality that may limit CO_2 storage volumes. Although this site may primarily interest a Direct Air Capture (DAC) project due to lower volume requirements. However, even a DAC operator needs assurance that the formation can store the captured volume within a given timeframe.

1.7 Research Goals

The goal of this study is to develop a strategic framework for CO_2 sequestration that assists operators in making informed, cost-effective decisions during pre-injection planning. By utilizing the VOI framework, we aim to quantify the financial value of reducing storage capacity uncertainty through additional data acquisition, specifically by drilling stratigraphic wells.

We will apply the VOI methodology to determine the "buying price" (Bratvold et al., 2009) for drilling stratigraphic wells—the maximum amount a DAC operator should be willing to invest. Any cost exceeding this value would not justify the investment, as it would not provide sufficient value relative to the incurred expenses.

This research involves evaluating CO_2 plume migration and pressure build-up in a complex structural setting with high depositional facies variability. By simulating injection in an area with low structural gradient and complex depositional facies, we can assess the impact of geological uncertainties on storage capacity.

By extending VOI analysis to include stratigraphic well data and focusing on geological uncertainties, this study contributes to improved decision-making in GCS projects, particularly during the pre-injection stage.

1.8 PROJECT WORKFLOW

The research is structure as follows: it begins with an overview of the potential storage site and an assessment of available datasets (Chapter 2: Reservoir Characterization). Geological and geophysical data from a site in South Texas, including raw data and previous interpretations, were cleaned and quality-checked before static model building.

In Chapter 3: 3D Geocellular Modeling for the Upper Frio Zone, using well logs, seismic horizons, and faults within the zone of interest was conducted. Structural interpretation in time was followed by time-depth conversion. Facies analysis identified sand trends based on well logs and seismic facies. A 3D geological model (static model) was built to generate porosity and permeability models, with petrophysical analysis determining key reservoir parameters.

The static model served as the foundation for simulation studies in Chapter 4: CO_2 Storage Capacity Analysis. CO_2 plume simulations modeled plume behavior and pressure front extent to delineate the Area of Review (AoR), assessing storage capacity and the reservoir's dynamic response to CO_2 injection.

In Chapter 5: Value of Information, economic modeling and VOI analysis evaluated the benefits of drilling stratigraphic wells to reduce pre-injection uncertainties. This analysis determined the maximum justified investment in additional data acquisition methods to mitigate geological risks.

The study concludes with a discussion of findings and future work in Chapter 6, followed by conclusions and recommendations in Chapter 7.

Chapter 2: Reservoir Characterization of the Storage Site

2.1 INTRODUCTION

The storage site is located in South Texas, USA, within the paleo Rio Grande embayment. Due to a confidentiality agreement with the landowner, the exact location of the site cannot be released. However, the evaluation with real data is provided in this thesis report. The storage site sits within a total area of 10 miles (52,435 ft) by 9 miles (42,700 ft) as shown in Figure 7. The subsurface characterization was performed on the Frio formation, which poses a challenging reservoir quality due to its volcanic content's nature.

The initial plan was to characterize the full-storage window (about 3000 to 4200 ft) including running amplitude analysis in Paleoscan on several seismic horizons in the model. However, this analysis is still not conclusive due to the amount of noise in the seismic. The full storage section (Figure 8) was originally considered to provide an overview of the total storage capacity of the site. Due to time constraints, only one zone was targeted for detailed evaluation, that is the interval between Frio Top and Frio FS1 marker (called Upper Frio zone) (see Figure 8). This research focuses on the Upper Frio zone, so a feasibility study for a GCS site would have some limitations since it does not consider the total section for storage. The project may not be economic for the Upper Frio zone itself, but it could be economic if we consider the full stratigraphy available for CO_2 storage. This will be discussed in the VOI section of the thesis.

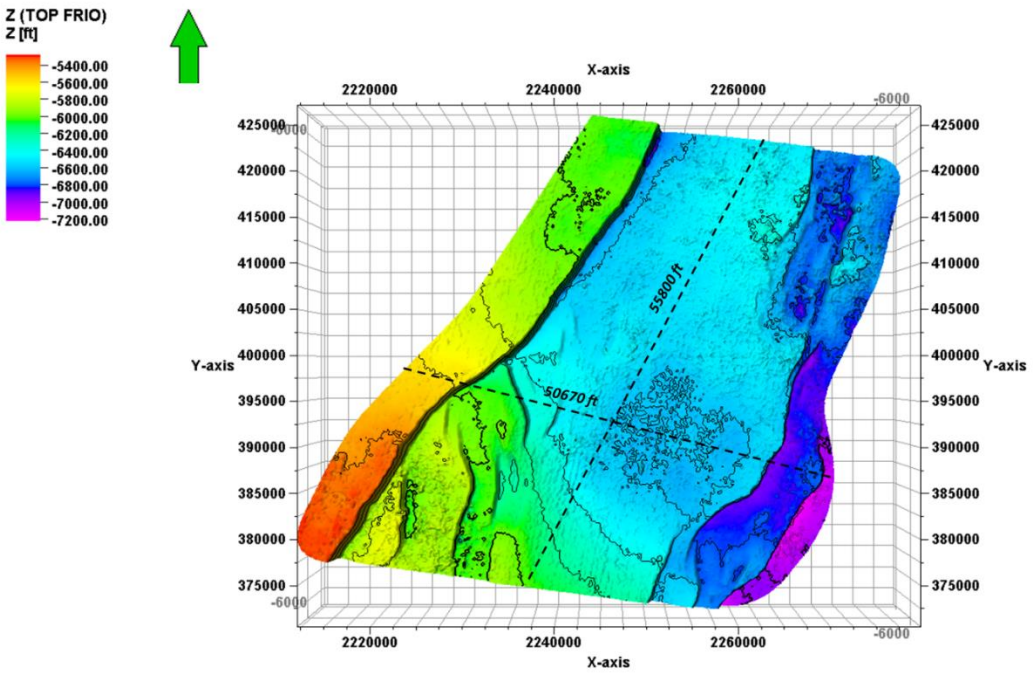

Figure 7: Size of the area in USft (~56,000 ft by 50,670 ft) about an area of 232 km^2

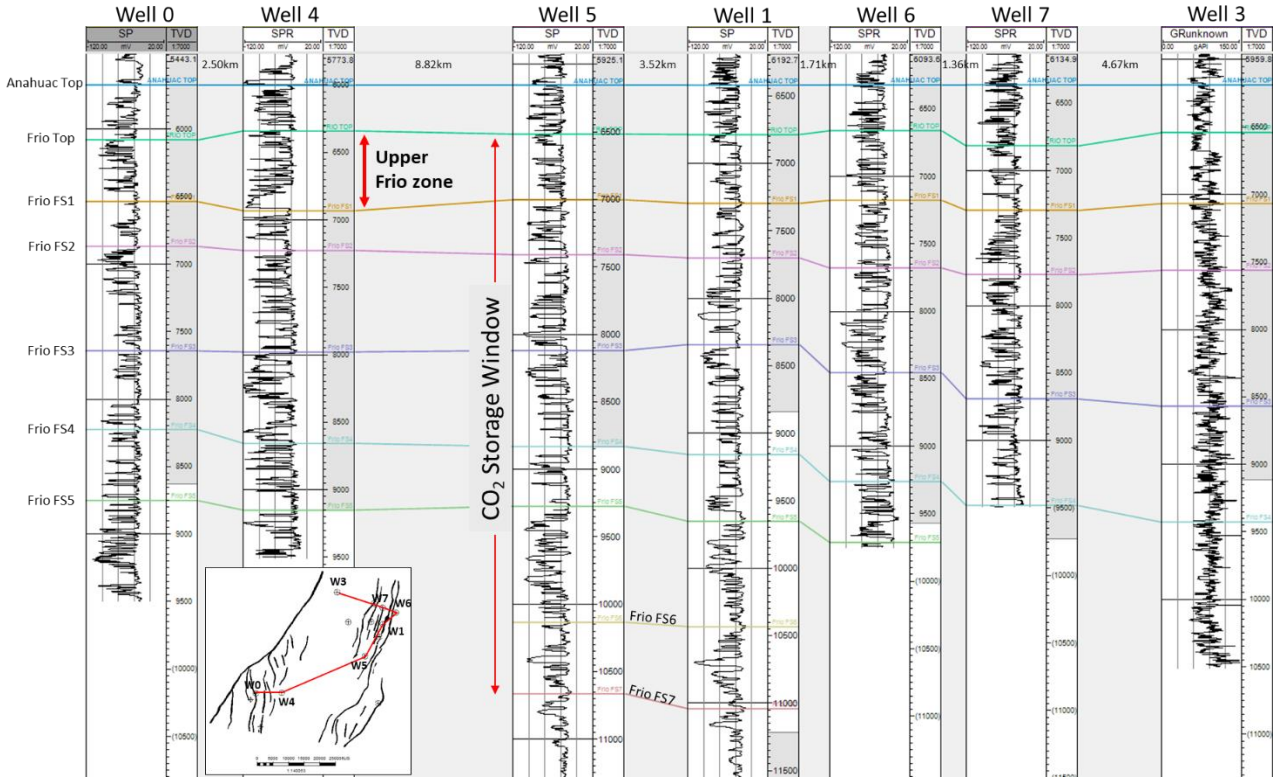

Figure 8: Well-log correlation in the AOI, showing the total storage section (Frio Top-Frio FS7 marker) and the targeted section (Frio Top-Frio FS1 marker). The correlation line shown on the map

2.1.1 Data cleaning and readiness

We received actual data for the research study. A lot of data cleaning was needed to pursue the research workflow. A project in Petrel was received with field data (logs, seismic interpretations, and a structure model- all in time domain). I managed along with my supervisors and a geophysicist from the land owner to narrow and tailor the project area to our needs. In the case of the well log data, the spontaneous potential (SP) and Gamma Ray (GR) logs were quality checked by plotting all GR logs and SP from the interest zone (Upper Frio) in a histogram window (Figure 9). Since all wells with the specific GR or SP are laying on top of each other, then these logs are fairly consistent and

good to go for stratigraphy and petrophysics analysis. Only one well was set for normalization, adding a calibration of 40 mV.

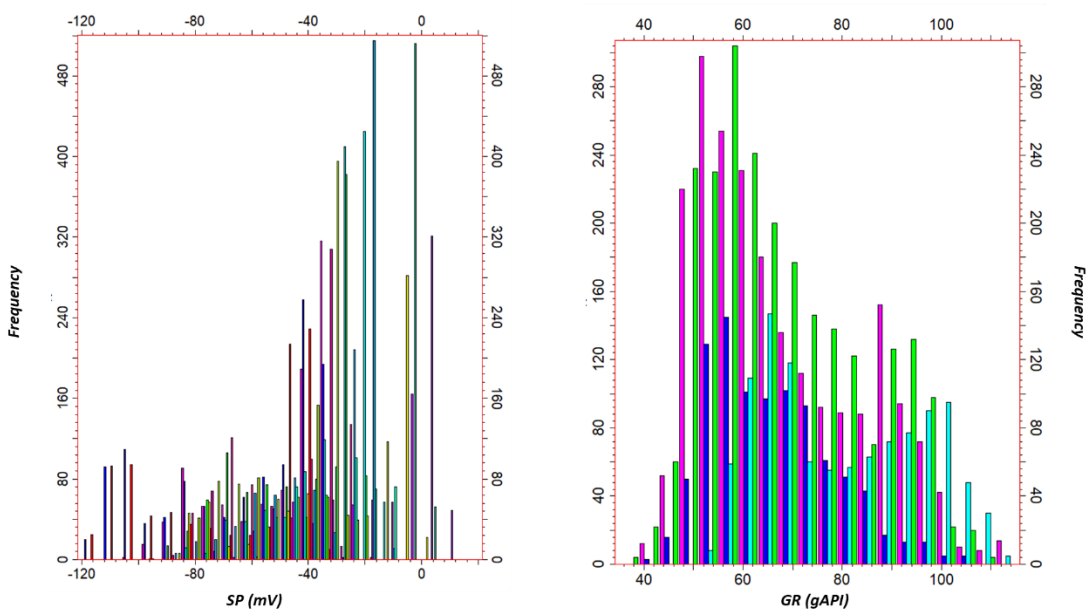

Figure 9: The SP and GR logs of the wells show normalization within the zone of interest (Upper Frio Zone). The SP logs are denser due to the higher number of wells with SP than the GR log. We ignore the outliers in the SP log, limiting the scale between 0 to -1

Basic well-log analysis is crucial to build a robust model. Later in this chapter, a framework of which petrophysical well-log curves were calculated to feed into the model would be discussed. There are 14 wells with limited well log data; twelve out of them have SP log, four with GR; three with sonic (DT), and two wells with bulk density log (RHOB) (see Table 2). The SP is scaled from 0 to -100 mV, and GR from 0 to 150 API, following the standard practice. There are three key wells with SP, GR, RHOB, and DT logs.

Table 2: Available well logs

Well log	Total Number	Log name
SP_SM	12	Spontaneous potential
RD_SM	12	Deep Resisitivity
RS_SM	12	Shallow resistivity
GR_SM	4	Gamma Ray
DT_SM	3	Sonic
CALI_SM	3	Caliper
RHOB_SM	2	Bulk Density
RM_SM	1	Medium Resisitivity
NPHI_SM	1	Neutron Porosity
DRHO_SM	1	Density

For standardization purposes, wells were grouped with my own naming convention, which is the reason for a "_SM" suffix attached to each log (see Table 2). Despite the availability of multiple log curves, the ones used in the petrophysical analysis were the SP, GR, sonic and bulk density.

2.2 STRUCTURAL FRAMEWORK

2.2.1 3D Seismic Interpretation: Horizon mapping

The targeted seismic horizons are Top Frio and Frio FS1, which are the top and base of the Upper Frio zone. The average thickness of the zone is 500 ft. In the initial stage of the study, the base of the storage section (Frio FS7 marker) was reinterpreted from a seismic horizon provided by the data owner. The base of the Frio storage section (Frio FS7), in the area of interest, is about 2900 to 4200 ft from the Frio Top as shown in Figure 10. The Frio formation in the area of interest is thick but we chose to limit the interval of interest to the Upper Frio zone, for the purpose of this thesis project, since it would require more structural interpretation and modeling that is beyond the timeline and scope of this research. Figure 10 shows a seismic line and a well with a check-shot that was used for calibration of seismic horizons vs. well picks. Figure 11 shows the seismic surfaces of

interest for this research, on a Inline and Xline intersection with the depth grids intersecting wells A and B. The depth grids were used as inputs for 3D modeling.

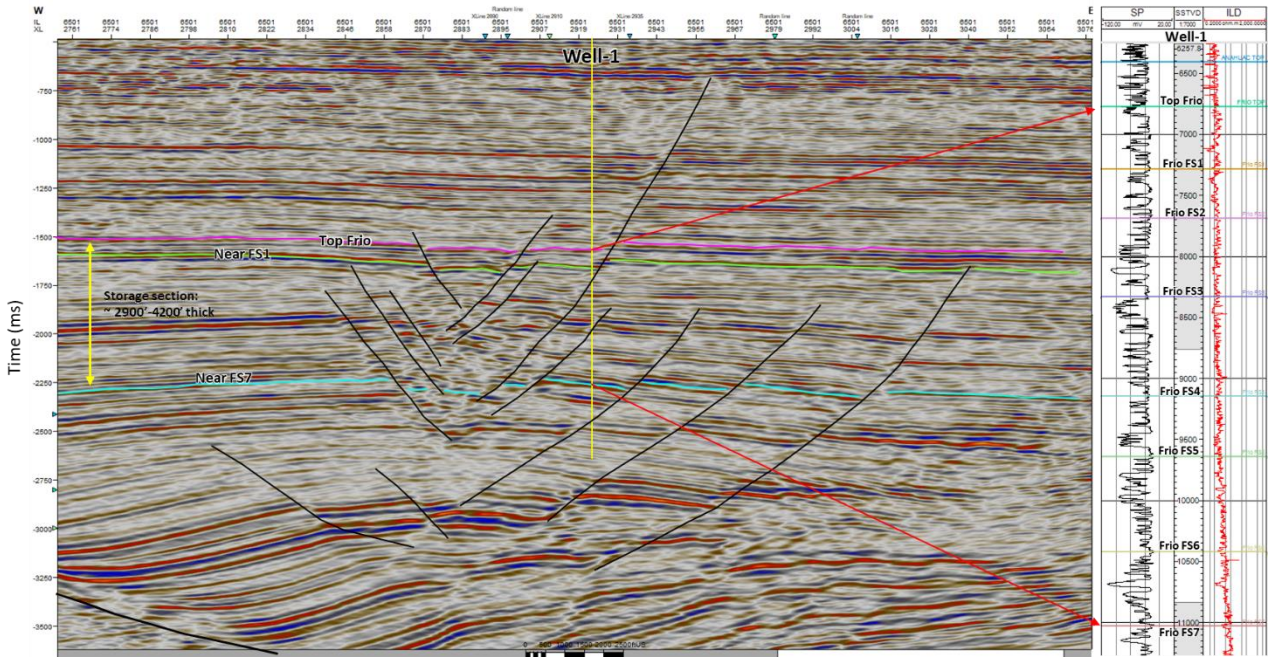

Figure 10: Seismic interpretation of Top Frio to base of Frio storage section (i.e., FS7)

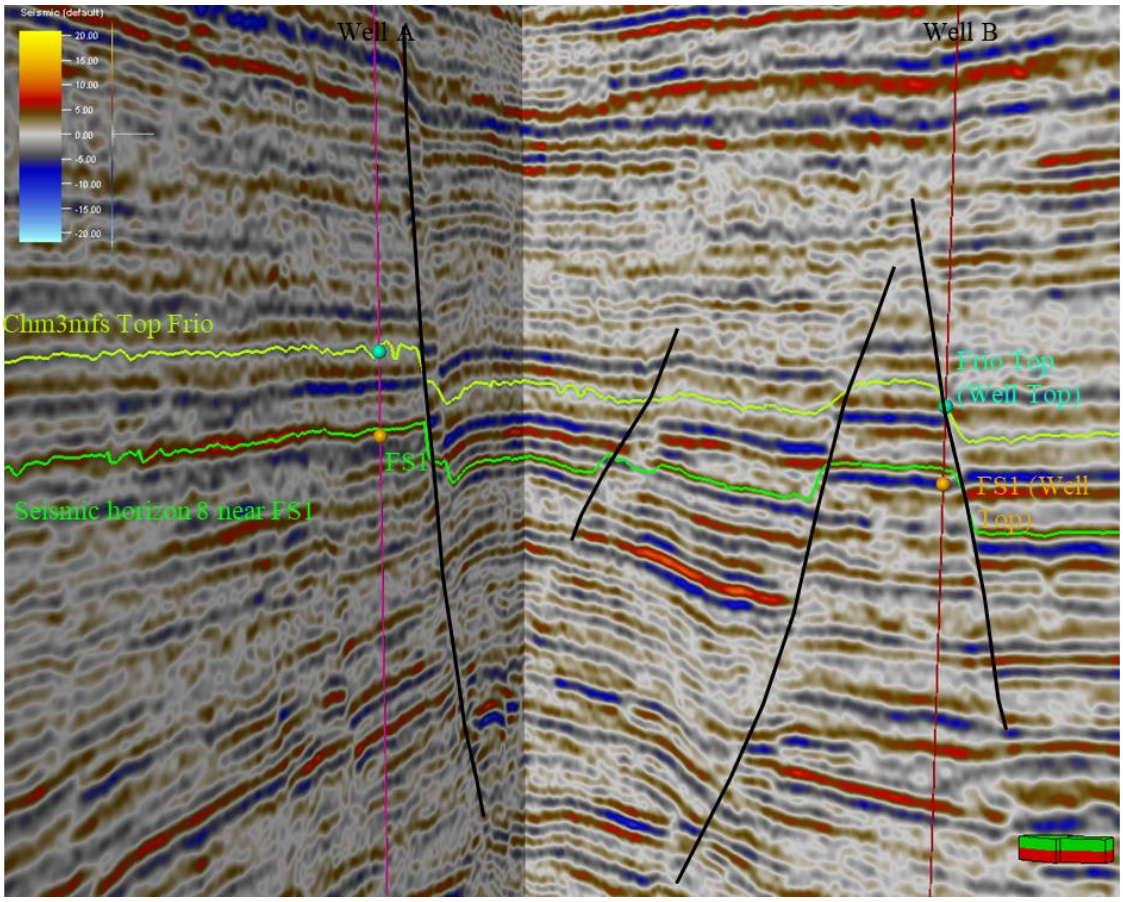

Figure 11: QC visualization - The displayed surfaces on the Inline and Xline seismic are the depth grids intersecting the well tops at wells A and B.

2.2.2 Main Faults and Faults that intercept the Upper Frio zone

There is a total of 37 faults cutting both horizons, the Top Frio and Frio FS1. A number of faults were received from the data owner and others were interpreted at GCCC, as part of the data readiness and quality check process. These faults were picked on the 3D seismic volume (Figure 12). After cleaning and adjusting the faults, the new total number came down to 35 (Figure 13). The 3D fault modeling was an important process as the faults are all included in the AOI for geomodelling with Petrel software. It is crucial to account for the major and minor faults, especially when modeling the extent of the CO_2 plume and

pressure build up, and the leakage potential of these faults in the AOI. The faults could either act as sealing features or leakage pathways. In this research we ignore the conditions of these fault pathways and we considered the faults in the model as volume modifier (refer to Chapter 4 for the details of CO_2 plume modeling and pressure build up).

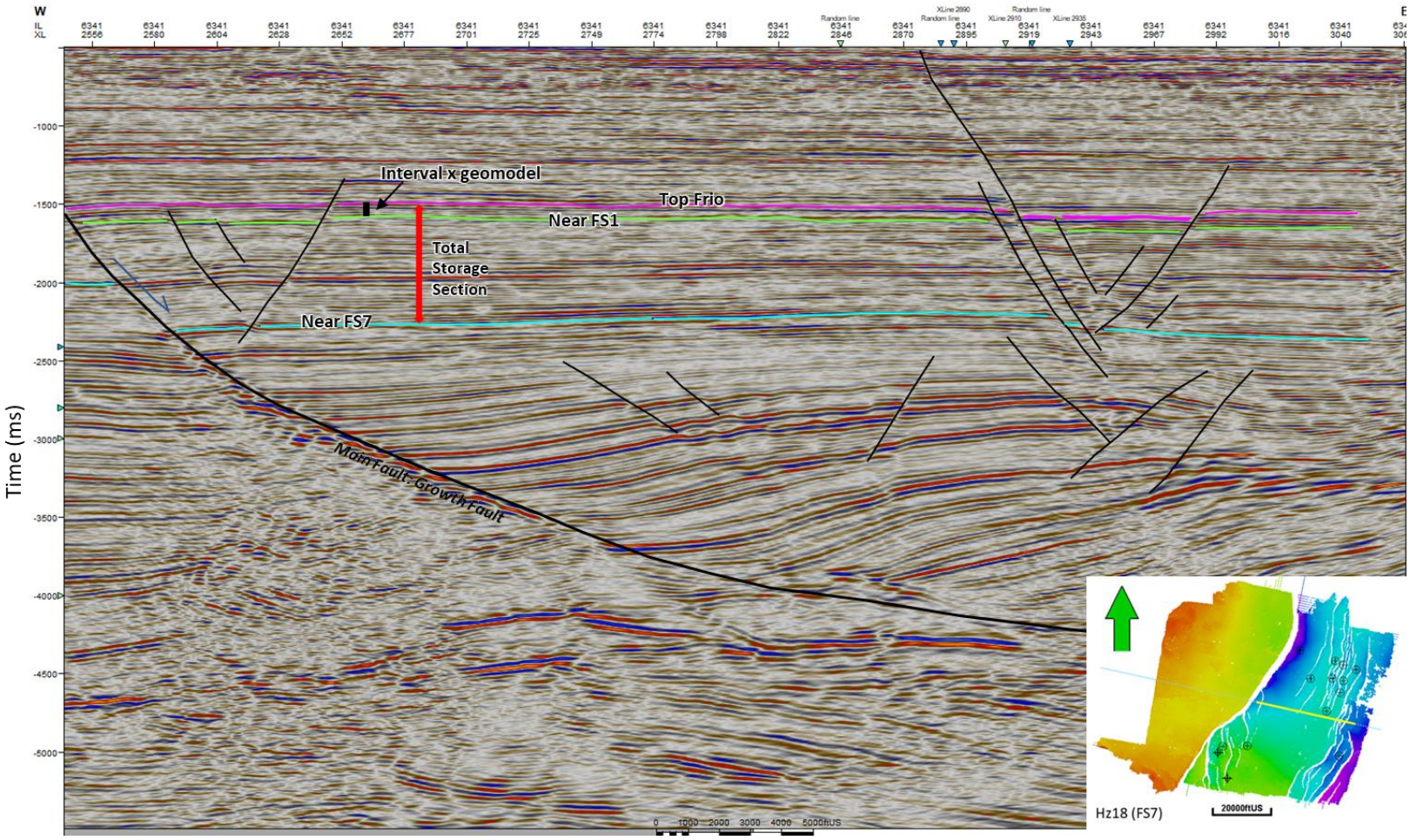

Figure 12: Seismic Inline with some of the faults in AOI. The target zone between pink and green horizons (Top Frio – FS1), the red arrow indicates the total storage section.

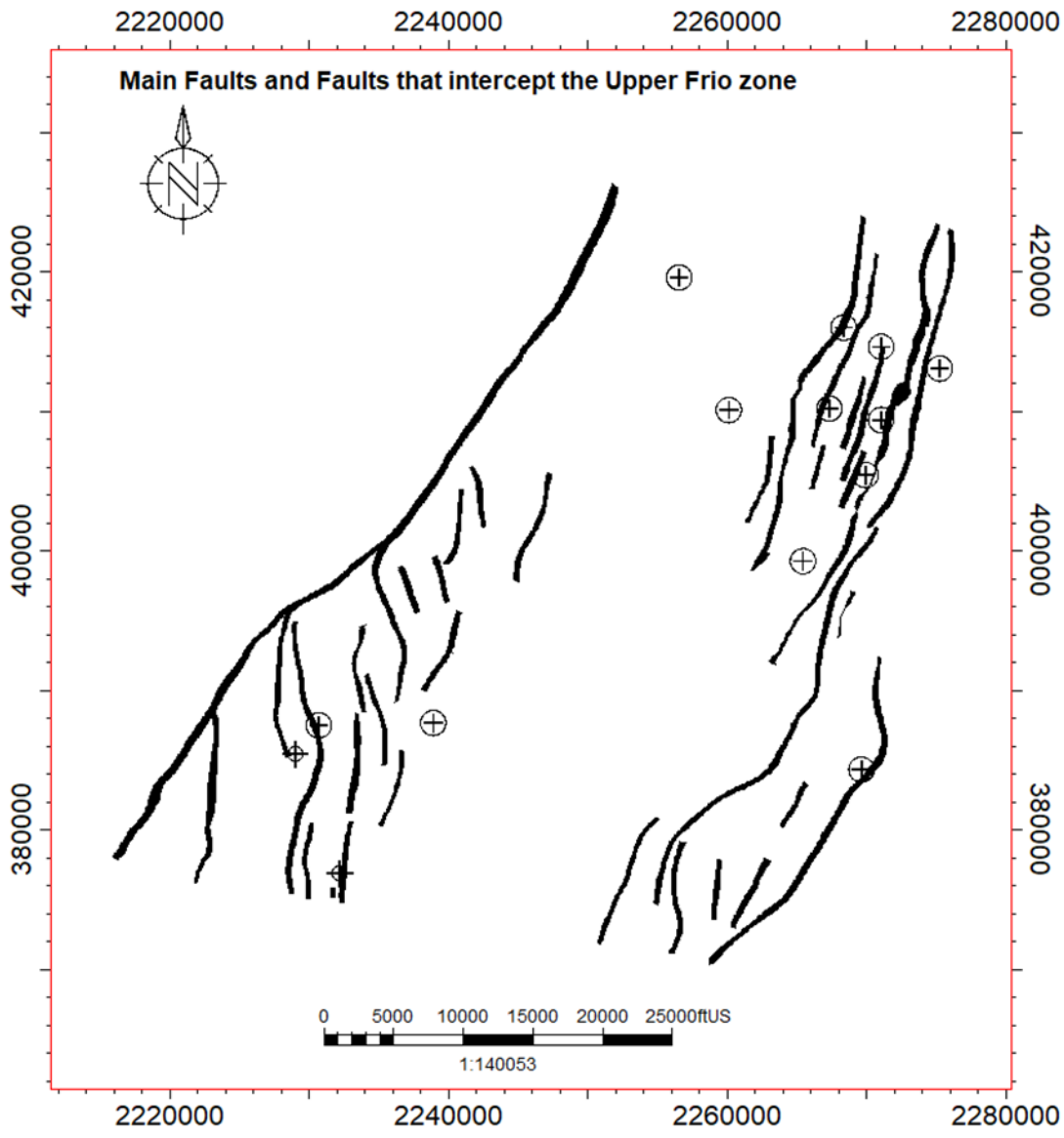

Figure 13: Map view of the faults with the wells' location

2.2.3 Time-Depth Conversion

The inherited original project was in the time domain. For a standard 3D geomodelling workflow, the domain must be in depth.

There are multiple velocity methods and models in Petrel for the *Advanced Velocity Models*. For this project, the velocity method used for defining the velocity input is dependent upon the velocity model that has been used. The surfaces (Top Frio and FS1) cover the whole area of the velocity zone. The value is estimated using the time-depth relationship (TDR) through the zone for each well and interpolated to give a surface describing the variation of the value across the model (see Appendix A). Then the data in the correction column, which are the Top Frio and Frio FS1 depth surfaces, are used to define the value. Figure 14 is displaying one of the surfaces, i.e. Top Frio depth surface (the well picks are tied to the surface). Petrel finds the value at the location of each of the correction points so that the resulting conversion will match the correction point. The values are interpolated to give a surface describing the variation of the value across the model. Now, the zone in the velocity model must have a definition of the velocities within that zone. The velocity model used is V=Vo=Vint, the value of Vo is a surface defining the value at each XY location.

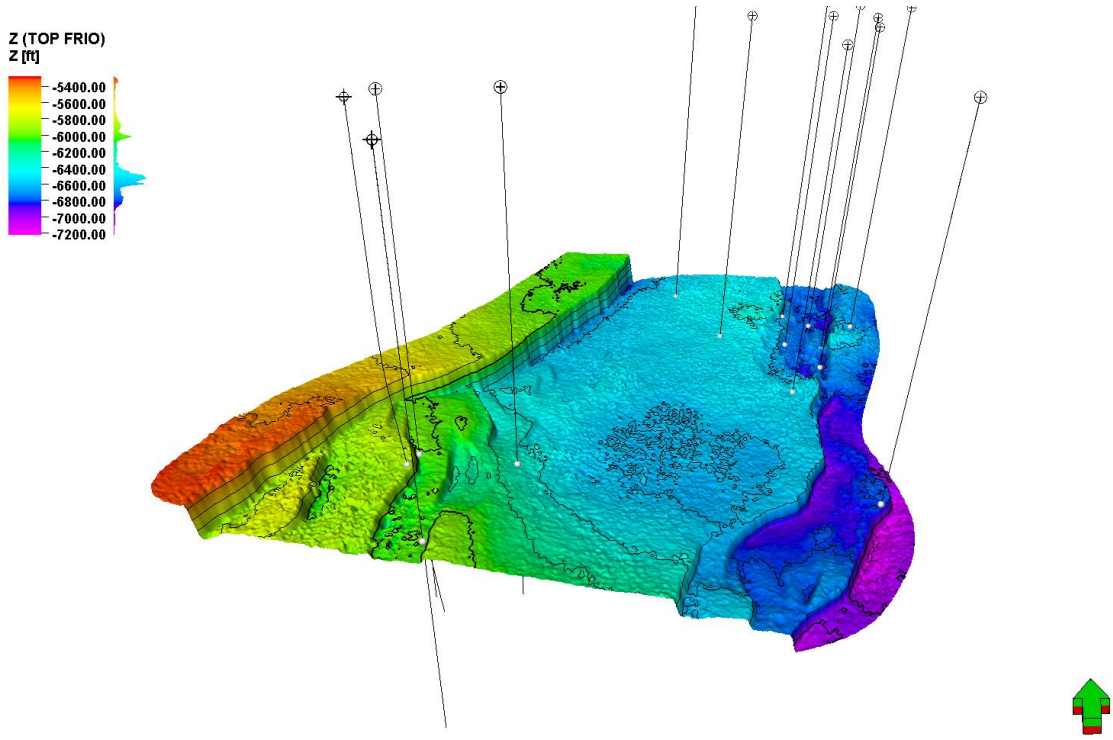

Figure 14: Frio Top structure map tied with its correspondent well pick as the input data in the correction column to define the value in the velocity model

Both resulted depth surfaces (Top Frio and FS1) are very similar and consistent to the time surfaces (Figure 15), so the velocity model created is acceptable for converting more time surfaces to depth. Any input in the time domain can be depth converted in the software.

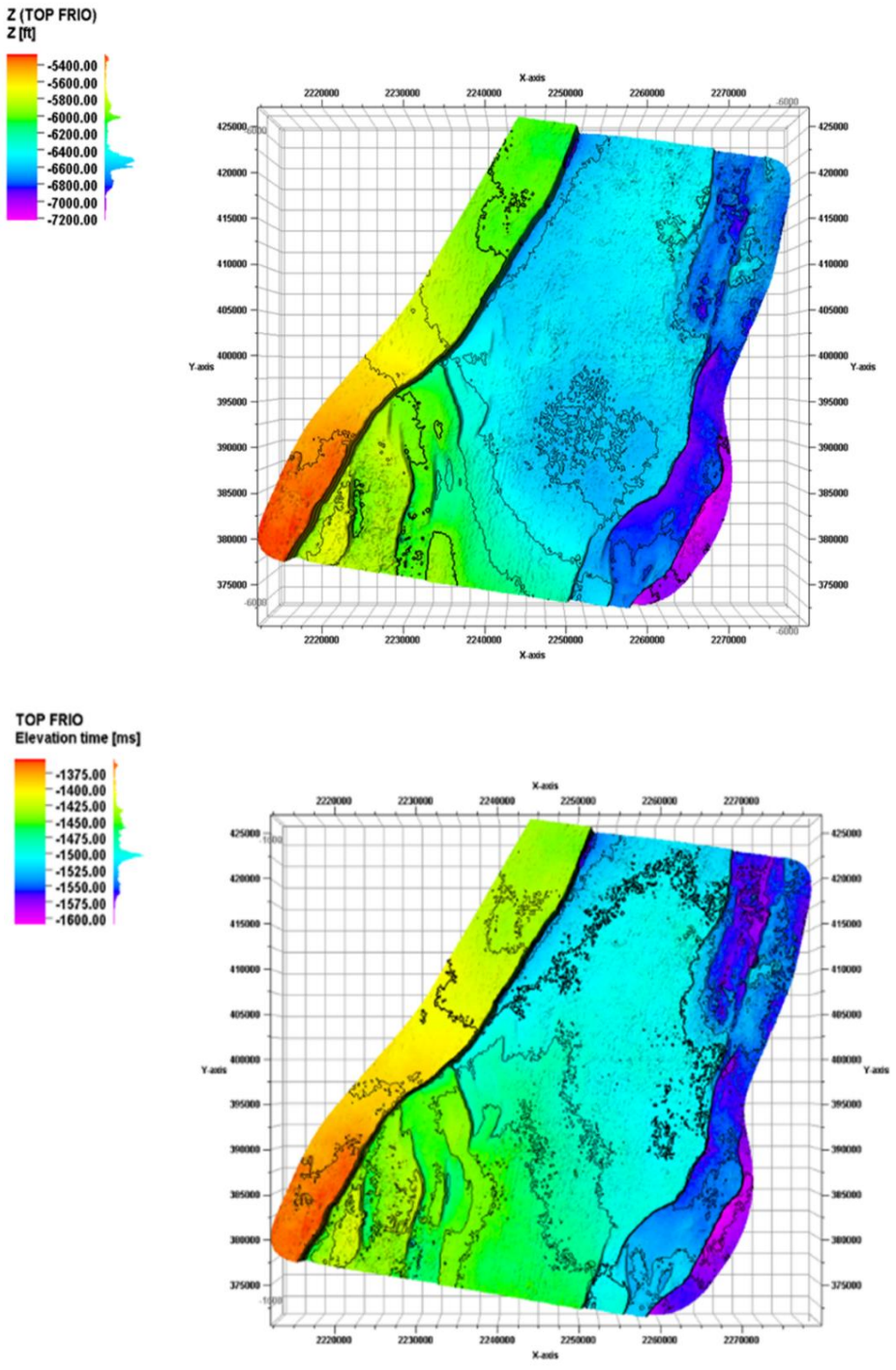

Figure 15: Map in time vs depth of the Top Frio, showing consistency following time-depth conversion process

2.3 STRATIGRAPHIC AND DEPOSITIONAL FRAMEWORK

2.3.1 Well Log Correlation

A key well was used to pick the Top Frio horizon on 3D seismic due to the availability of the Paleo data. We did not receive a synthetic seismogram for an appropriate seismic-well tie. The seismic horizons were previously interpreted from migrated 2D and 3D seismic surveys along with check shots in the area. The target injection interval is the Upper Frio zone, the stratigraphic uppermost interval of the Frio storage section (Figure 16). The reservoir units were picked based on well log correlation. The total 2900 to 4200 ft Frio storage section is defined from the Frio Top to the Frio FS7 marker (Figure 17). But we limited the detailed evaluation to the 500ft from Frio Top to Frio FS1.

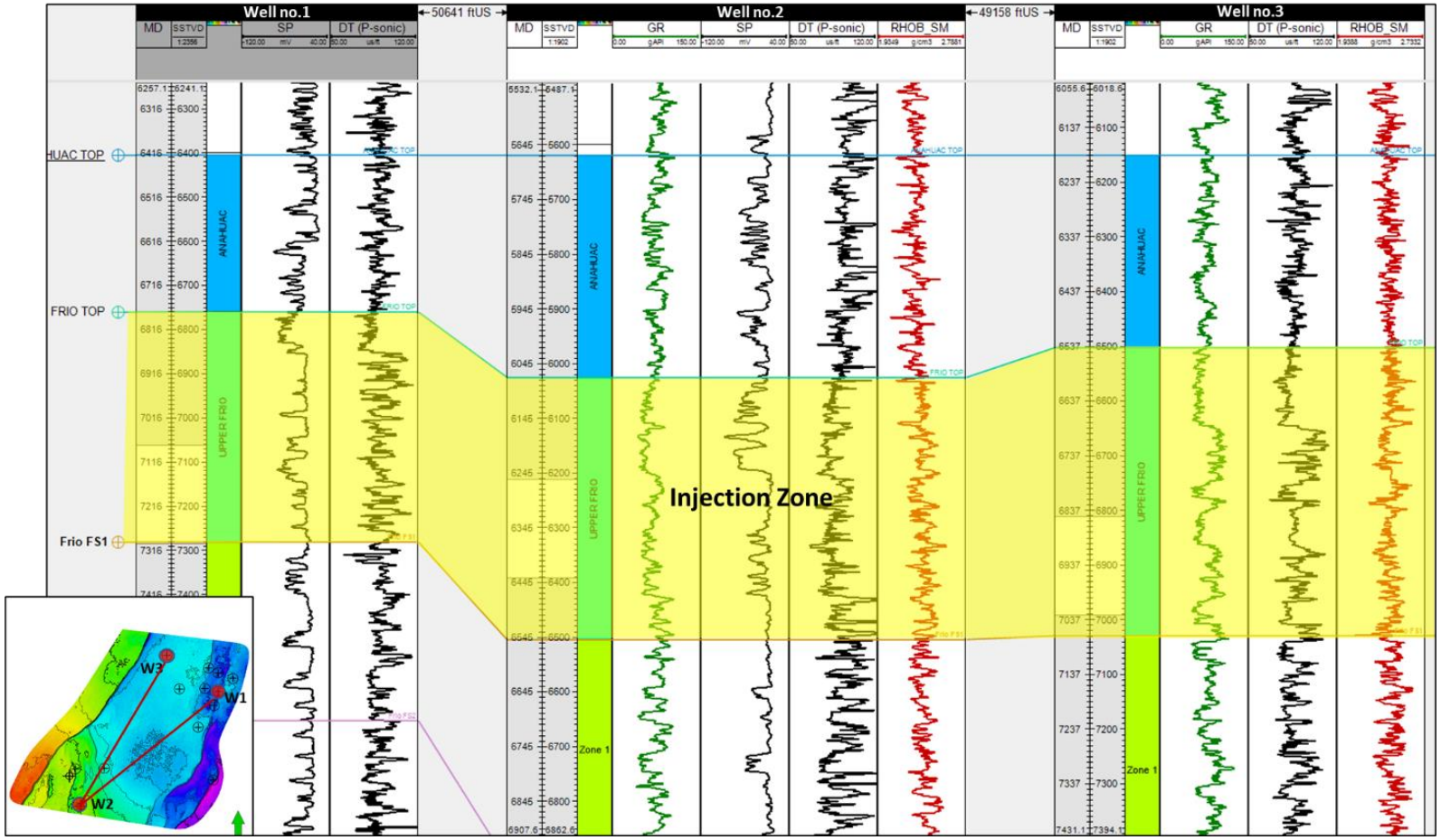

Figure 16: Well cross-section showing the main three key wells - the highlighted zone is the Upper Frio Zone, the target injection interval. The datum is the Anahuac shale.

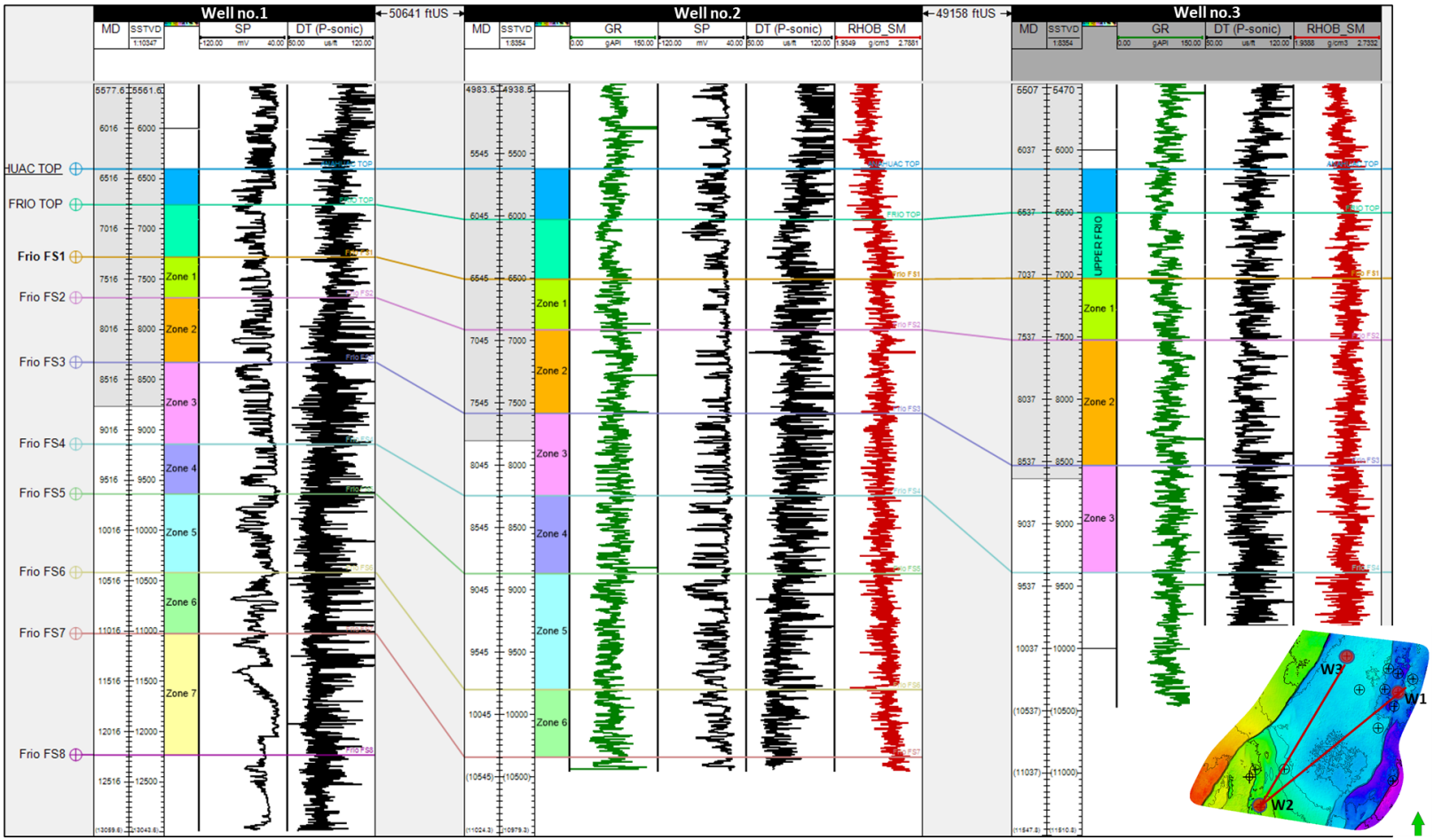

Figure 17: Stratigraphic cross-section of the Frio formation in the AOI, showing the multiple reservoir units. We are only focusing on the Upper Frio interval as the target injection interval for this study. Wells in cross-section contain the most complete suite of log curves

2.4 RESERVOIR QUALITY ANALYSIS

For the petrophysical analysis of this section, a workflow involving three main cases with a total of 21 realizations, was performed. Each case examines how porosity and variogram ranges affect storage estimates to account for the VOI analysis. Variogram estimates due to the scarcity of the data in the area, particularly the nugget and sill, determine spatial correlation and model variance The vertical variogram was based on the well log trend, and the horizonal (lateral spatial correlation) variogram ranges were estimated theoretically based on the current knowledge of the formation and nearby filed. The process is a blind testing method to have a base case by removing two wells out of the three key wells. Then building a second-generation model by adding the second well out of the 3 key reference wells; then building a third-generation model by adding the third well from the group of key wells. The objective is to evaluate and study the uncertainty ranges by evaluating and documenting any changes in the storage capacity estimations when running the dynamic simulations in chapter 4. The analysis is as follows:

Definitions:

1. **Key wells**

   There are only three wells out of the fourteen available legacy wells with computed porosity log from sonic or density curves

2. **Base case**

   Model with 12 existing wells only.

3. **Bplus (B+)**

   Adding one well to the base case model totaling 13 wells with a new porosity relationship

4. **Bplus plus (B++)**

Adding one more well to the B+ model totaling 14 wells with a new porosity relationship

2.4.1 Petrophysical Interpretation

In petrophysics, volume of clay (Vclay) is the fraction of a rock volume occupied by clay minerals. It is an important parameter used to determine the amount of clay present in the formation, which directly impact porosity, permeability, and fluid saturation (Moore et al., 2011). Knowing that not all wells have the measured log density (RHOB) and sonic (DT) logs to compute porosity from, and due to lack of core data, I used the measured logs GR and SP to calculate the Vclay (1)&(2) at each well suggesting well-log curves (Vclay and PHIE) (Satti et al., 2024). I set the Vclay based on the low (minimum) and high (maximum) readings of the logs at each well to set a cutoff for reservoir and non-reservoir.

$$Vclay = \frac{SP_{clean} - SP_{log}}{SP_{clean} - SP_{shale}} \quad (1)$$

Where; $Vclay$ is the volume of clay, SP_{clean} is the SP reading in a clean sand (maximum deflection), SP_{log} is the SP reading at the depth of interest, and SP_{shale} is the SP reading in a pure shale (SP log baseline)

Estimating Vclay using the SP log has several limitations; the SP log is less sensitive to clay content than the gamma ray log, potentially leading to less accurate $Vclay$ estimates (Rider, 1996).

$$Vclay = GRI = \frac{GR_{log} - GR_{min}}{GR_{max} - GR_{min}} \quad (2)$$

Where; GRI is the Gamma Ray Index, GR_{log} is the GR reading at the depth of interest, GR_{min} is the GR reading in clean sand (minimum value), and GR_{max} is the GR reading in pure shale (maximum value) (Kukal & Hill, 1986)

This method of $Vclay$ is the simplest approach and could potentially overestimate the clay content in the reservoir. For the purpose of this study, Equations (1) and (2) were used due to limitations mentioned earlier (lack of core data to calibrate, scarcity of the datapoints). The GR log may not always clearly differentiate between sands and shales, especially if there are radioactive minerals present in clean sands (Piava et al., 2019). Many assumptions fall under using GRI directly as $Vclay$, it assumes a linear relationship between GR readings and clay content. This assumption is often an oversimplification of the actual relationship (Bhuyan & Passey, 1994; Piava et al., 2019). In this reservoir, we are considering non-reservoir as both silt and shale potentially resulting in a higher clay content, and sand as reservoir. In addition, GR does not account for the presence of non-clay minerals in shales. Shales typically contain only 50-70% clay minerals, with the rest being silt-seized quartz, feldspars, and other minerals (Bhuyan & Passey, 1994).

I calculated the petrophysical log curve PHIE from total porosity (PHIT), as PHIT represents the total amount of pore space within a rock, including all voids, both connected and nonconnected that do not contribute to flow. Therefore, PHIE is more relevant and representative as it represents only "the interconnected pore space" (Bear, 1979) that contribute to fluid flow through the formation. I then computed $PHIE$ using Equation (5) at well level and applied to all unsampled wells that will be discussed in the following segment.

2.4.2 Porosity Analysis

Three main (key) wells have either sonic or density logs that we could compute porosity from. No neutron porosity curves were available from any of these wells. These three key wells are located in the periphery of the AOI (Figure 18). Although all three key wells have sonic log, the sonic is not as precise as the density. The sonic is a signal that travels through the different matrixes without differentiating them. Density log measures

the bulk density of the rock, which directly correlates to porosity. Density porosity has a more direct relationship to the rock matrix and pore fluid densities, leading to higher confidence in its result when matrix density is well known. Sonic porosity is highly sensitive to the type of fluids present in the formation, such as gas, oil, or water. Gas, in particular, causes significant drop in acoustic velocity. Often leading to an overestimated porosity. To account for this, we applied uncertainty to the porosity with a margin of error. The density log, however, is generally less sensitive to the type of pore fluid. Sonic logs are affected by the degree of compaction and cementation of the formation. The velocity of sound through rock can be influenced by rock compaction, particularly in deeper formation leading to inaccuracy in porosity estimates. Density logs are less influenced by these factors, resulting in more realistic and confident reflection of the porosity. Acknowledging the differences, I still had to compute the petrophysical porosity log curve using sonic porosity for the well that only had sonic log lacking density. I used the relationship between PHIT and Vclay of the key wells to get PHIE_base, PHIE_B+, and PHIE_B++ curves

From sonic porosity (PHIS):

$$PHIS = \frac{\Delta t_{log} - \Delta t_{mat}}{\Delta t_{fl} - \Delta t_{ma}} \quad (3)$$

Where $PHIS$ is the sonic porosity, Δt_{log} is the interval transit time of the formation (from the sonic log in (µs/ft), Δt_{mat} is the matrix interval transit time, Δt_{fl} is the fluid transit time, typically ~189 µs/ft. (Wyllie et al., 1956)

From the density porosity (PHID):

$$PHID = \frac{RHOM - RHOB}{RHOM - RHOFL} \quad (4)$$

Where $PHID$ is the density porosity, $RHOM$ is the matrix density of the rock (g/cm^3), $RHOB$ is the bulk density from the density log (g/cm^3), $RHOFL$ is the fluid density (g/cm^3) typically 1.0 g/cm^3 in water (Peters, 2012)

$$PHIE = PHIT - PHIT \times V_{Clay} \quad (5)$$

for all key wells with RHOB or DT log

Figure 18: Highlighting the three key wells in the AOI where property modeling and VOI analysis was focused on

Since the remaining wells in the project do not have density or sonic logs, we computed the porosity from key well-1 by getting the linear relationship between $PHIE$ and V_{Clay} (Figure 19), and applied to the remaining wells. To study the VOI based on the current field knowledge. We computed $PHIE_{Base}$ from the well with sonic porosity only (i.e., well-1) and excluded the two other key wells.

1. **PHIE Base case Petrophysical Workflow:**
    I. Compute key well1 with sonic porosity Equation (3) → $PHIT$
    II. Compute $PHIE$ at key well-1
    III. Plot $PHIE$ vs V_{Clay}
    IV. Linear relationship to apply to remaining wells

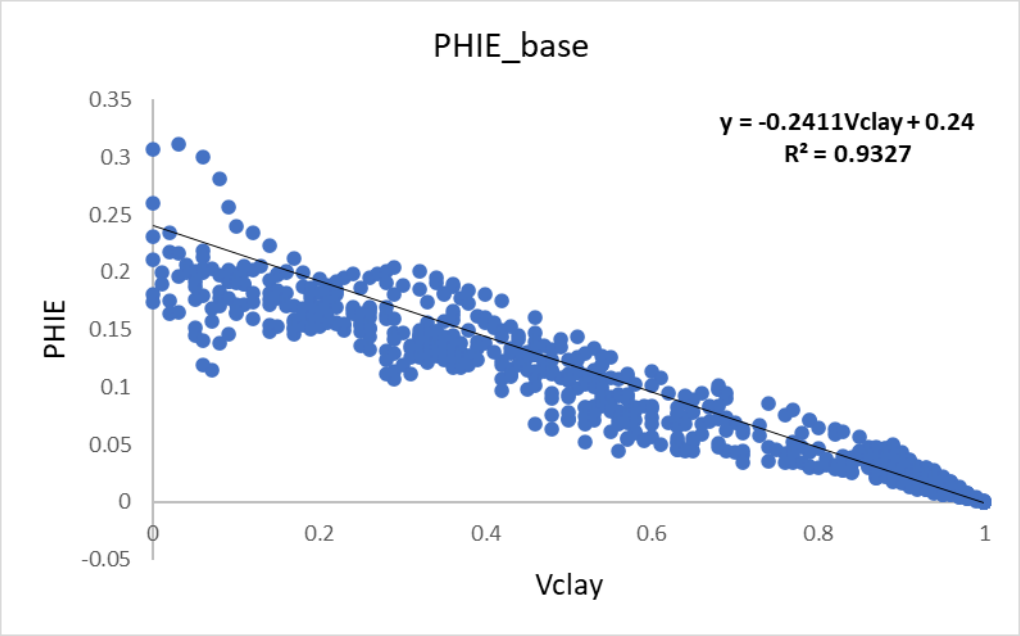

Figure 19: PHIE vs Vclay from key well no.1 to get the linear relationship for PHIE_base

In this case, I chose the linear relationship instead of the plots with polynomial degree 2 because these will result in negative PHIE if used otherwise. In addition, before deciding on using sonic porosity (PHIS) as the petrophysical log for key well-1, I compared the density porosity from the two other key wells (PHID) and plot them against their sonic log to get a relationship for porosity that can be used at key well-1. The petrophysical log response is shown in Figure 20. The PHIS (in blue) when compared to PHID_sonic (in blue), it gave a significantly higher porosity by over 100%.

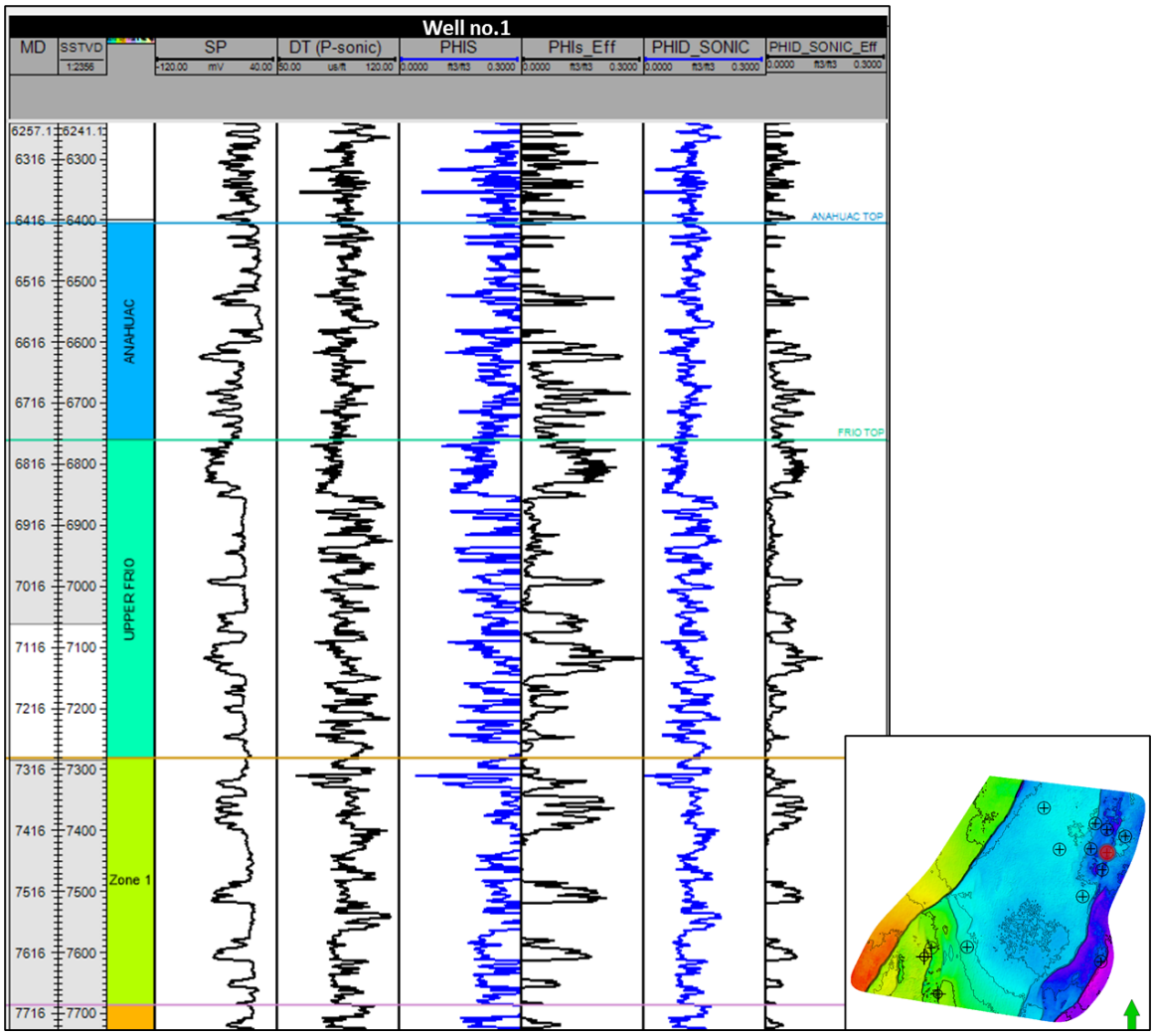

Figure 20: Key well-1 displaying sonic porosity (PHIS) compared to PHID_SONIC (regression relationship between density porosity and sonic). PHIS was used instead for better results

Again, for VOI analysis, the following workflow was applied for the B+ model by adding key well-2 to the base case to evaluate any significant changes in the porosity modeling.

2. PHIE (B+) Petrophysical Workflow:

V. Compute density porosity for key well-2 with Equation (4) → *PHIT*

VI. Compute $PHIE$ at key well-2

VII. Plot $PHIE$ vs V_{Clay} (Figure 21)

VIII. Polynomial 2nd deg relationship to apply to remaining wells

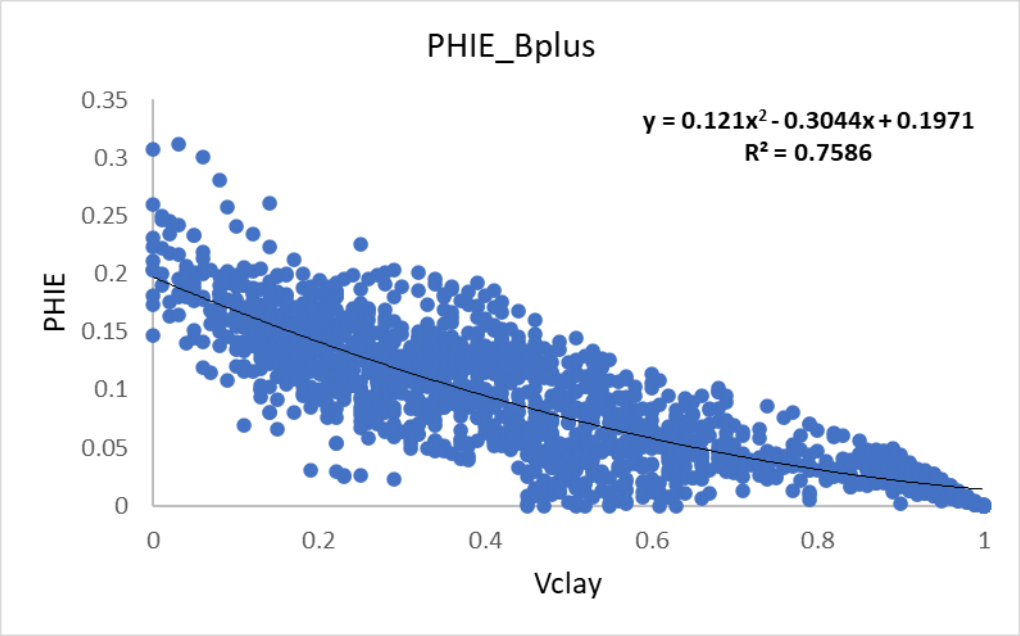

Figure 21: PHIE_B+ case: PHIE vs Vclay plot from key well no.2 to get the linear relationship for PHIE_B+

3. PHIE (B++) Petrophysical Workflow:

IX. Compute density porosity for key well-3 with Equation (4) → $PHIT$

X. Compute $PHIE$ at key well-3

XI. Plot $PHIE$ vs V_{Clay} (Figure 22)

XII. Polynomial 2nd deg relationship to apply to remaining wells

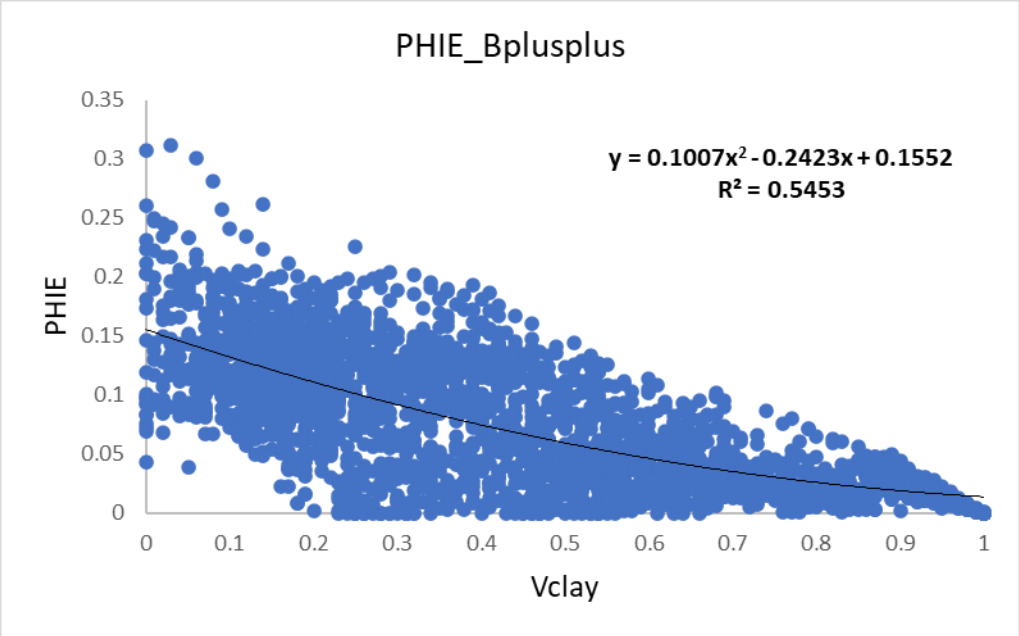

Figure 22 – PHIE_B++ case: PHIE vs Vclay from key well- 3 to get the linear relationship for PHIE_B++

2.4.3 Challenges

The reservoir quality is the main challenge in this potential GCS site as shown in the plots where the porosity is relatively decreasing with new wells added. There are two existing wells with neutron porosity (one of them in sandstone matrix); however, I did not work on the correction for density porosity (PHID) and neutron porosity (NPHI). This correction is generally related to gas effect correction. By applying the correction this would affect the porosity even negatively. The porosity (Ø) is equal to the square root of the average of the squared values of NPHI ($\emptyset_N$) and density porosity ($\emptyset_D$) (Bhuyan & Passey, 1994) (Equation 6) that could result in lower porosity value than density porosity.

$$\emptyset = \sqrt{\frac{\emptyset_N^2 + \emptyset_D^2}{2}} \quad (6)$$

2.4.4 Permeability Analysis

The permeability was calculated from a porosity-permeability transform from a nearby field in the Frio Formation that we believe represent a similar geological characteristics (Equation 7). Other permeability transform functions were tested using a different from literature review (McRae et al., 1995) explaining the different rock types with their poro-perm relationship as a comparison (see Appendix B). In addition, the closest transform is from sidewall core plug from two wells around the AOI but the data was highly scattered and uncertain with a coefficient of determination (R^2) of 0.27 as seen in Figure 23(b), whereas the applied poro-perm for the project is honoring three wells with an R^2 of 0.41 (Figure 23(a)), therefore it was more realistic to use the transform in Equation (7) from the nearby field.

$$k = 0.0689e^{0.2355\emptyset} \quad (7)$$

(a)

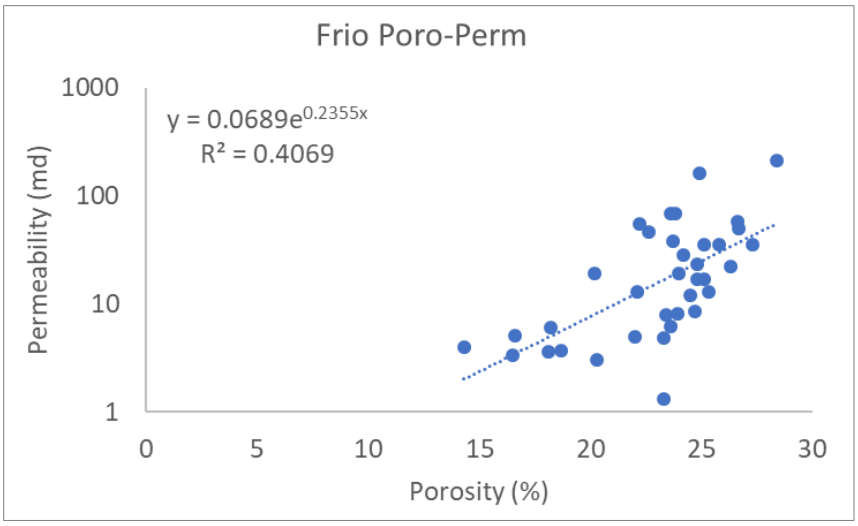

(b)

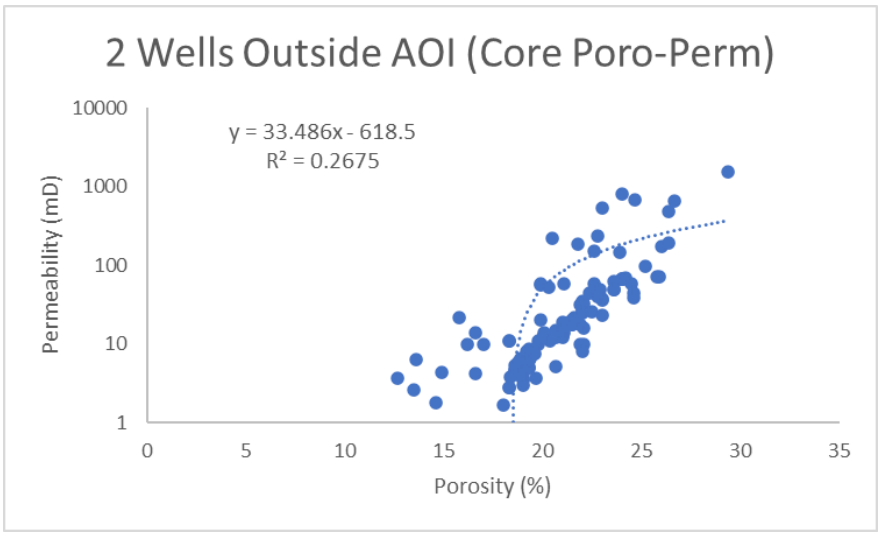

Figure 23: (a) Poro-Perm transform from a nearby field applied in the study (b) Two wells outside the AOI with core plug Poro-Perm with a lower R^2 (scattered and uncertain) that was not used

Chapter 3: 3D Geocellular Modeling for Upper Frio Zone

3.1 Reservoir 3D Geomodeling

The static model was built in Petrel software. The structural framework was done using Corner Point Gridding workflow to model and QC the faults. The extend of the AOI for geomodelling is shown in Figure 24.

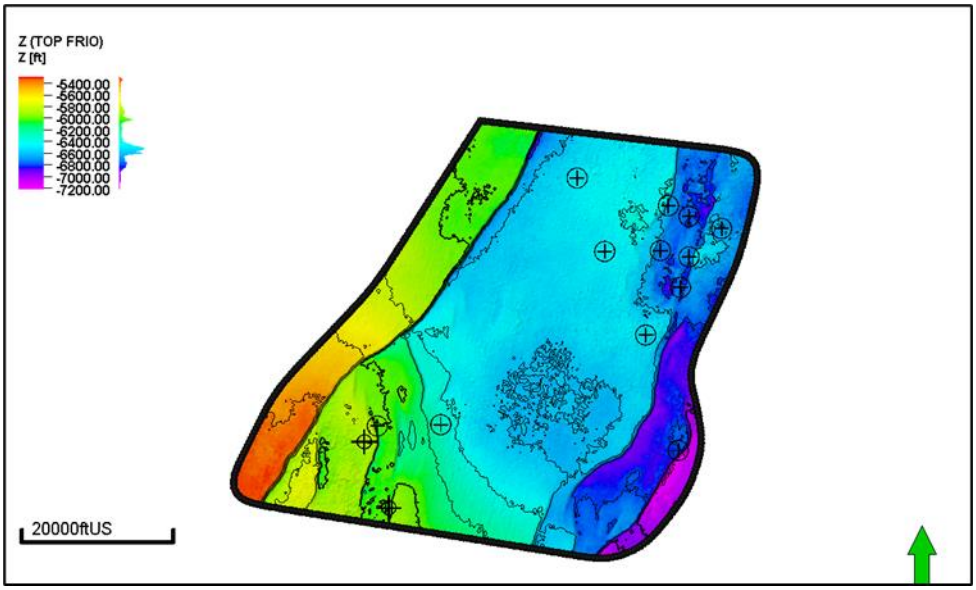

Figure 24: Boundary polygon indicating the extend of the AOI used for modeling

Prior to implementing corner point gridding, structural gridding was performed using the *Structural Framework* in Petrel. However, the resulting 50 layers in the Upper Frio zone (Top Frio - Frio FS1) within the 3D geomodel consistently exhibited discrepancies that prevented the structural model from being effectively utilized for property modeling in Petrel. Consequently, the workflow was shifted to corner point gridding. Additionally, the Petrel version was updated to the newer version 2023.6 to run a Pillar gridding framework for creating the final structural grid.

3.1.1 3D Grid and Structural Modeling

Table 3 summarizes the input for the 3D modeling framework. The 14 available legacy wells, the two horizons that were seismically interpreted, and the 35 faults also interpreted seismically. Finally, the main input is the measured porosity curves to run simulations for the CO_2 plume and pressure build up.

Table 3: Summary of input data available for constructing 3D geologic modeling

Data	Number of Data Available	Data Origin
Horizons	2	Seismic interpretation
Faults	35	Seismic interpretation (All interpretted by Carlos and Karen)
Wells	14	
Lithotype Curve (Vclay)	14	Well log interpretation
Porosity Curve	14	Well log interpretation

The Upper Frio zone's average thickness is 500ft. In order to capture 5ft per cell the model would have require 100 layers. With these grid parameters and resolution, the dynamic model would not be able to handle the data processing. Therefore, it was necessary to reduce the number of layers to 50, capturing 10ft thickness per cell instead and thereby making the grid coarser. The new grid resolution is shown in Table 4, where the new grid cell size is 3,568,000. If we had used the finer grid, the simulation runs would take longer than anticipated, and this was beyond the project scope. Also, Figure 25 displays the faults in one of the surfaces (Top Frio) that were included for 3D geomodelling. Figure 26 shows the resulting horizons of the Top Frio and Frio FS1. In

these horizon maps, the green to red color range represents shallow depths, and the blue to purple range represents deeper depths.

Table 4: 3D Grid resolution parameters

Grid cells (nI x nJ x nK)	320 x 223 x 50
Grid nodes (nI x nJ x nK)	321 x 224 x 51
Total number of grid cells:	3568000
Total number of grid nodes:	3667104
Number of geological horizons:	51
Number of geological layers:	50
Total number of 2D cells:	71360
Total number of 2D nodes:	71904
Total number of defined 2D nodes:	50940

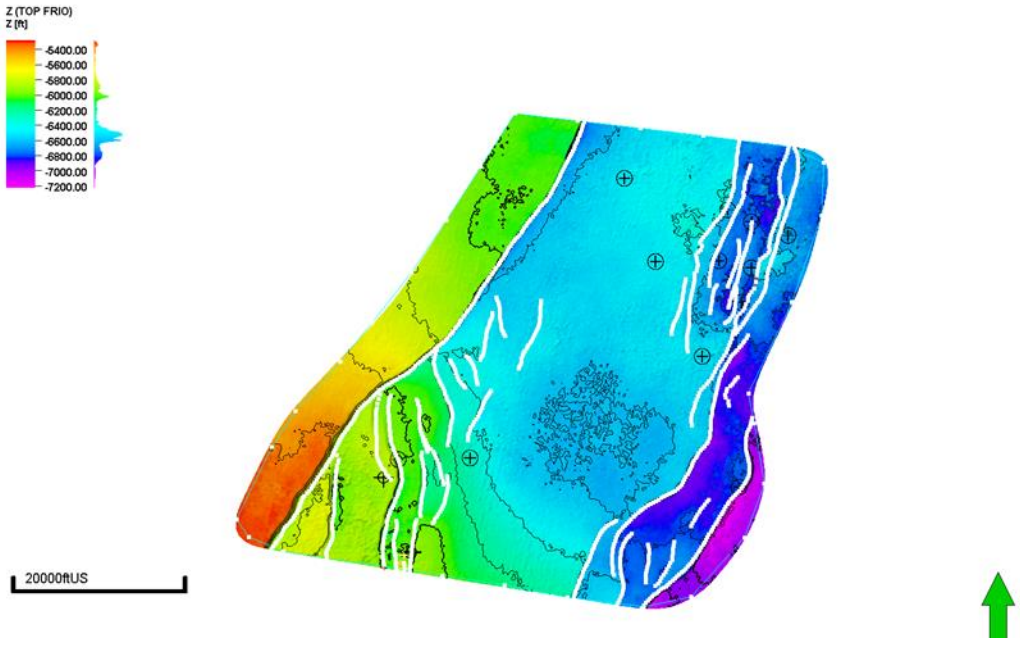

Figure 25: Top Frio depth map, showing the 35 faults included in the geologic modeling

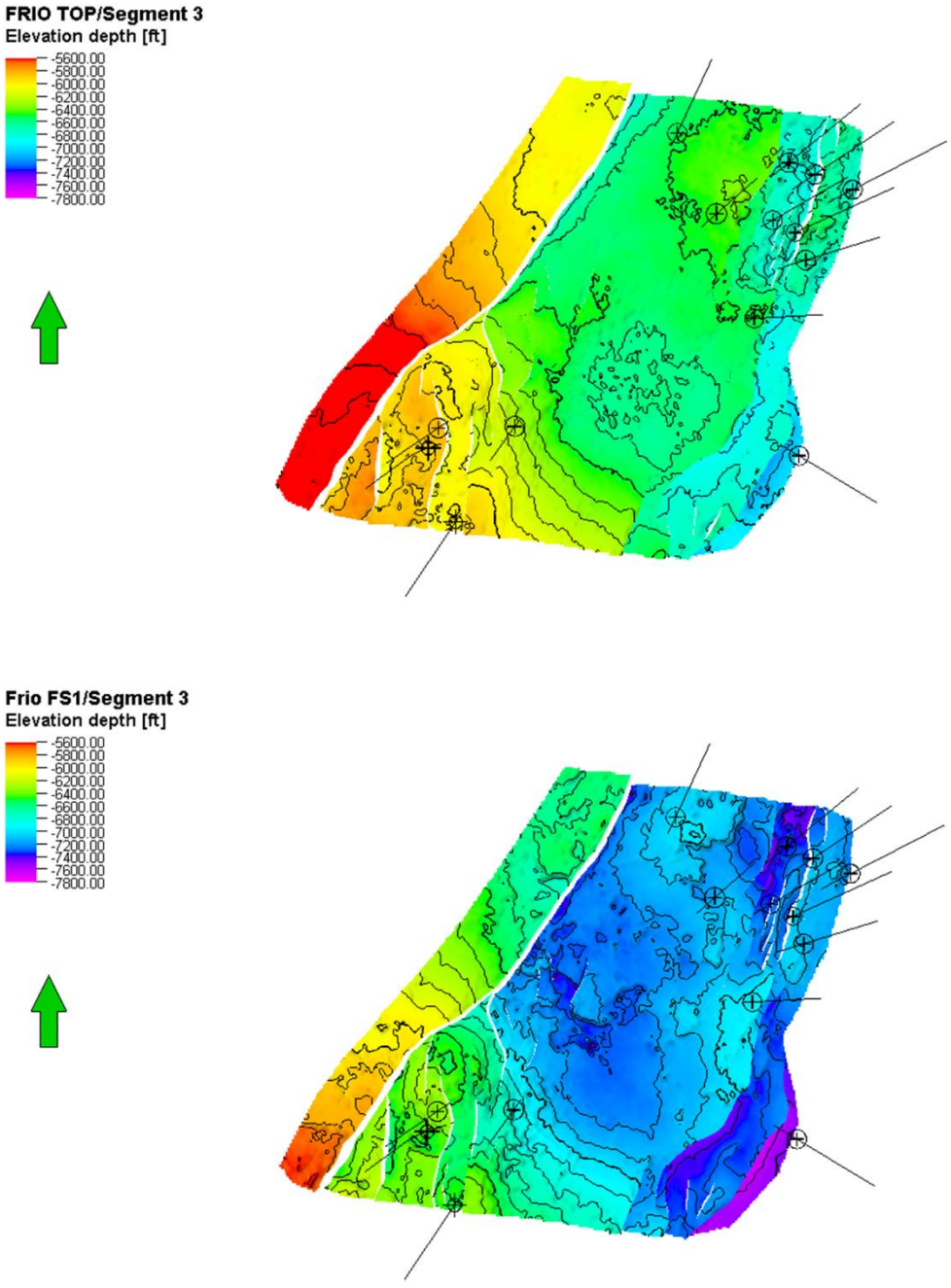

Figure 26: Frio top (above) and FS1 (below) horizons in 3D structure model. The blue represents deeper depth and the green up to red color represent shallower depth

3.1.2 Fault modeling

Fault modeling was crucial for accurately characterizing the subsurface structure, which directly impacts the feasibility and safety of geological carbon storage (Dommisse, 2024). The fault modeling framework applied incorporated key elements including the use of 3D seismic data to model the faults and reference horizons. This approach provided a reliable basis for fault editing, ensuring that the structural model captured the essential elements necessary for evaluating the geological integrity of the storage site.

A significant amount of quality control (QC) was undertaken in the 3D workflow (see Appendix C). The faults had previously been interpreted seismically in time. In the structural modeling module of Petrel, the fault framework was originally built under *structural framework* and moved to *corner point gridding* within the Pillar Gridding. In Figure 27, the faults have already been QC'd and adjusted through truncation and merging using the Edit Fault Model tool palette in Petrel. A total of four faults were merged into two, with selections based on the dominant fault and the dip/orientation of the faults in relation to the surrounding faults. The number of faults were truncated to the regional master fault in Figure 27. The reasons to follow this process include the following:

- Improved modeling of the 3D grid and avoidance of discrepancies
- Ensuring that the workflow in Petrel runs properly by adjusting all faults

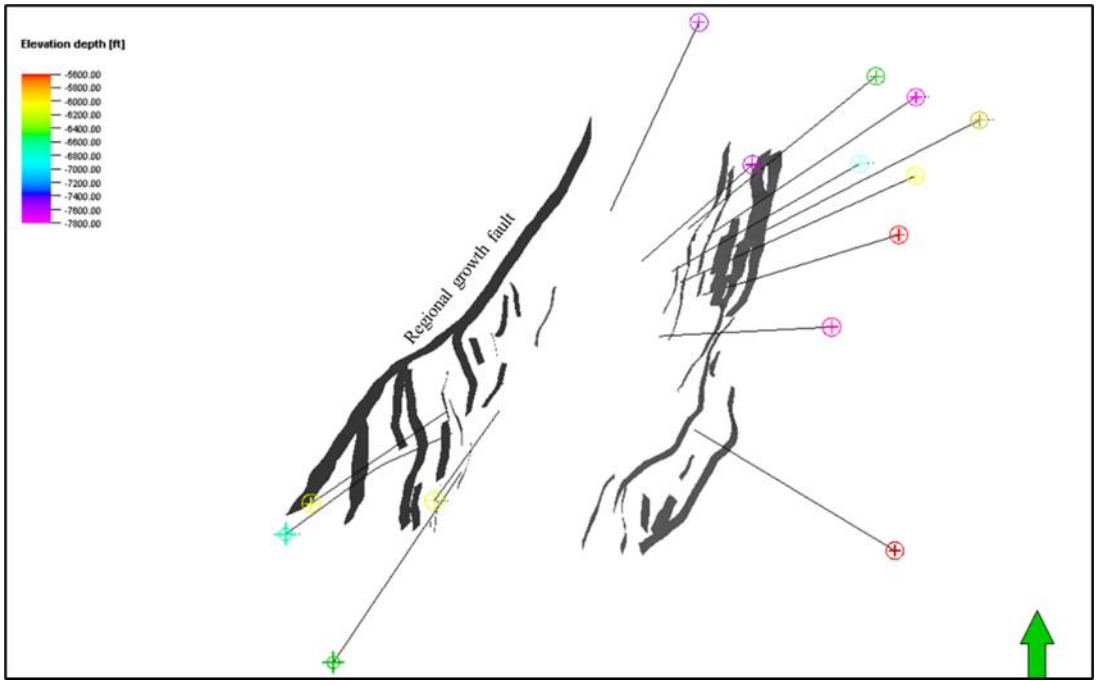

Figure 27: The 35 faults in the AOI showing the regional growth fault on the west

Further QC and fault cleaning were necessary as shown in Figure 28, where the fault-horizon lines were used as input in the “Horizons” to edit the grid in the fault modeling process. Finally, Figure 29 is the resulted structural model of the Upper Frio zone shown in dark grey.

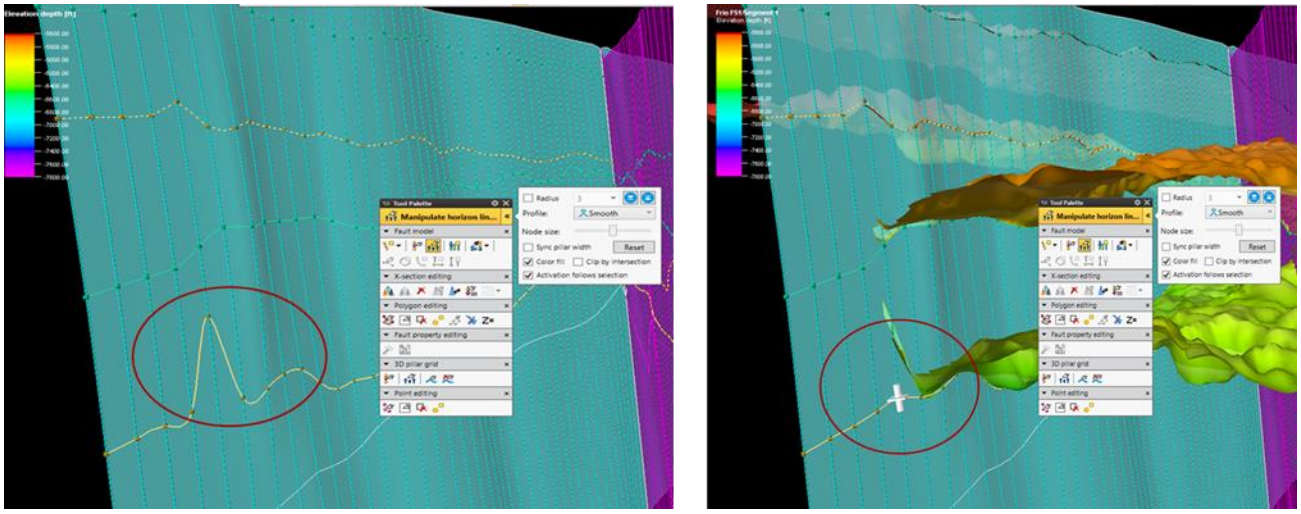

Figure 28: Before and after adjusting the horizon line. Adjustment of the horizon line circled in red

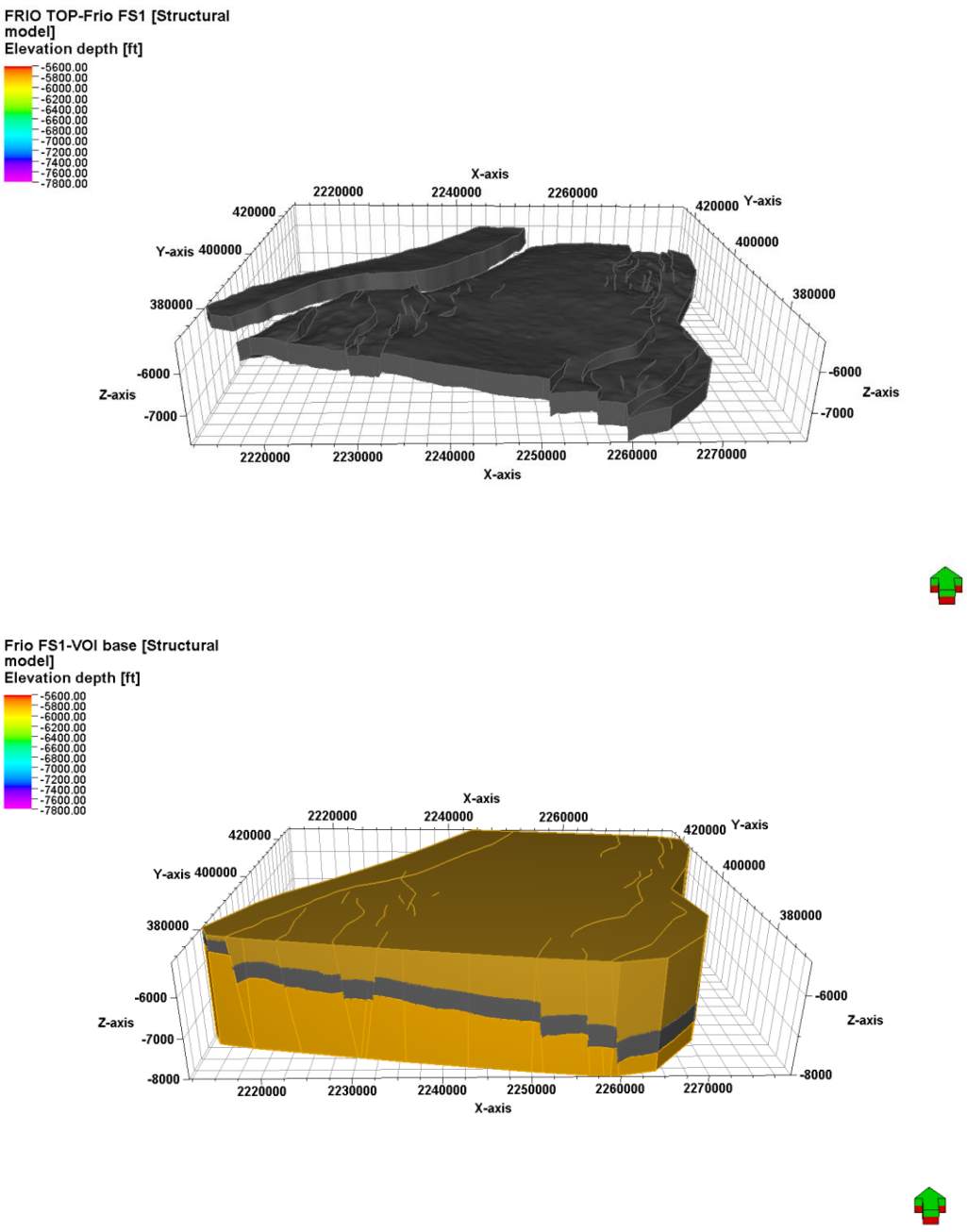

Figure 29: Target injection zone visualization of the Top Frio - Frio FS1in dark grey. This is the structural model under Structural Framework in Petrel (Geospace view).

3.2 PETROPHYSICAL PROPERTY MODELING

Property modeling is considered an important step in 3D geomodelling. It is carried out by filling grid cells with discrete or continuous properties. Detailed facies modelling effort was not performed for this project; however, sandstones were separated from shales/mudstones at the well level, based on a sand cut-off at GR and SP logs.

The 3D model was populated with porosity values using GRFS stochastic method, a well-known geomodeling technique that effectively honors available data points, particularly under conditions of data scarcity. Through a sequential simulation process, each location is generated while considering both previously simulated points and actual well data. By utilizing this approach, uncertainty is characterized effectively, which is crucial when dealing with sparse datasets. Multiple realizations can be produced using this method, thereby enhancing the understanding of variability and uncertainty within the model.

3.2.1 Well log Upscale and Data Analysis

Porosity logs were upscaled using arithmetic method in Petrel. Figure 31 shows the input well log and the upscaled porosity, honoring the same response.

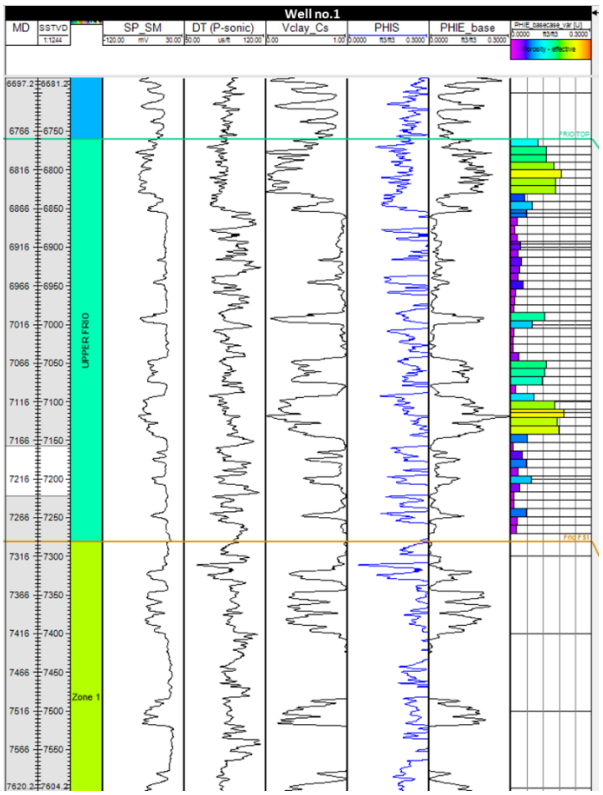

Figure 30: The resulted upscaled log PHIE_base of the key well- No1 consistent with its input well log. The blue log is the PHIT. The datum is flattened in Anahuac shale.

When performing data analysis in Petrel, running a normal score transformation of the data before running the GRFS simulation algorithm. Normal score transformation is used with caution particularly since the project has limited input data, because the distribution of the property is forced to match the distribution of the input exactly (that is, both the position and the relative height of the histogram bars). You can see some of the results of these histogram later in this section. After the data is normal scored, the variograms are set and ran the simulation. In Petrel, when the simulation is complete, the data is back-transformed automatically from the normal distribution to the original distribution as seen in Figure 32.

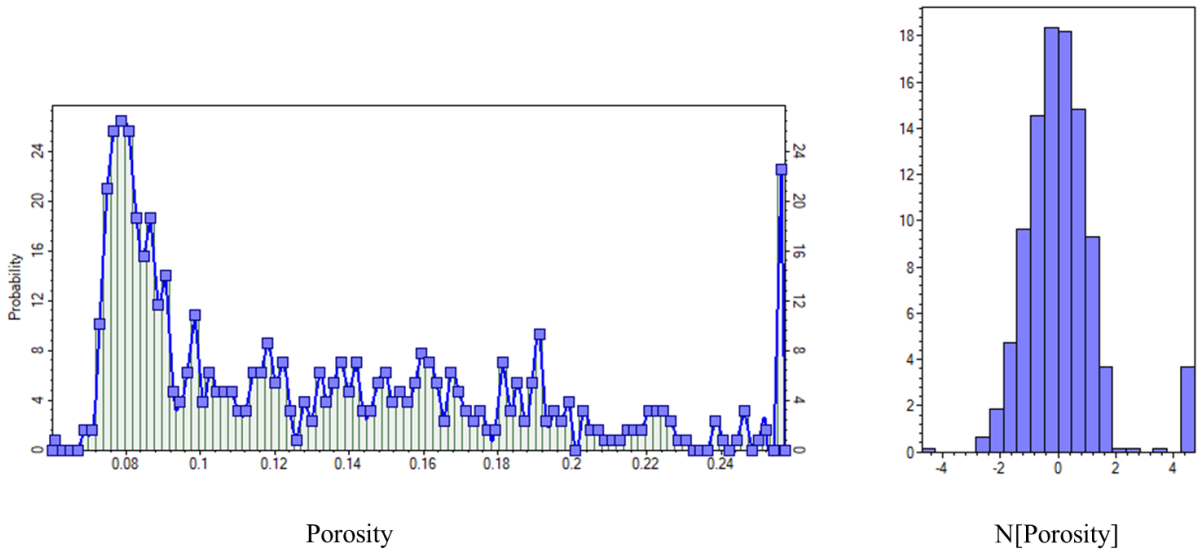

Figure 31: Normal score transformation performed in Petrel modeling background for running stochastic simulation (property modeling). The histogram on the right shows the transformed values (standardized to follow a normal distribution with a mean of 0 and standard deviation of 1)

Figure 32 indicates that a value is picked and simulated from the normal distribution; the histogram with the transformed values is standardized to follow a normal distribution with a mean of 0 and standard deviation of 1. Then after the geostatistical algorithm has been run, the picked value is back-transformed to its original distribution.

After the data had been back-transformed from the data analysis, the vertical variogram range was set according to the well logs, and the horizontal (lateral spatial correlation) major and minor variogram ranges were theoretically estimated based on the current geologic knowledge of the field and by analogy with a nearby field. The values were established at 20,000ft for the base case, 15,000ft for the low case, and 25,000 ft for the high case, as shown in Tables 5, 6, and 7. The major orientation direction (azimuth

angle) was set to the default value of 0°. The same workflow was applied to each case following the same completion of the data analysis.

3.2.2 Property (Porosity) Modeling

Below, the workflow and approach are presented for executing a total of 21 realizations in the static modeling process. These realizations are used to calculate the uncertainty of porosity, based on the standard deviation from the mean and on variogram that deviate from the base value.

Effect of variogram alone:

I. Upscale $PHIE_{base}$

II. Perform data analysis

III. Run $PHIE_{base}$ porosity model with *base* variogram from Table 5

Table 5: Basecase variogram ranges for property modeling

Basecase/Varigoram	**Base**	**Low**	**High**
Maximum range (ft)	20,000	15,000	25,000
Minimum range (ft)	20,000	15,000	25,000
Vertical range (ft)	17	16	18

IV. Upscale $PHIE_{B+}$

V. Perform data analysis

VI. Run $PHIE_{B+}$ porosity model with *base* variogram ranges from Table 6

Table 6: B+ variogram ranges for property modeling

Bplus/Varigoram	**Base**	**Low**	**High**
Maximum range (ft)	20,000	15,000	25,000
Minimum range (ft)	20,000	15,000	25,000
Vertical range (ft)	13	12	14

VII. Upscale $PHIE_{B++}$

VIII. Perform data analysis

IX. Run $PHIE_{B++}$ porosity model with *base* variogram range from Table 7

Table 7: B++ variogram ranges for property modeling

Bplusplus/Varigoram	**Base**	**Low**	**High**
Maximum range (ft)	20,000	15,000	25,000
Minimum range (ft)	20,000	15,000	25,000
Vertical range (ft)	16	15	17

1. Effect of porosity alone:

I. Create *PHIE* at global well log under the wells folder in Petrel

$$PHIE_{high} = PHIE + std \quad (9)$$

$$PHIE_{low} = PHIE - std \quad (10)$$

For the std is ±0.08 for basecase, ±0.06 for B+, ±0.05 for B++ according to the statistics of the well log input data

II. Upscale $PHIE_{high}$ with 12 well for basecase, 13 wells with B+, 14 wells with B++

III. Perform data analysis and keep same variograms for initial basecase models

IV. Run the $PHIE_{high}$ property modeling for PHIE_base, PHIE_B+, and PHIE_B++

V. Upscale $PHIE_{low}$ with 12 well for basecase, 13 wells with B+, 14 wells with B++

I. Perform data analysis and keep same variograms for initial basecase models

II. Run the $PHIE_{low}$ property modeling for PHIE_base, PHIE_B+, and PHIE_B++

2. Effect of combination variogram and porosity together

I. In each case $\boldsymbol{PHIE_{high}}$

a. Basecase → use variogram from basecase high

b. B+ → use variogram from B+ high

c. B++ → use variogram from B++ high

II. In each case $\boldsymbol{PHIE_{low}}$

a. Basecase → use variogram from basecase low

b. B+ → use variogram from B+ low

c. B++ → use variogram from B++ low

The resulted histograms of base case with low and high variogram ranges are displayed in Figure 33 as an example, where the property model is in purple, and it is honoring and consistent with the upscaled (in green) and input well log (in red) (All other 18 resulted histograms can be seen in Appendix D).

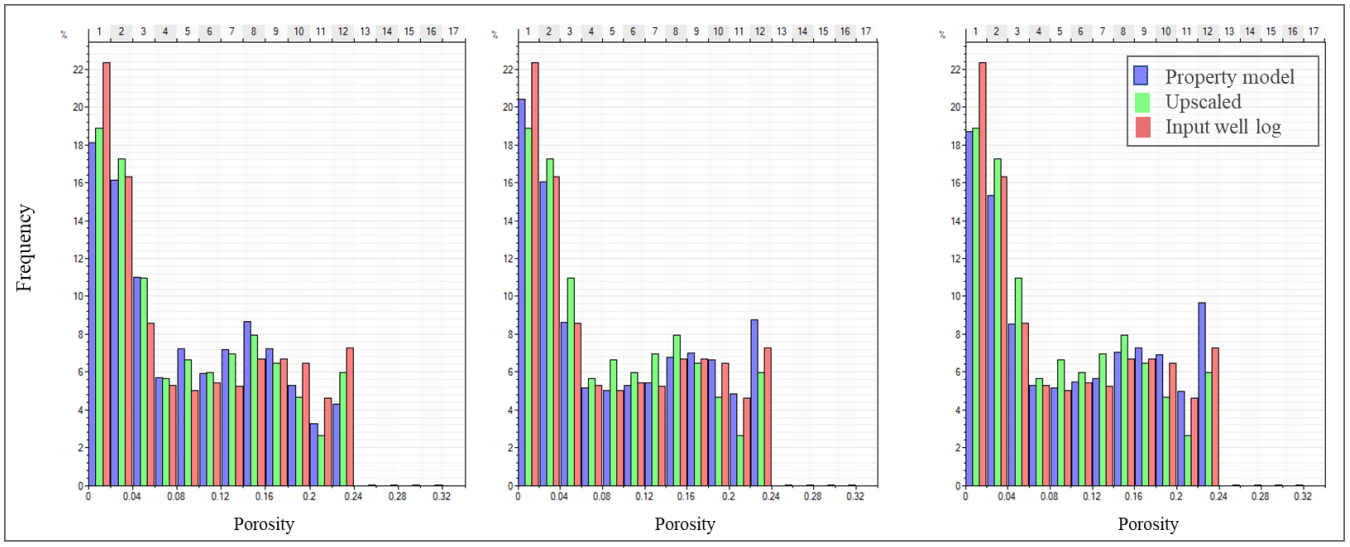

Figure 32: The effective porosity with low and high variogram ranges in the base case (Left histogram: base variogram at 20,000 ft, middle: low at 15,000, and right: high at 25,000 ft)

3.3 UNCERTAINTY ANALYSIS

To study the reservoir quality and the uncertainty of the property, the previously described approach was employed. A very high level of uncertainty was observed, stemming from the limited data and the wide well spacing. Consequently, the variogram inherently reflects high uncertainty due to the lack of closely spaced data points. It does not provide a robust estimate of small-scale variability since the smallest available distances (approximately 3000ft) remain quite large. As a result, the variogram model is more uncertain, particularly at short distances. In Figure 34, the three key wells are displayed alongside the effect porosity mode, which was extracted from 3D property model (shown on the far-right log). Well-1 was utilized for the base model, ensuring ethe extracted effective porosity honors the input data. In contrast, well-2 and well-3 represent total porosity since they were not incorporated into the base modeling.

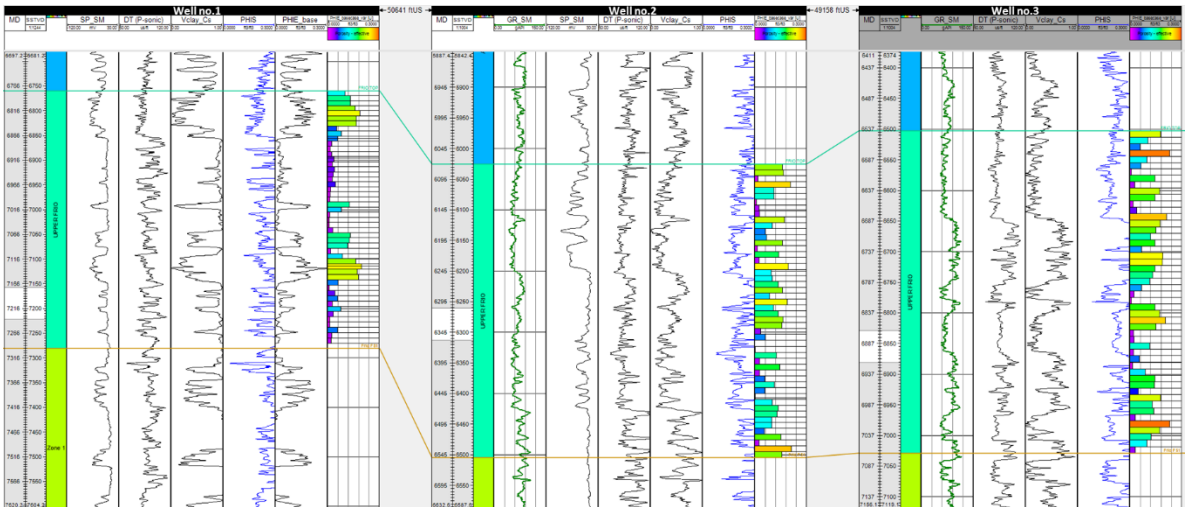

Figure 33: The resulted effective porosity model displayed as an extracted log (in the far right for the base case model) from the 3D grid in Petrel. Well-2 and well-3 are honoring its total porosity instead of PHIE when stochastically modeling in 3D property modeling since these two wells were not sampled in the base case model. The datum is flattened on Anahuac shale.

3.3.1 Results and Discussion

In the following figures, the effective porosity legend is set to a minimum of 2% and a maximum of 32%, reflecting the lowest and highest porosity values obtained from all 21 realizations. Red indicated the highest porosity value, while purple represents the lowest. All figures follow the same arrangement: the base porosity is displayed on the left, the low is in the middle, and the high on the right. Figures 35, 36, & 37 show the effective porosity maps for each main case, with varying the variogram ranges illustrating both the low and high results relative to the base case (as detailed in Tables 5, 6 & 7). Figures 38, 39 & 40 present the change in porosity values based on their standard deviation from the mean while maintaining the base variogram range at 20,000ft. Figures 41, 42 & 43 display the corresponding high porosity and high variogram values, as well as the combined low porosity and low variogram values. Additionally, the global seed was to 1342, defining the starting point for random number generation in the algorithm to ensuring consistency across 21 realizations. (Note: Although there are 27 total realizations in the figures below, some are displayed twice for consistency and comparison). For a large well spacing there would be limited data points to establish spatial continuity and observe variability between wells at short distances. Due to the limited data sampling, which leads to greater heterogeneity, the resulted 3D porosity maps do not exhibit any clear trend or pattern leading to low quality reservoir.

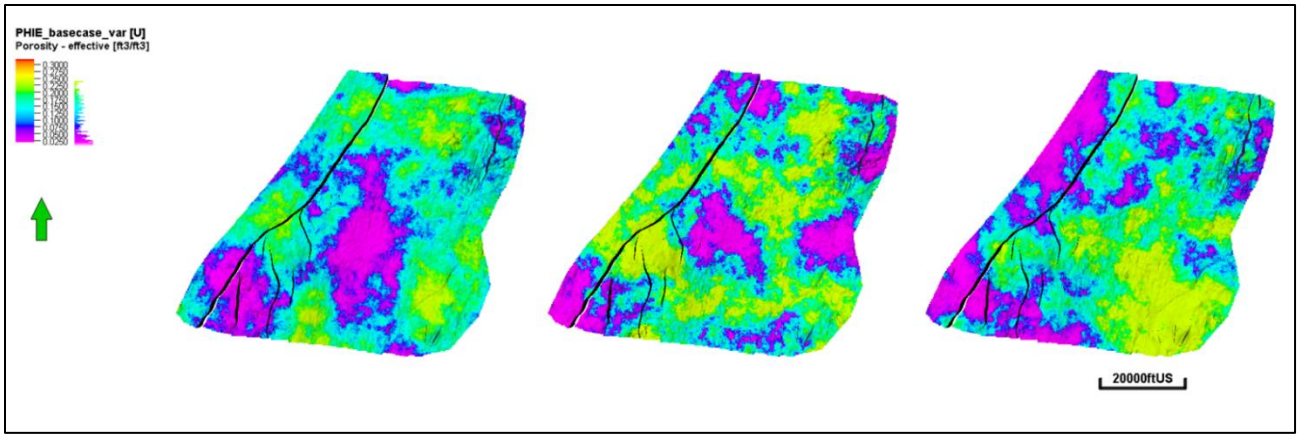

Figure 34: PHIE_basecase with variogram range (base at 20,000ft, low at 15,000ft and high at 25,000ft respectively)

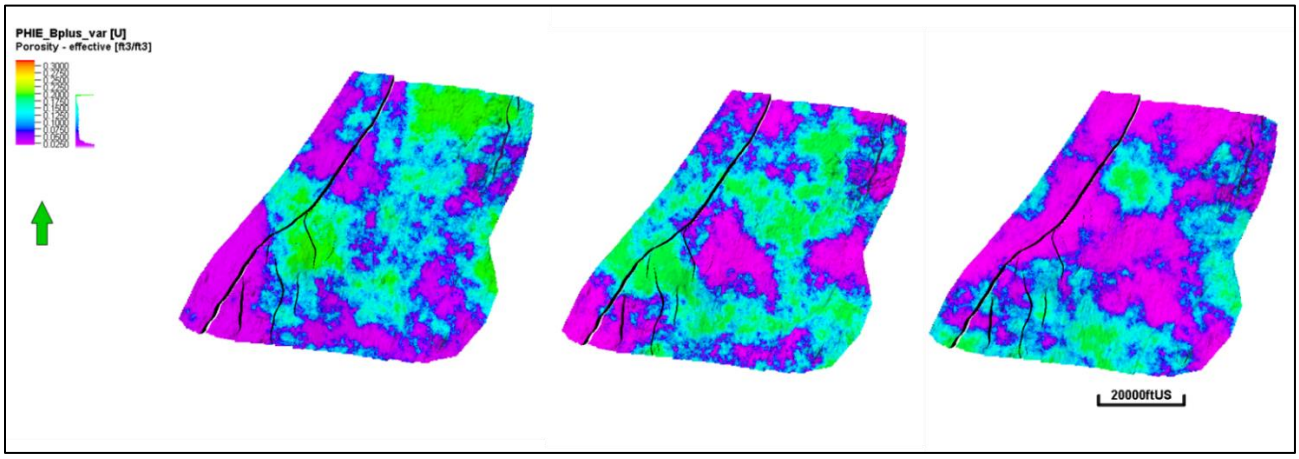

Figure 35:PHIE_ B+ with variogram range (base at 20,000ft, low at 15,000ft and high at 25,000ft respectively)

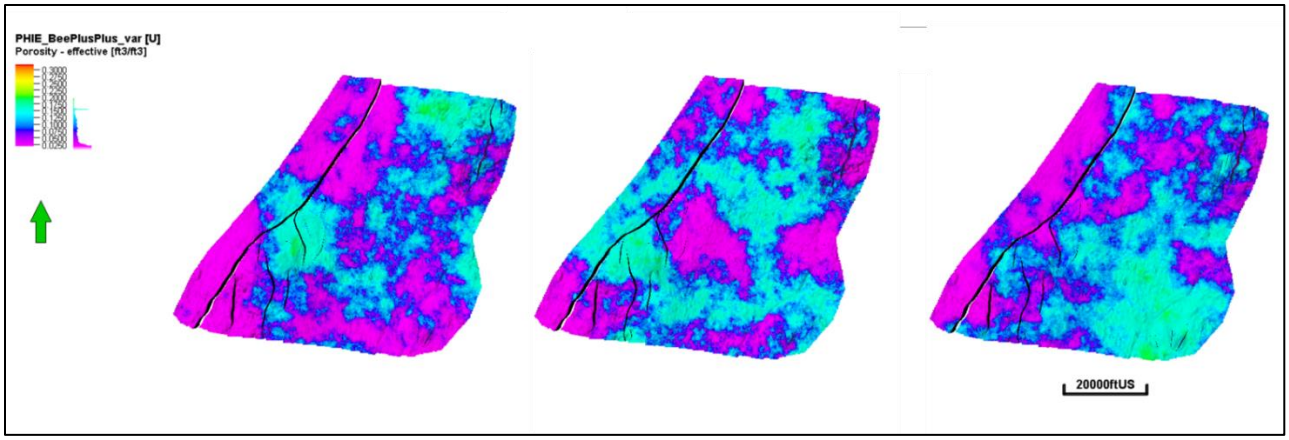

Figure 36: PHIE_B++ with variogram range (base at 20,000ft, low at 15,000ft and high at 25,000ft respectively)

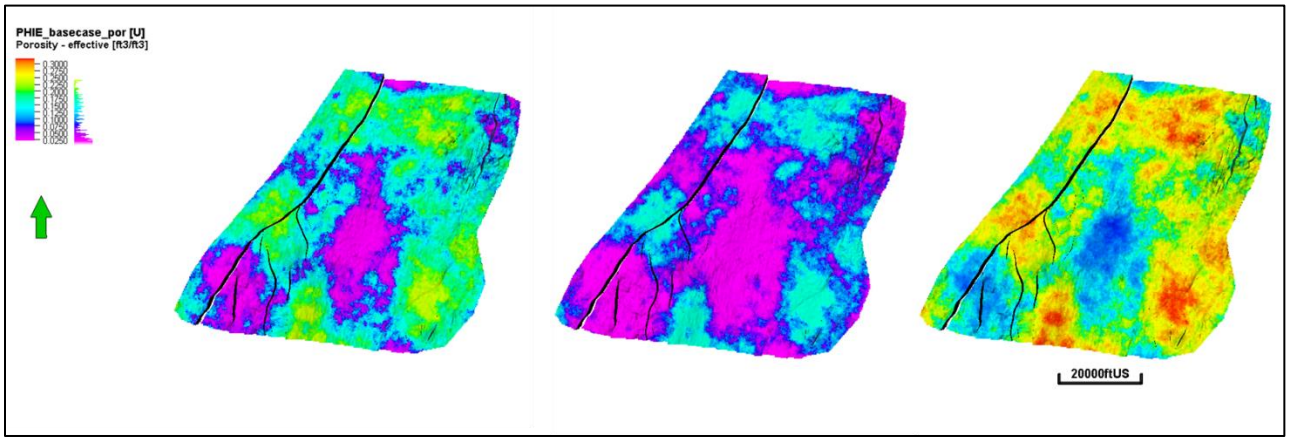

Figure 37: PHIE_basecase with low and high porosity respectively based on +/- 0.08 std from the mean with the same base variogram at 20,000 ft

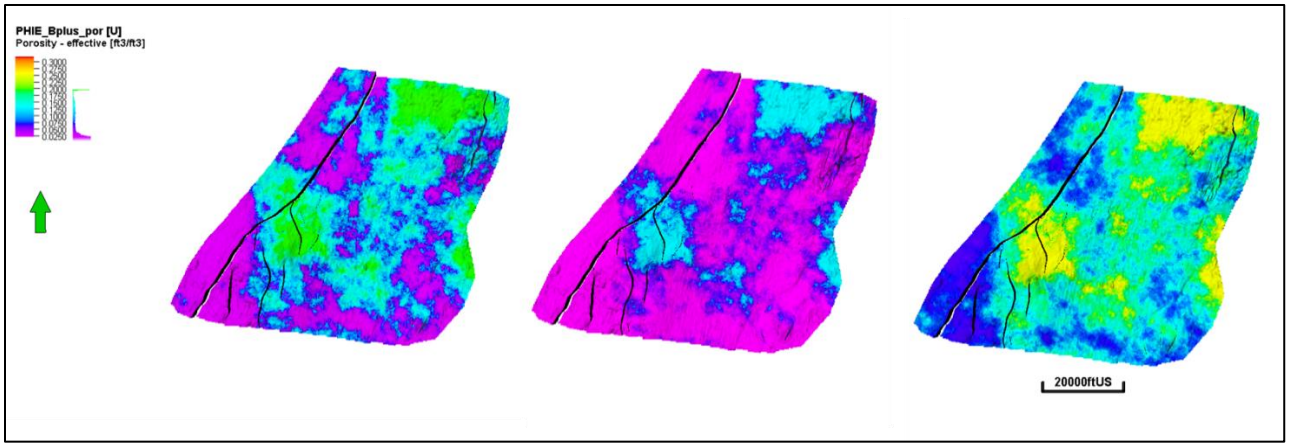

Figure 38: PHIE_B+ with low and high porosity value based on +/- 0.06 std from the mean with the same base variogram at 20,000 ft

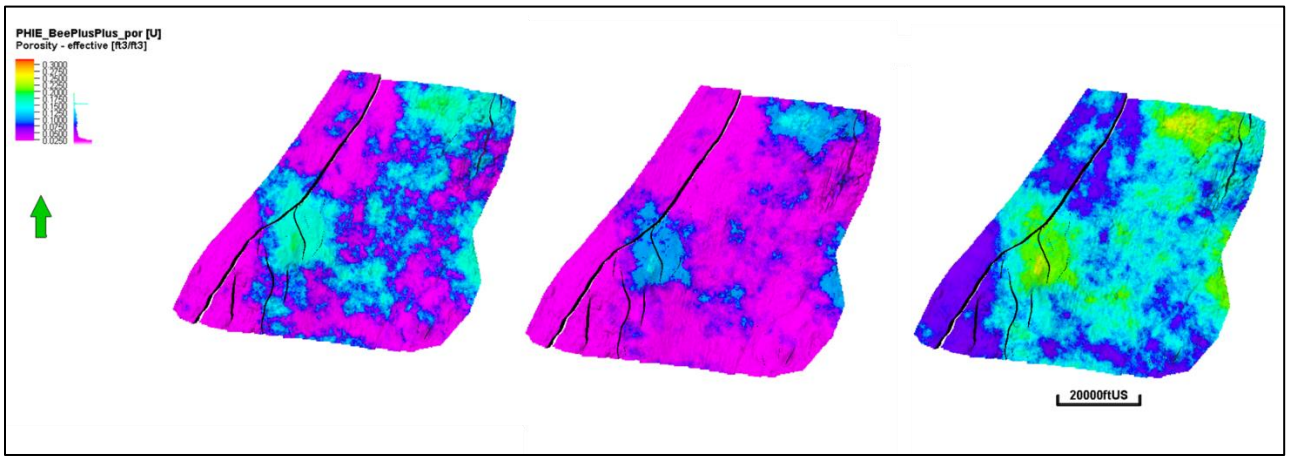

Figure 39: PHIE_B++ low and high porosity value based on +/- 0.05 std from the mean with the same base variogram at 20,000

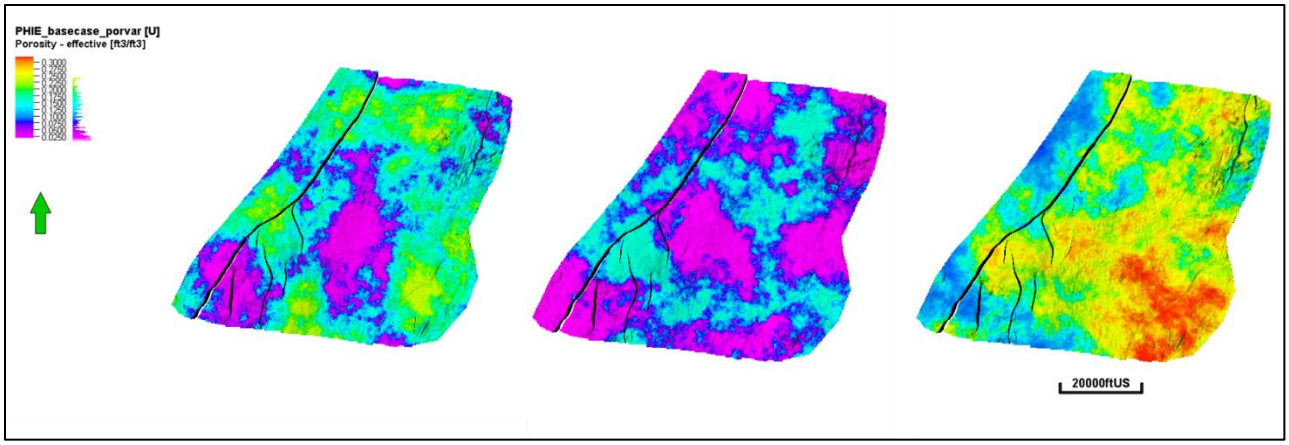

Figure 40: Basecase with porosity and variogram combined

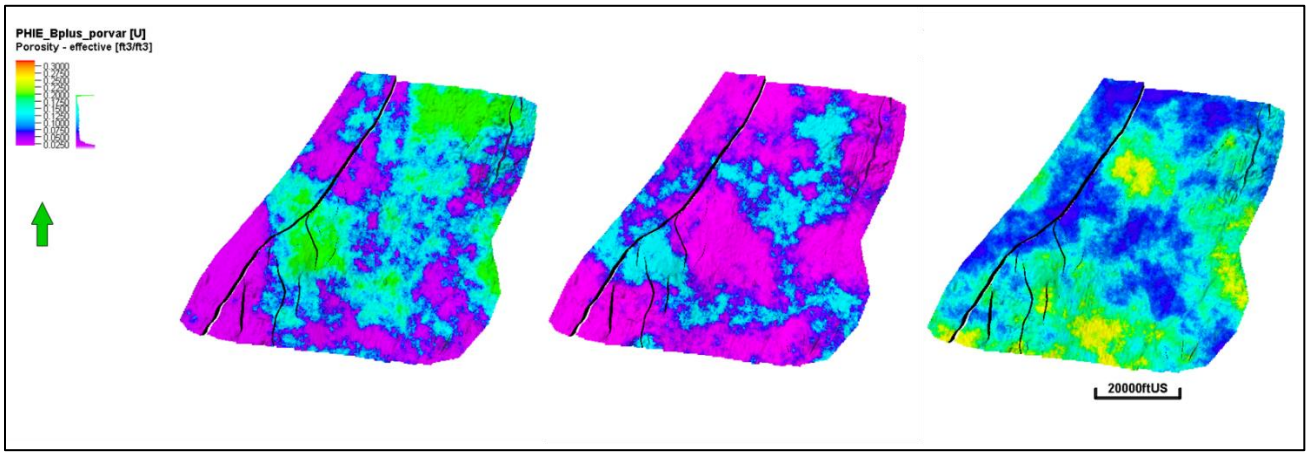

Figure 41: B+ with porosity and variogram ranges combined

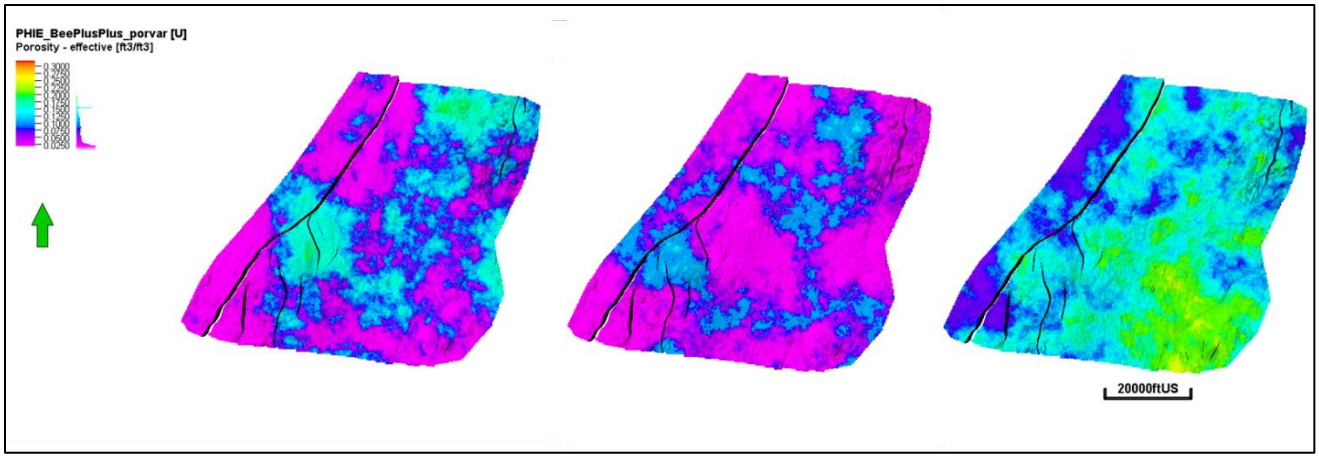

Figure 42: B++ with porosity and variogram ranges combined

Chapter 4: CO_2 Storage Capacity Analysis- Simulation Study

The dynamic modeling workflow for geological carbon storage (GCS) aims to simulate CO_2 injection and its distribution within stratified reservoirs, ensuring storage efficiency while assessing associated risks. Key parameters include porosity, permeability, and boundary conditions, all of which directly impact the CO_2 plume migration, pressure build up, storage capacity, and the AoR delineation. By accounting for site-specific factors, such as reservoir heterogeneity and injectivity, the model provides insights into the optimal storage potential while minimizing risks associated with CO_2 leakage and ensuring compliance with Class VI permit requirements (Hosseini et al., 2024).

4.1 Dynamic Reservoir Modeling

After building the static modeling of porosity and permeability, these properties were exported for simulation study. Note that there was a total of 21 static realizations, but only 15 realizations were used for the simulation study. The remaining 6 were excluded due its very low porosity and permeability leading to injection rate and well bottom-hole pressure limitations; hence they are not going to be part of the VOI analysis. Dynamic simulations were conducted using Computer Modeling Group (CMG) software to predict storage capacity within the injection zone. The primary input parameters for the simulation were porosity and permeability (results described in the previous chapter). Due to low quality reservoir rock, the injection rate was set at 0.1 $MtCO_2$/year for two injection wells, with their locations determined by the highest net pay map values (Figure 44), the portions of the gross pay that meet local criteria for pay (such as porosity, permeability) are net pay. To prevent model crashes due to numerical divergences, constraints were imposed on the model's bottom-hole pressure based on a 90% of fracture gradient of 0.7 psi/ft. This limitation accounts for the low porosity and permeability of the reservoir. CMG internally

sets pressure at standard condition (pstd) equal to 14.7 psia or 101.325 kPa and temperature at standard condition (tstd) equal to 60.0 deg F or 15.56 deg C by default. The CO_2 density according to National Institute of Standards and Technology (NIST) at standard conditions is 1.87 kg/m^3. Injection pressures were limited to the reservoir's constraints, and boundary conditions were adjusted using volume modifiers in CMG to extend the boundaries to estimated regional boundaries. Table 8 summarizes the fluid properties for the injection zone. The brine salinity is at 116000 ppm, 0.116 kg/l, the CO_2 viscosity at initial condition is 618 kg/m^3, and water viscosity is 0.39 cp, the initial pressure (psi) is 2790 psi, and the reservoir temperature is at 163 °F.

Table 8: Fluid Properties

CO_2 Density	**Brine salinity at the in-zone**	**CO_2 Viscosity (cp)**	**Water Viscosity (cp)**	**Initial Pressure (psi)**	**Reservoir Temperature (°F)**
618 kg/m^3 at initial condition	2 mol/kg = 116000 ppm	0.049	0.39	2790	163

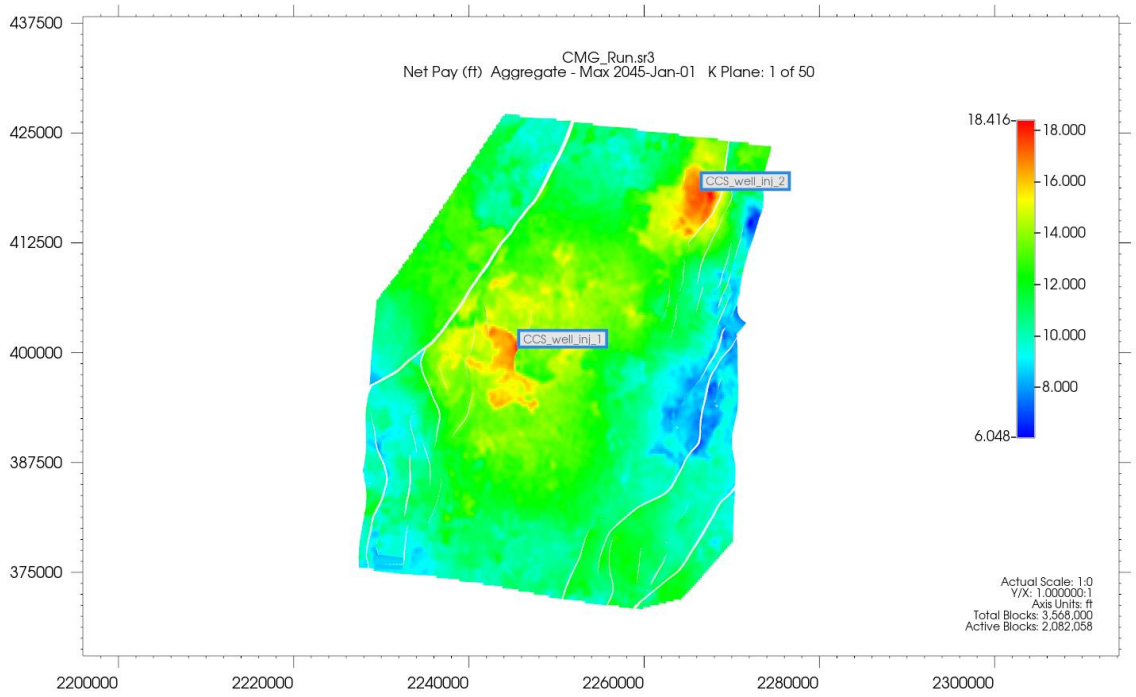

Figure 43: Net pay map showing bullseyes where the CCS injection wells were placed

For each well, perforations were made along different layers of the model, over 20 years:

- Layers 34–49 were perforated and injected during the first 10 years, then shut in.
- Layers 18–33 were perforated and injected during years 10–15, then shut in.
- Layers 2–17 were perforated and injected during the last 5 years.

The maximum allowable injection pressures were calculated using Equation (8), considering a fracture gradient of 0.7 psi/ft and 90% of the fracture pressure. Table 9 shows these values for the two injection wells. This is visualized in the plot as the gas rate in the green line and the well BHP in the blue line. The maximum allowable pressure for CCS_well_Inj_1 is 4496 psi corresponding to the fracture gradient of 0.7 psi/ft and 90%

of the fracture pressure, same approach for CCS_well_Inj_2 where the maximum allowable pressure is calculated to be at 4435 psi. These values are shown in Table 9.

$$P_{\max inj} = Avg.Depth \times 0.7\frac{psi}{ft} \times 90\% \quad (8)$$

Where, $P_{\max inj}$ is the maximum allowable injection pressure (psi), $Avg.Depth$Is the average depth of the target injection zone measured in ft, 0.7 is the fracture gradient and 90% is the factor of fracture gradient pressure to avoid exceeding the formation's fracture pressure.

Table 9: Maximum injection pressure for CCS_well_Inj_1 and CCS_well_Inj_2.

Injection Well	**Fracture Gradient**	**Subsurface Average Depth (ft)**	**Calculated Maximum Injection Pressure (psi) (90% of Fracture Gradient)**
CCS_well_Inj_1	0.7	7136	4496
CCS_well_Inj_2	0.7	6917	4358

The cumulative CO_2 and injection rate behaviors over the 20-year simulation period are shown in Figures 45 and 46. Variations in perforation layers led to non-linear cumulative CO_2 trends, with injection rates adjusted over time. For simplification, iteration tolerance was increased to allow the simulation to converge, given the low permeability values. Fifteen simulation realizations were modeled, each with varying variogram ranges to evaluate reservoir heterogeneity. Due to challenges with very low-porosity realizations, these simulations could not be completed and we assume those capacity values will be way

below the target volumes. The gas rate and the BHP follow the same behavior because of the perforation layers (Figure 45). For the first ten years of injection, the well begins injecting at a rate of 4e+06 ft^3/day, or 211.33 tCO_2/day then stops and returns injecting at a lower than increasing rate to 4.5e+06 ft^3/day, or 238.29 tCO_2/day for the following five years then stops and injects back to 6.24+06 ft^3/day, or 330.42 tCO_2/day. Figure 46 also shows the base case where the red lines represent the three scenarios of the base case varying in variogram range. The cumulative gas ranges from 1.74 $MtCO_2$ to 2.66 $MtCO_2$ after 20 years.

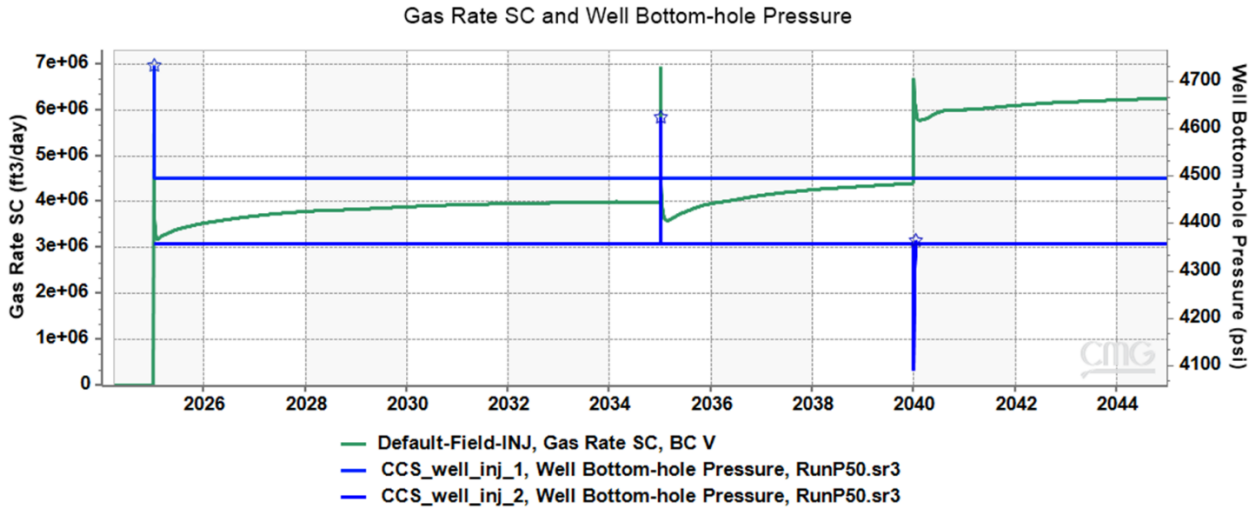

Figure 44: CO_2 Rate at the standard condition and Well Bottom-hole Pressure for the base case with data analytics (BC V). CCS_well_Inj_1 is set at 4496 psi and CCS_well_Inj_2 is at 4358 psi with different perforation layers.

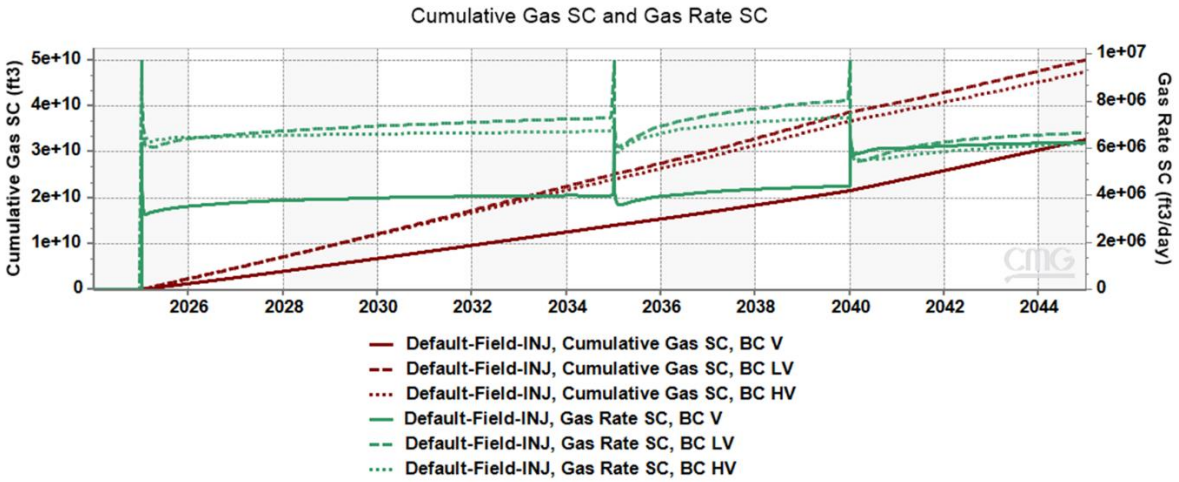

Figure 45: Cumulative CO_2 in red and CO_2 Rate in green at standard conditions for the base case scenarios in data analytics (low, base, high variogram values). The reason why the cumulative CO_2 is not a straight linear line is due to the different perforation layers, injecting at 4e+06 ft^3/day for the first ten years, then at 4.5e+06 ft^3/day for the five years, then at to 6.24+06 ft^3/day for the last five years of the injection period

4.2 Simulation Results And Discussion

The CO_2 plume distribution after 20 years is illustrated in Figure 47, with the two injection wells highlighted. The faults are in purple in south west direction. These faults are considered minor and not critical to the simulation study.

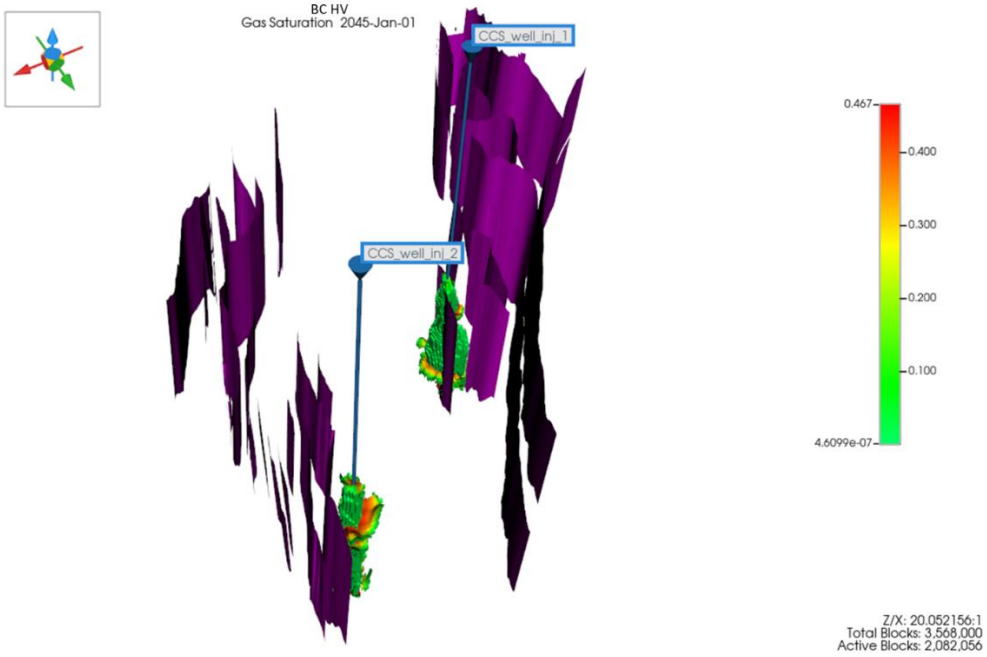

Figure 46: CO_2 plume model after 20 years. The plume is touching the minor faults that are considered not critical to the storage capacity and would not impact leakage for the study. The bar legend indicates the CO_2 saturation.

4.2.1 Area of Review Delineation

The AoR is defined as the region surrounding a GCS project where underground sources of drinking water (USDWs) may be at risk due to injection activities (EPA, 2013). For Class VI CO_2 wells, the AoR is critical to ensure the protection of underground sources of drinking water (EPA, 2013; UIC, 2010). The AoR is delineated using computational modeling that considers the physical and chemical properties of all phases of the injected CO_2 stream, and displaced formation fluids based on available site characterization, monitoring, and operational data (EPA, 2013). The AoR in the simulation study was defined by the combination of the CO_2 plume with a gas saturation greater than 1% and pressure front with a critical pressure (Pc) above 77 psi. The map in Figure 48 shows the

AoR of all 15 realizations after running the simulations for 20 years, observing how the AoR changes with each realization.

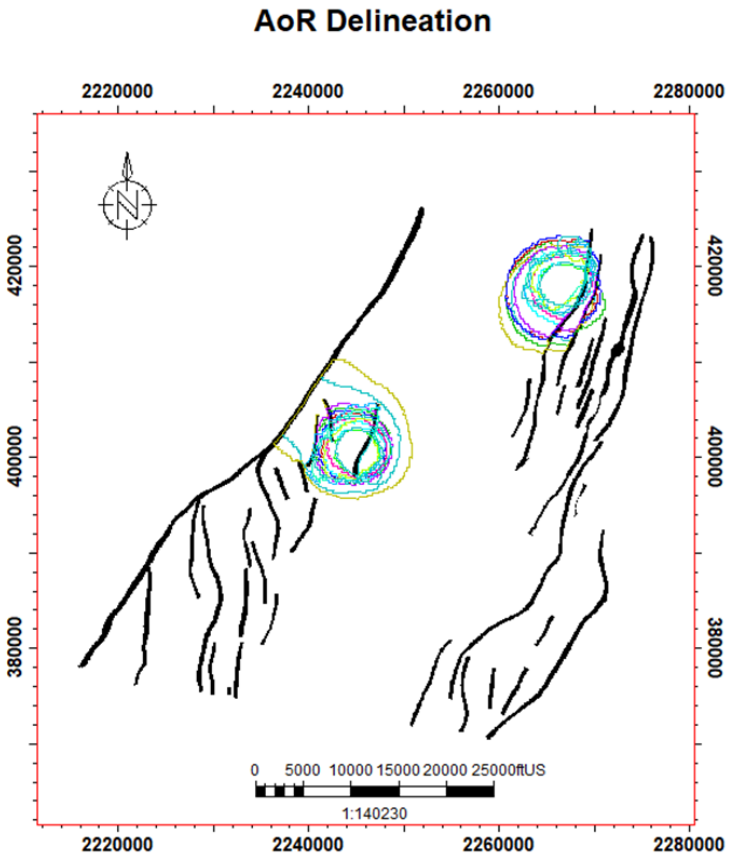

Figure 47: AoR delineation for all 15 realizations

The area of the different AoRs is shown in Table 10 where we later use the acreage to account for the cost of land lease in the value of information calculations in Chapter 5. Figure 49 shows the results of the 15 realizations' total storage capacity output estimations. The results vary from 499 $ktCO_2$ to 3.78 $MtCO_2$. The most sensitive input or parameter

that affects the storage capacity, in this case, is the porosity and reservoir quality heterogeneity of the reservoir. These scenarios are defined earlier in Chapter 3.

Table 10: The outcomes of the AoR definitions in acre and SQFT for each realization

Realization (Ri)	AoR (Acre)	AoR (SQFT)
R1	5144	224055216
R2	3118	135837504
R3	3950	172044576
R4	1187	51718788
R5	2630	114558444
R6	2819	122791284
R7	770	33557317
R8	1306	56893716
R9	794	34598837
R10	1847	80452706
R11	1519	66156314
R12	1146	49938491
R13	1902	82836310
R14	2583	112531162
R15	1389	60524006

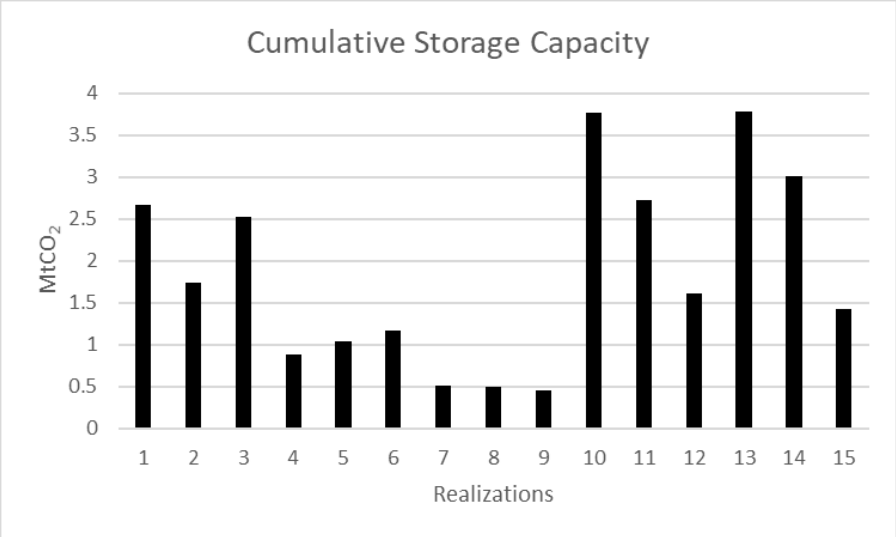

Figure 48: The outcomes of the cumulative storage capacity in tCO_2 for each realization for 20 years (total of 15 realizations)

Chapter 5: Value of Information

5.1 VOI CASE

The fourteen legacy wells in the storage site provide historical data such as well logs, which can be repurposed for updated analyses in the pre-CO_2 injection phase of the project. Three out of the fourteen wells show better well log quality, specifically porosity which was considered for petrophysical analysis, stochastic modeling, and simulations to estimate storage capacity. A hypothetical Direct Air Capture (DAC) operator would evaluate the potential for a CO_2 storage site. The operator's goal is to store 1 $MtCO_2$ over 20 years, motivated by the 45Q tax credit market offering $180 per tCO_2. The DAC operator wants to know the value of drilling a stratigraphic well to get a class VI permit in this challenging geological carbon storage site. The decision maker is faced with two alternatives, i.e., drill a stratigraphic well or not drilling any well. We identified two possible scenarios faced by the operator:

- SC1 = the targeted interval can store 1 $MtCO_2$ for 20 years
- $SC1^c$ = the target interval fails to store 1 $MtCO_2$

In the flowing analysis, further details will be explained and discussed about the decision situation faced by the operator. Suppose a company needs to choose between different alternatives, but there is some uncertainty involved. After the uncertainty is observed and an option is selected, the company gains some benefit. Before getting any information, the company's initial beliefs about the uncertainty are shown by the probability distribution ***p(x).*** now, suppose the company can collect more information before deciding to sign the contract. This additional information is represented by a likelihood probability ***p(y|x)***, which shows the conditional probability between the new information ***y*** and the uncertainty ***x***.

5.2 DECISION ANALYSIS

In decision analysis, one of the effective diagrams is the influence or relevance diagram to illustrate the relationship between the distinction of interest and the observed distinction (Howard & Matheson, 2005). For this study, the distinction interest is the amount of tCO_2 (>1$MtCO_2$) that the storage site can store, and the observed distinction is the stratigraphic well test results of storage capacity estimations. The arrow in the influence diagrams (Figure 50 and Figure 51) indicates the relevance or influence (Howard & Matheson, 2005) between the distinction interest and the observed distinction, and this is called the *assessed form* where we begin with a prior probability distribution over the distinction of interest as shown in Figure 50. The conditional probability of the observed data given the distinction of interest is called the *likelihood.* In Figure 51, the reversed arrow signifies the *inferential form* of the probability distribution assigned to the distinction of interest once the observed data is known. This updated distribution is known as the *posterior,* as it is utilized following the acquisition of results from modeling or simulation assessments. The probability distribution representing the anticipated observations in the study prior to data collection is termed the *preposterior.* This represents Bayes' theorem application.

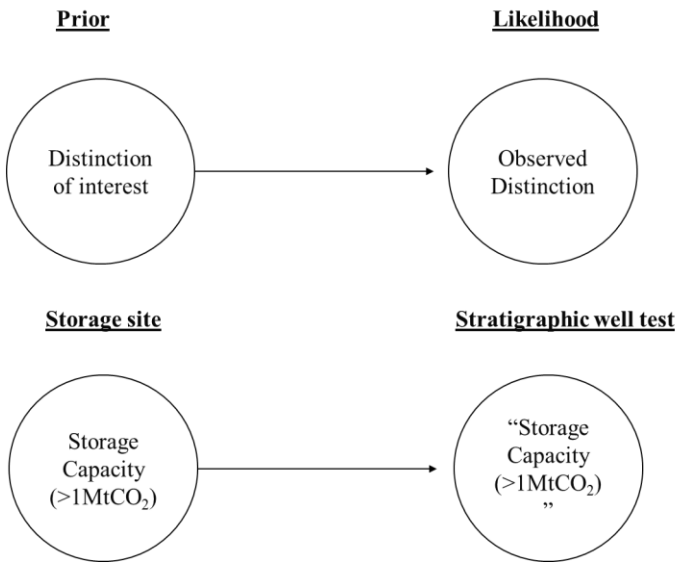

Figure 49: The influence diagram (or relevance) in the assessed form (prior belief)

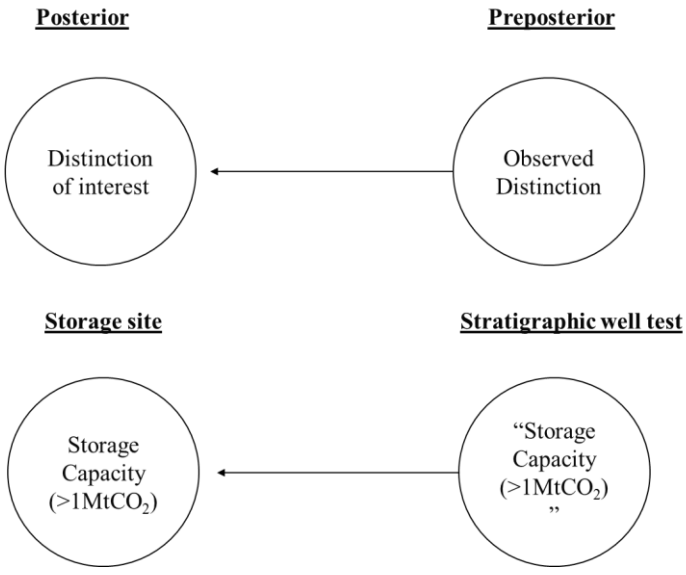

Figure 50: The influence diagram (or relevance) in the inferential form (posterior)

5.3 VALUE OF STRATIGRAPHIC WELL INFORMATION (VOI):

5.3.1 Prior Value

As explained in the previous chapters, 15 realizations were modeled stochastically and exported for simulations in CMG software to obtain the storage capacity estimations. To quantify the probability of the storage site storing the operator's goal of 1 $MtCO_2$, a statistical analysis, bootstrapping sampling with replacement (Efron & Tibshirani, 1985), was assessed to recalculate uncertainty in a calculated statistic from the 15-sample realizations itself. After getting the normal distribution of the means of the outcomes and the standard deviation of the sample data (Figure 52). Prior belief about the uncertainty is ***p(SC1)*** = 73.33%, ***p(SC1^c)*** = 26.67%. This information represents the prior beliefs in the assessed form and it is shown in the probability tree in Figure 53.

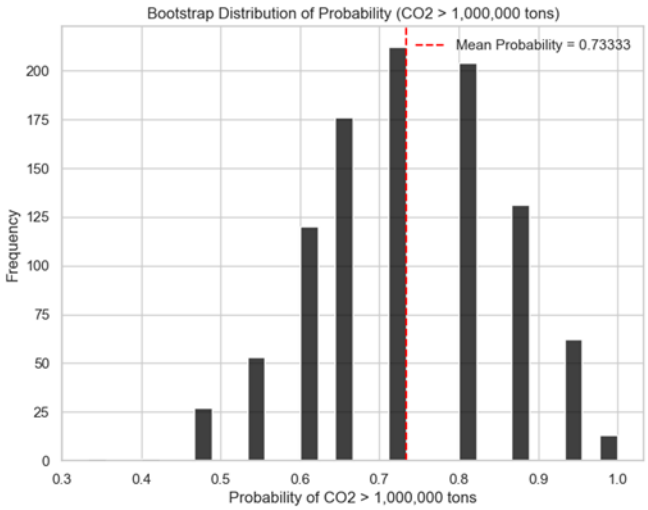

Figure 51: Bootstrap distribution of the 15 realizations (storage capacity predictions)

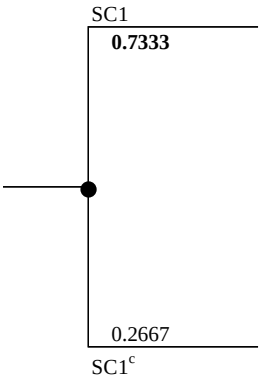

Figure 52: Prior probability (without additional information) of the storage capacity greater than 1MtCO_2. The circle represents uncertainty

The outcomes of drilling stratigraphic well will generate a profit or loss (NPV) for the DAC operator. The NPV is a function of the average amount of CO_2 above 1MtCO_2 and the price of carbon credit per MtCO_2 (\$/MtCO_2) minus the CAPEX and OPEX and the cost of land. Since the project is capture and sequester, the carbon price according to EPA, and current DAC operators with renewable energy to power DAC is through the 45Q tax credit of 180 \$/tCO_2. The cost of land is assumed with a price of \$2,400 per acreage according to current appraisal district prices. In addition, according to the recent data from Energy Information Administration (EIA), the latest commercial electricity rate in Texas is 9.14 cent per kWh. The average energy consumed for a DAC project through the grid is assumed around 1100 kWh/tCO_2. The cost of drilling deep stratigraphic well is assumed based on the historical production appraisals, which is around \$1 to \$3 Million.

NPV Assumptions:

- CAPEX:
    - Based on the scale of 1-billion-dollar capex for 1 MtCO_2 captured

- Cost of land is a function of the average AoR acreage calculated (above a cumulative average of 1MtCO_2 for 20 years) and the price is assumed based on cost of land per acre in Texas
- OPEX:
  - Assuming the energy consumption of the DAC operator is through green energy assuming a lot of wind development in south Texas. The main energy consumption is through the grid
- The full-time operational employment is 30 and a wage of $54k per employee per year
- Revenue:
  - Carbon price based on the 45Q tax credit

The decision maker obtains no value if the contract is not signed and earns a sure zero. While the NPV for the specific storage site studied with a storage capacity of greater than 1MtCO_2 (SC1) is $29.59M. Alternatively, the NPV is -$17.53M when the storage capacity is not greater than 1 MtCO_2 (SC1^c). Assuming the decision maker is risk neutral, which is often a valid assumption in value of information (Bickel, 2006), who goes for the maximum expected value between the alternatives of "Develop" or "Not Develop", the expected value (EV) of "Develop" is $17.02M ($29.59*0.7333-$17.53*0.2667), the expected value of "Not Develop" is 0. Since the EV is greater than 0, hence the storage formation is feasible for DAC project. The DAC operator's decision without drilling

stratigraphic wells can be represented with the decision tree in Figure 54. The rectangular represents decision, and the circle represents a probability of the uncertainty.

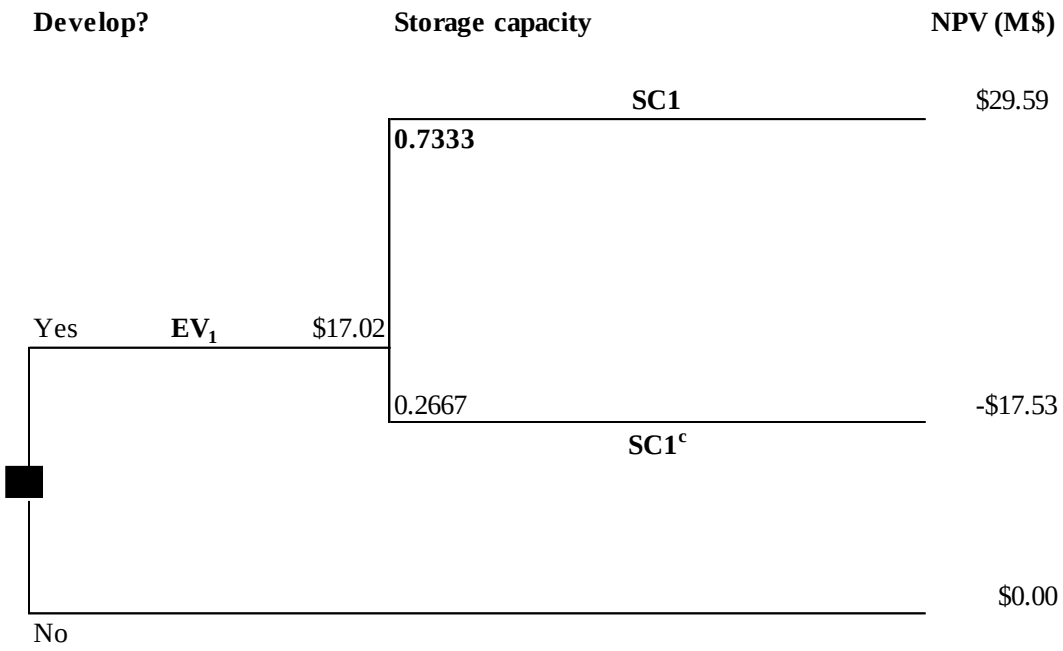

Figure 53: Decision tree without stratigraphic well (VOI). The rectangular represents decision, and the circle represents uncertainty.

5.4 VALUE OF PERFECT INFORMATION (VOPI)

5.4.1 Posterior Value (The Value with Stratigraphic Well)

Now, the question remains should the operator pay for a stratigraphic well as per Class VI permit? The operator wants to evaluate the value of drilling stratigraphic well to reduce geological uncertainty. The most the operator should be willing to pay for drilling stratigraphic well is the value with perfect information. Since the operator is risk neutral, in general we can say the value with perfect information, is equal to the difference between

the expected value with perfect information (EV_2) and the expected value without perfect information (EV_1) (Bratvold et al. 2007) as shown below.

$$VOPI = [EV\ with\ perfect\ information - EV\ without\ perfect\ information]$$

Suppose the decision maker knew the storage site could store higher than 1MtCO_2 for certain, since the probability of SC1 is 73.33% and the test is perfect, meaning if SC1 will occur the test will report that with certainty, then the probability the test will report SC1, ***p("SC1")***, is also 73.33% and they would drill and earn $29.59M. If they knew the storage site could not have that storage capacity, 26.67% they would not have to drill the stratigraphic well. The VOPI probability tree can be illustrated in Figure 55.

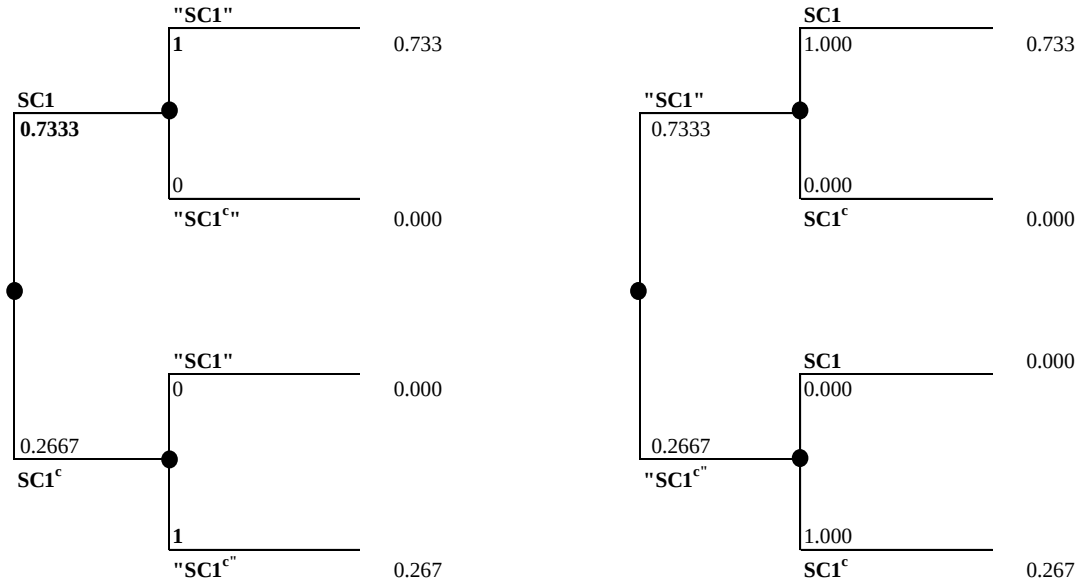

Figure 54: Information gathering relevance (VOPI)

Hence, the value with perfect information is $21.70M (0.7333*$29.59M), and therefore perfect information is worth $4.68M. Any tests higher than this value is not worth the cost. This decision situation faced by the operator is illustrated in Figure 56.

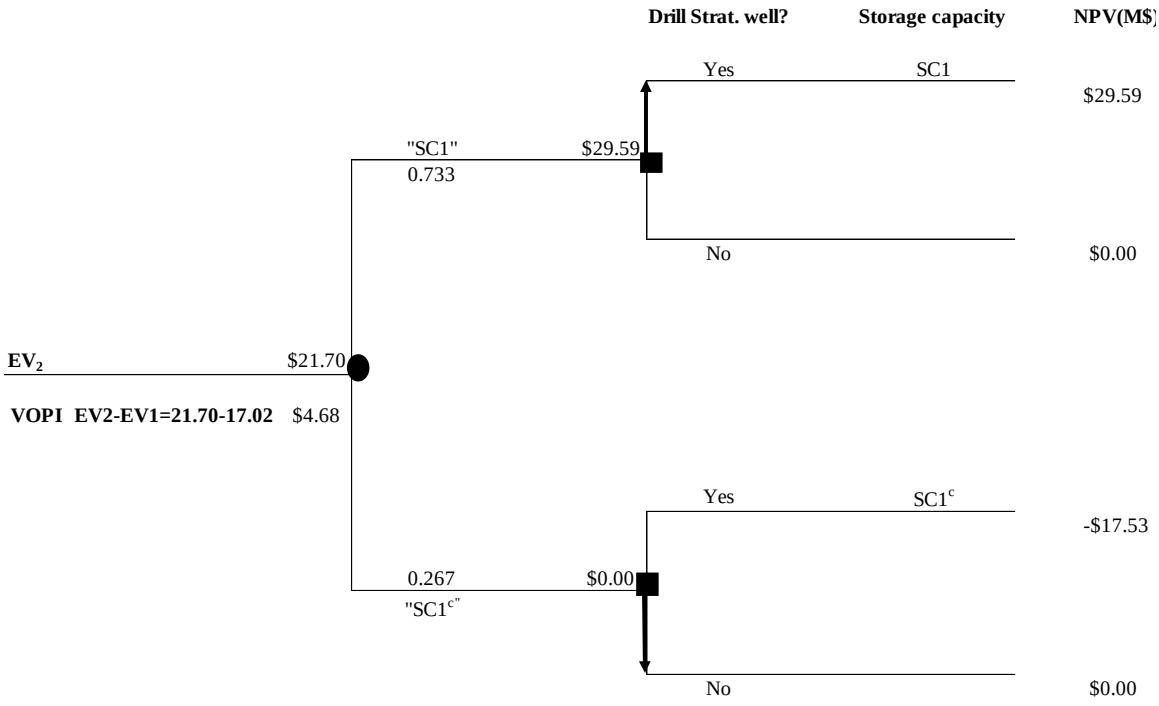

Figure 55: Decision tree of value of perfect information (VOPI)

Obtaining perfect information is very rare and does not happen in the real world, however the value with perfect information is useful for the decision maker as it set the upper boundary limit for any imperfect information gathering activity.

The VOPI is the most the decision maker should pay. Any information-gathering activity beyond this value is worthless and not economic. Hence, exploring the Value of Imperfect Information (VOII) is worthwhile and essential in the VOI analysis.

5.5 VALUE OF IMPERFECT INFORMATION

Now, assuming the operator can further obtain information about the target formation with a well test. Assume the accuracy of the test is 90%. The preposterior probability is as follows:

$$p("SC1") = p("SC1"|SC1)p(SC1) = 0.9 \bullet 0.7333 + 0.1 \bullet 0.2667 = 0.69$$

$$p("SC1^c") = p("SC1^c"|SC1^c)p(SC1^c) = 0.1 \bullet 0.7333 + 0.9 \bullet 0.2667 = 0.31$$

Or

$$p("SC1^c") = 1 - p("SC1") = 0.31$$

The posterior probabilities for different outcomes of uncertainty *SC1* given the different outcomes of *"SC1"* is as follows:

$$p(SC1|"SC1") = \frac{p("SC1"|SC1)p(SC1)}{p("SC1")} = \frac{0.9 \bullet 0.7333}{0.69} = 0.961$$

$$p(SC1^c|"SC1") = 1 - p(SC1|"SC1") = 0.039$$

The probability tree of the above analysis is illustrated in Figure 57

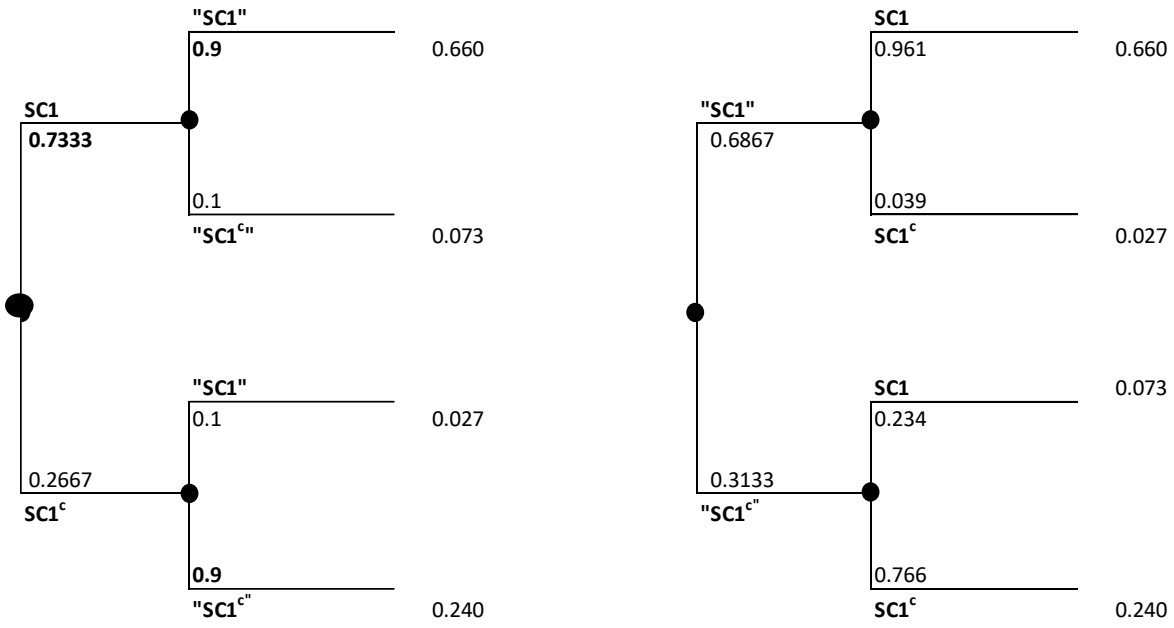

Figure 56: Probability tree of storage capacity

The posterior values with stratigraphic well give the degree of accuracy of the performance of the well test is as follows;

(0.961*29.59) + (0.039*-17.53) = $27.78 and (0.234*29.59) + (0.766*-17.53) = - $6.50

The posterior value (the value with stratigraphic well) is $19.08 (27.78*0.69 + 0*0.31). Hence, the value of the stratigraphic well is $2.05M ($19.08M – $17.02M). Now, the operator should perform the test with a 90% accuracy if the cost is less than $2.05M. Figure 58 illustrates the decision analysis above with the stratigraphic well test.

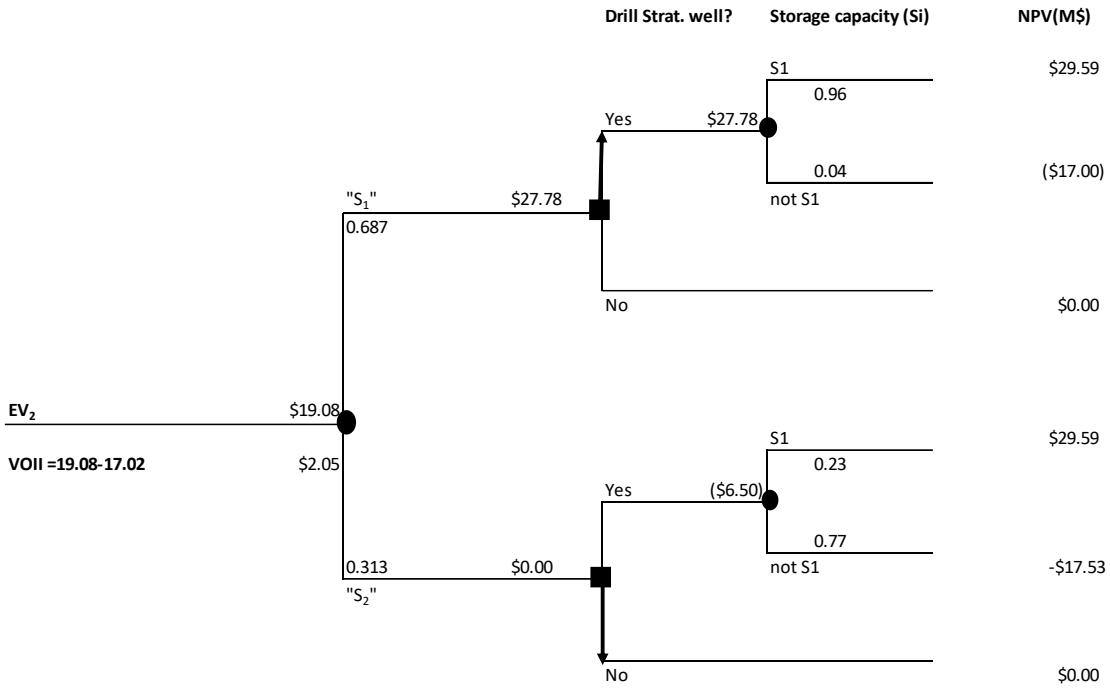

Figure 57: Decision tree with value of imperfect information (VOII)

5.6 SENSITIVITY ANALYSIS

Figure 59 plots the VOI against the accuracy test. In the operator's situation, he/she should not buy information with a test of 80% accuracy. Accuracy below 80%, the VOI is zero. Meaning it cannot add any value to the decision situation.

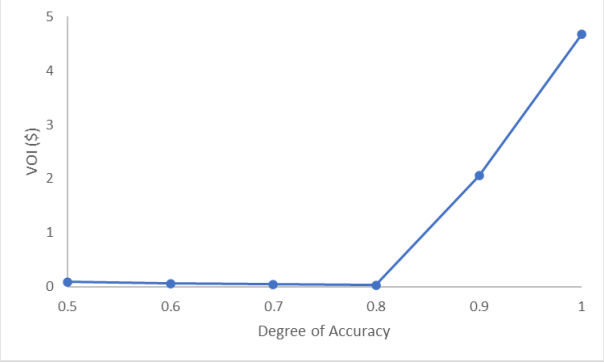

Figure 58: Sensitivity of operator's VOI to Test Accuracy for the storage capacity

Chapter 6: Discussion and Future Work

6.1 VALUE OF INFORMATION (VOI)

This study aims to determine whether drilling stratigraphic wells in a low-quality reservoir is worthwhile for a DAC operator involved in a Geological Carbon Storage (GCS) project. Specifically, the key question addressed: What is the value of drilling stratigraphic wells in a low-quality reservoir? VOI analysis for this research involves a total of 15 realizations, each examining how porosity distribution affects storage estimates by varying theoretical variogram range and porosity based on standard deviation. Scenarios consider whether the site can store 1 $MtCO_2$ over 20 years, from a single storage unit.

Given the assumption the DAC operator is risk-neutral, then the notion of value of perfect information (VOPI) is applicable, and the VOI study is implemented to use the application for a GCS project and have it useful for future studies. The analysis focuses on the Value of Perfect Information, representing the maximum that should be paid for information. This focus helps establish a "buying price" (Bratvold et al., 2009) for drilling stratigraphic wells, ensuring that drilling is considered only if the cost is below this value for the DAC operator. The value with perfect information is $21.70M and therefore perfect information is worth $4.68M. Any tests higher than this value is not worth the cost. The posterior value of the decision situation with imperfect information is $19.08M, hence the company should perform the test with a 90% accuracy if the cost is less than $2.05M. The study is tailored to a specific storage site and injection period, indicating that results might differ for other sites or times. This study is to demonstrate the VOI application and steps that is needed to be taken. The current VOI analysis concentrates exclusively on the value of drilling the stratigraphic wells, excluding other information-gathering activities such as core samples, and formation testing. This would require additional geological

characterization, modeling, and assessments for the VOI study (Bratvold et al., 2009) and understanding the degree of accuracy for each of the tests to account for multiple uncertainties and more complex analysis for a VOI study. Enhancing the analysis could include a sensitivity analysis to identify which variables most significantly impact the NPV outcomes, recognizing these factors like the energy consumption costs and carbon pricing could greatly influence these results. In addition, the time value of money was ignored to demonstrate the VOI application. Future work should incorporate discounting to reflect how costs and benefits change over time, providing a more accurate economic assessment. The decision tree and influence diagram would even get bigger to display the decision analysis. Future directions for VOI analysis involve exploring the value of imperfect information, which reduces but does not eliminate uncertainty, providing a more realistic assessment.

6.2 Site Characterization and Modeling

In this project, the lithology analysis was based on GR and SP logs cut off to set reservoir or non-reservoir. The reservoir rock is sandstone, and the non-reservoir is siltstone and shale. The practice in petrophysics is to calculate Vclay. There are no cores in the AOI to calibrate any facies assemblage or to calibrate the Vclay parameter, hence the petrophysical modeling was run without facies. Saying this, future work could be considered to carry on with further facies characterization and modeling. In addition, more petrophysical analysis is recommended for further assessment, for example well log calibration and normalization, density and neutron correction, and calculation of new porosity. Also, creating models with different (better) poro-perm transform since there were no cores in the AOI. It is important to add the deeper zones for characterization, geomodeling and simulation. In addition, I started the project with a time-depth conversion

to generate the static modeling for the porosity and permeability to export them for dynamic modeling, which is an extra effort into the research workflow.

To mitigate the major geological risks, it is recommended to perform additional studies, such as core analysis to estimate porosity, permeability, and capillary pressure, as well as 3D seismic interpretation of the total storage window to better define the structure, seismic facies, and the boundary conditions of the reservoir compartment. The initial plan was to characterize the full-storage window (about 2900 to 4200 ft) including running amplitude analysis in Paleoscan on several seismic horizons in the model, however this analysis is still not conclusive due to the amount of noise in the seismic. The full storage section (Figure 8) was considered to provide an overview of the total storage capacity of the site. Due to time constraints, only one zone was targeted for detailed evaluation, that is the interval between Frio Top and Frio FS1 marker (called Upper Frio zone). This research focused on the Upper Frio zone, so a feasibility study for a GCS site would have some limitations since it does not consider the total section for storage. Adding the deeper zones could change the economics of the project, where the synclinal area (Figure 7), south of the defined AoRs (Figure 48) is, also, a potential site for a CO_2 sequestration project.

Future work should consider studying the whole storage window, so more storage capacity is added, to better justify any investment in stratigraphic wells. This upper Frio zone was selected as an analog from a nearby field that we believed could represent similar properties; however, after petrophysical analysis and static modeling the interval showed significant differences in porosity and sand presence (poorer reservoir properties than the analog field). In addition, the analysis was based on three wells with porosity logs and applied to three main cases. The analysis could be expanded to characterize the deeper zones, and compare with the current target zone (Upper Frio). As for the uncertainty analysis, the number of realizations was a total of 15 for storage capacity outcomes, future

simulations could include the remaining excluded 6 (the low values of porosity and variogram ranges).

Chapter 7: Conclusions and Recommendations

Based on the assumptions outlined in this study, our analysis for this specific site recommends drilling a stratigraphic well with an expected value of $4.68 million, as determined by the Value of Perfect Information (VOPI). Stratigraphic wells and associated data collection activities that exceed this value are not economically justified. This Value of Information (VOI) analysis provides a framework for assessing the economic viability of drilling stratigraphic wells in low-quality reservoirs for DAC operators involved in GCS projects. The analysis indicates that drilling a stratigraphic well is advisable as long as the drilling cost remains below the VOPI threshold. While relying solely on VOPI may be idealistic, it establishes a clear benchmark for making informed investment decisions. Additionally, the evaluation of value with imperfect information underscores the importance of test accuracy; performing tests with at least 80% accuracy adds value for this specific study to the decision-making process. Although this study is site-specific and time-specific, the same VOI analysis can be applied to include the deeper layers of the Frio formation since the focus was on one interval. Also, the same framework can be applied for other relevant data, for example, the value of 3D seismic or 2D lines in the study area. Future research can expand the analysis to enhance its applicability, thereby supporting more effective and efficient GCS projects. Future recommendations could consider well placing as an extension to the study. Optimizing well placement is crucial for refining variogram estimates due to the scarcity of the data in the area, particularly the nugget and sill, which determine spatial correlation and model variance. Strategically placing new wells at distances that challenge existing nugget estimates enhances confidence in the variogram, leading to a more constrained and accurate geological model. Avoiding redundant drilling close to existing wells ensures that each new well provides valuable

information, thereby improving the model's reliability in estimating storage capacity. Addressing challenges with sparse well distribution through strategic placement and uncertainty management ultimately leads to better-informed decision-making and more robust geological assessments.

Appendices

APPENDIX A

The **Advanced velocity model** dialog box in Petrel. The advanced velocity model requires the following input: (Chapter 2.2)

1. Name. Set a name for future velocity model.
2. Type of conversion. For example, from TWT to Z.
3. Datum (Z=0). The elevation reference point (SRD or Other) must be set.
4. One or more zone descriptions. For example, a set of surfaces in two-way time.
5. A definition of the velocity model for each zone. For example, V=Vint.
6. Input parameters for the velocity model. For example, a surface of Vint.
7. Correction data, if required. For example, well tops for the specified zones.

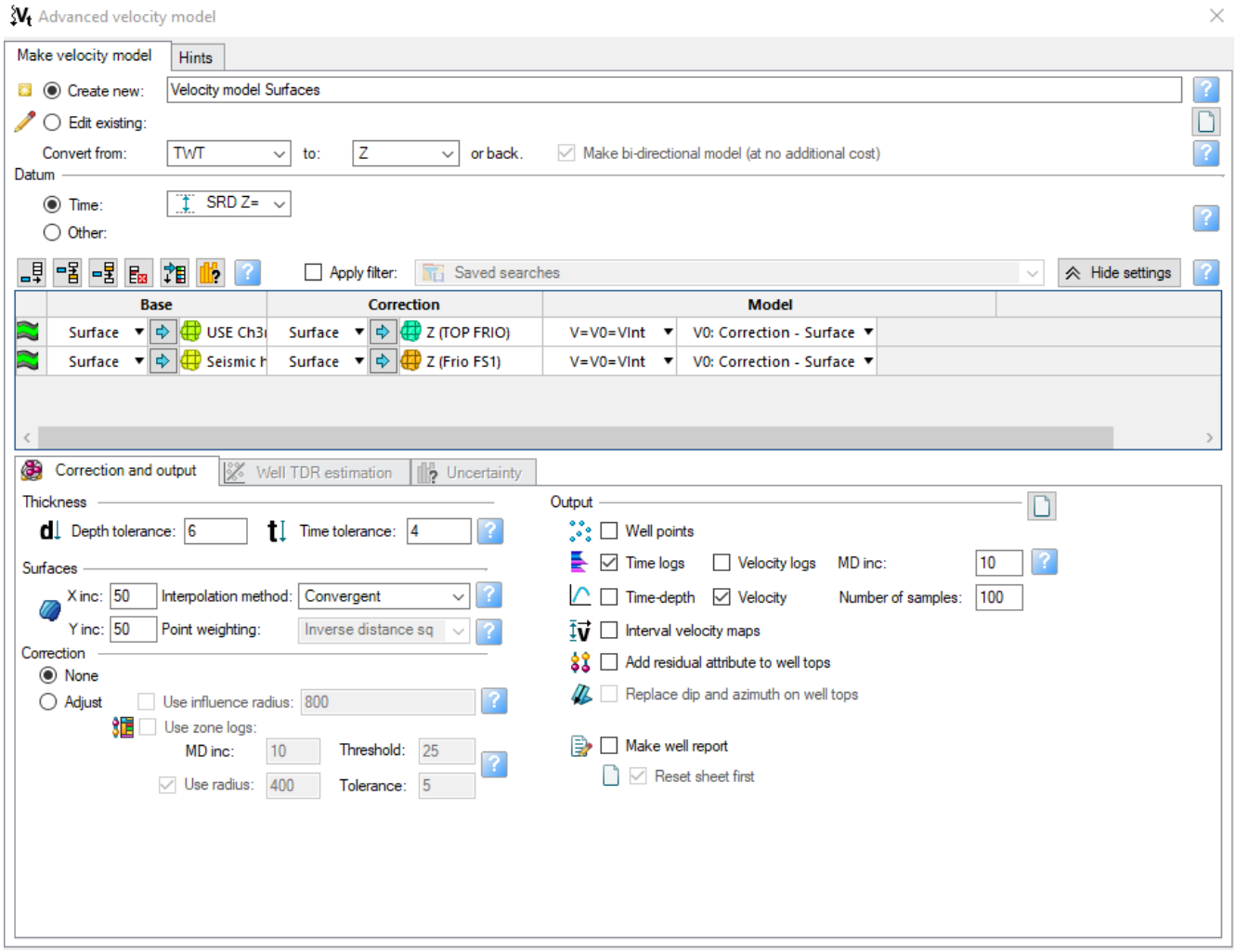

APPENDIX B

Porosity-Permeability transform from literature that were also tested for the project but not used.

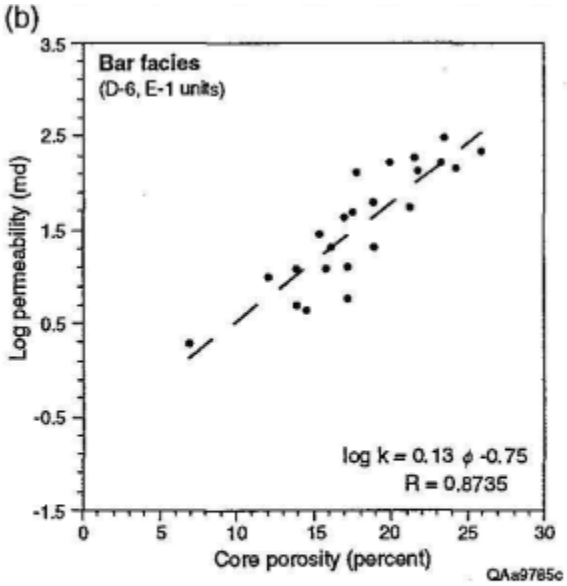

Figure 28. Cross plots reveal different porosity–permeability relationships for the two primary reservoir facies: (a) channel facies and (b) bar facies.

From Chapter 2.4: Porosity-Permeability transform adapted from (McRae et al., 1995)

APPENDIX C

Results of the fault truncation and QC. Some faults in the west were truncated to the main regional fault.

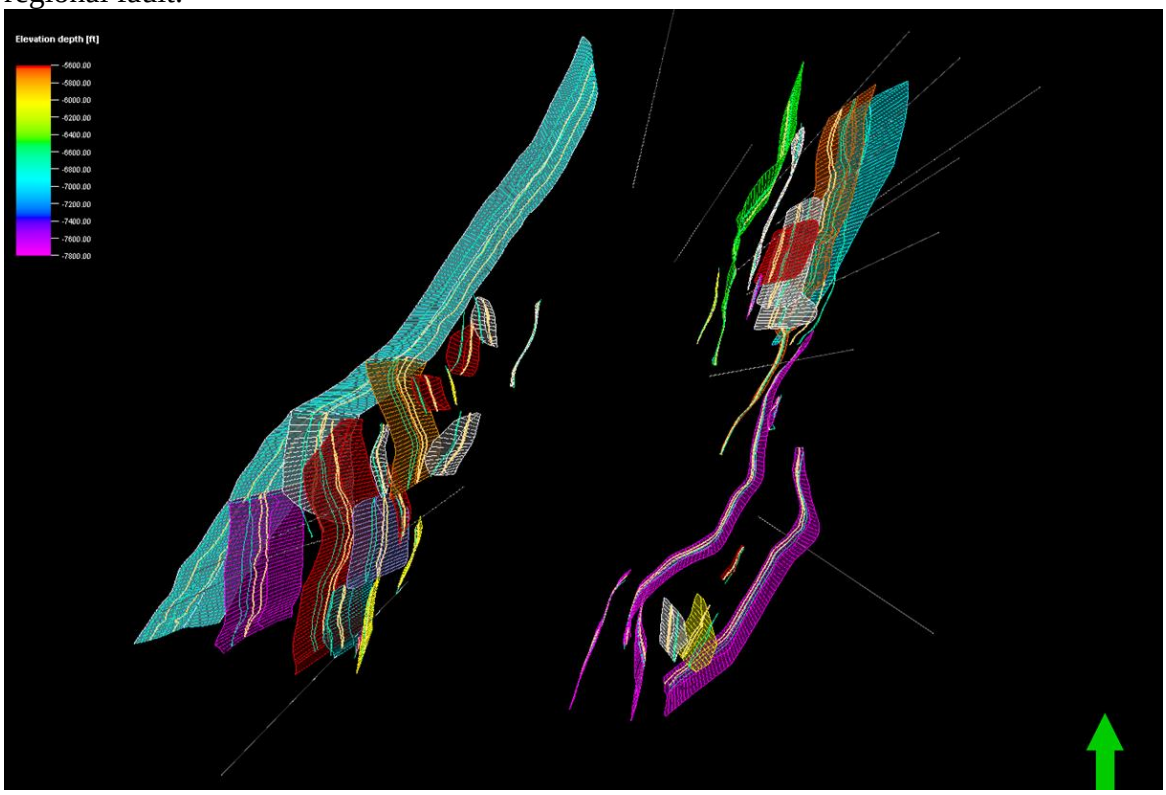

From chapter 2.4: reservoir quality analysis (Faults QC)

APPENDIX D

From Chapter 3.2:The histogram distributions of high and low porosity models according to their standard deviation (Y-axis is the frequency, x-axis is the porosity; red bar is the input well log, green bar is the upscaled porosity, & purple bar is the property (porosity) modeled)

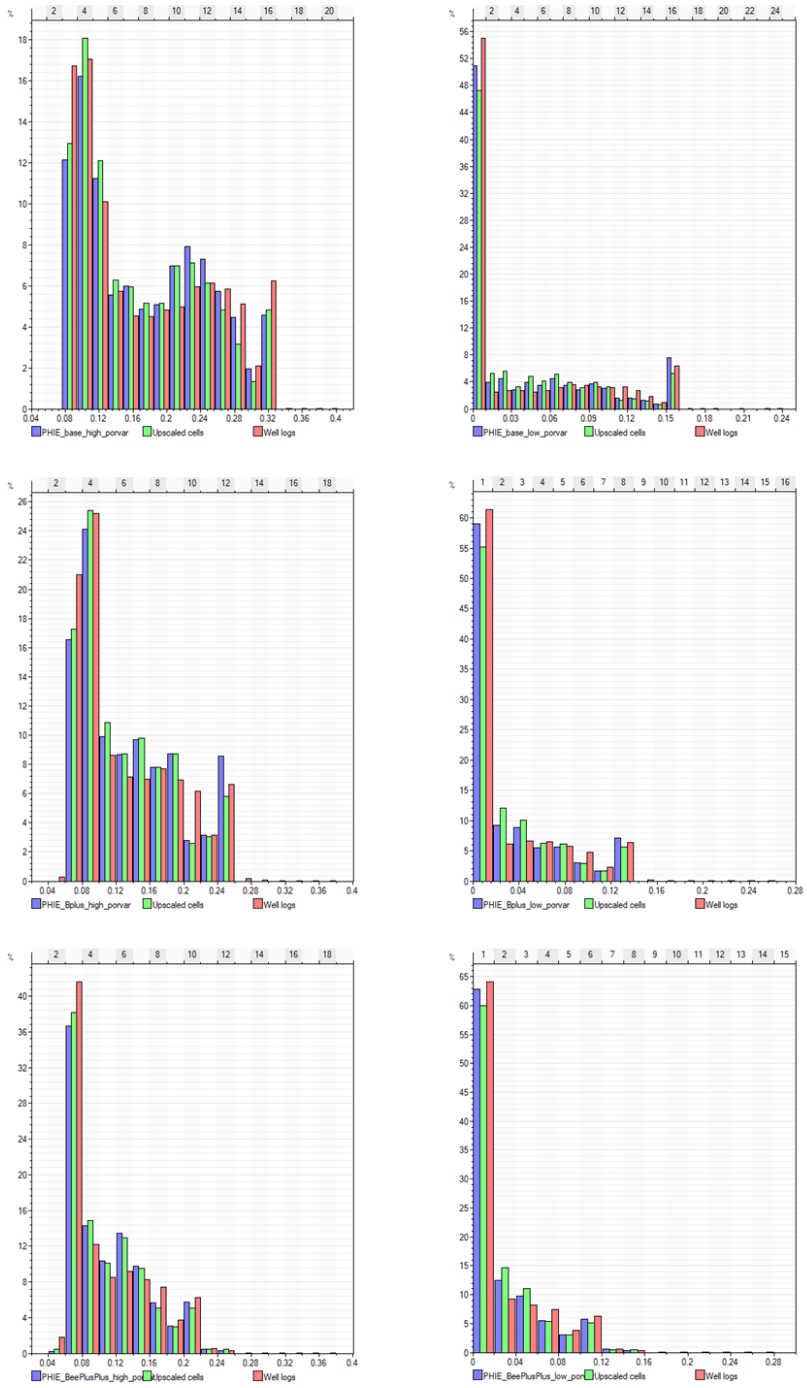

From Chapter 3.2: The histogram results of combined data analysis and high and low porosity (Y-axis is the frequency, x-axis is the porosity; red bar is the input well log, green bar is the upscaled porosity, & purple bar is the property (porosity) modeled)

References

Allen, R., Nilsen, H. M., Lie, K.-A., Møyner, O., & Andersen, O. (2018). Using simplified methods to explore the impact of parameter uncertainty on CO2 storage estimates with application to the Norwegian Continental Shelf. *International Journal of Greenhouse Gas Control*, *75*, 198–213. https://doi.org/10.1016/j.ijggc.2018.05.017

Bear, J. (1979). *Hydraulics of Groundwater* (1st ed.). London ; New York : McGraw-Hill International Book Co., c1979.

Bhuyan, K., & Passey, Q. R. (1994). *CLAY ESTIMATION FROM GR AND NEUTRON - DENSITY POROSITY LOGS*.

Bickel, J. E. (2006). Some Determinants of Corporate Risk Aversion. *Decision Analysis*, *3*(4), 233–251. https://doi.org/10.1287/deca.1060.0080

Bickel, J. E. (2015). *QUANTIFYING THE BENEFIT OF CCS MONITORING AND VERIFICATION TECHNOLOGIES*.

Bonnaffé, F. L., Hammes, U., Carr, D. L., & Brown, F. L. (2008). *High-Resolution Sequence Stratigraphic Correlations of the Oligocene Frio Formation in South Texas*.

Bratvold, R. B., Bickel, J. E., & Lohne, P. H. (2009). *Value of Information in the Oil and Gas Industry: Past, Present, and Future*.

Brown, L. F., Loucks, R. G., Treviño, R. H., & Hammes, U. (2004). Understanding growth-faulted, intraslope subbasins by applying sequence-stratigraphic principles: Examples from the south Texas Oligocene Frio Formation. *AAPG Bulletin*, *88*(11), 1501–1522. https://doi.org/10.1306/07010404023

Dommisse, R. (2024). Constraining faults and stratigraphic zones in shale and tight oil basins via 3D geocellular models. *Geoenergy Science and Engineering*, *240*, 212991. https://doi.org/10.1016/j.geoen.2024.212991

Dual Challenge, C. C. (2021). *Meeting the Dual Challenge, A Roadmap to At-Scale Deployment of CARBON CAPTURE, USE, AND STORAGE, CHAPTER SEVEN-CO2 GEOLOGIC STORAGE*.

Efron, B., & Tibshirani, R. (1985). *THE BOOTSTRAP METHOD FOR ASSESSING STATISTICAL ACCURACY*.

Eidsvik, J. (with Mukerji, T., & Bhattacharjya, D.). (2015). *Value of Information in the Earth Sciences: Integrating Spatial Modeling and Decision Analysis*. Cambridge University Press.

Elvaretta, S. (2021). *Value of Information Analysis in CO2 Sequestration Projects*. University of Stavanger.

EPA. (2013). *Geologic Sequestration of Carbon Dioxide: Underground Injection Control (UIC) Program Class VI Well Site Characterization Guidance*.

Galloway, W. E. (1977). *Catahoula Formation of the Texas Coastal Plain: Depositional Systems, Composition, Structural Development, Ground-Water Flow History, and Uranium Distribution*. Bureau of Economic Geology, The University of Texas at Austin.

Hammes, U., Loucks, R., Treviño, R., & Brown, F. J. (2006). Fault compartmentalization of stacked sandstone reservoirs in growth-faulted subbasins: Oligocene Frio Formation, Red Fish Bay area, South Texas, in R. Slatt, ed., Reservoir characterization: Integrating technology: Proceedings of the 26th Annual Gulf Coast Section of the Society of Economic Paleontologists and Mineralogists Foundation Bob. *Bob F. Perkins Research Conference*, 631–650.

Hosseini, S. A., Ershadnia, R., Lun, L., Morgan, S., Bennett, M., Skrivanos, C., Li, B., Soltanian, M. R., Pawar, R., & Hovorka, S. D. (2024). Dynamic modeling of geological carbon storage in aquifers – workflows and practices. *International Journal of Greenhouse Gas Control*, *138*, 104235. https://doi.org/10.1016/j.ijggc.2024.104235

Howard, R. A., & Matheson, J. E. (2005). Influence Diagrams. *Decision Analysis*, *2*(3), 127–143. https://doi.org/10.1287/deca.1050.0020

IPCC, Calvin, K., Dasgupta, D., Krinner, G., Mukherji, A., Thorne, P. W., Trisos, C., Romero, J., Aldunce, P., Barrett, K., Blanco, G., Cheung, W. W. L., Connors, S., Denton, F., Diongue-Niang, A., Dodman, D., Garschagen, M., Geden, O., Hayward, B., … Péan, C. (2023). *IPCC, 2023: Climate Change 2023: Synthesis Report. Contribution of Working Groups I, II and III to the Sixth Assessment Report of the Intergovernmental Panel on Climate Change [Core Writing Team, H. Lee and J. Romero (eds.)]. IPCC, Geneva, Switzerland.* (First). Intergovernmental Panel on Climate Change (IPCC). https://doi.org/10.59327/IPCC/AR6-9789291691647

Kukal, G. C., & Hill, R. E. (1986). Log Analysis of Clay Volume: An Evaluation of Techniques and Assumptions Used in An Upper Cretaceous Sand-Shale Sequence. *SPWLA TWENTY-SEVENTH ANNUAL LOGGING SYMPOSIUM*.

McRae, L., Holtz, M., & Hentz, T. (1995). *Strategies for reservoir characterization and identification of incremental recovery opportunities in mature reservoirs in Frio Fluvial-Deltaic sandstones, south Texas: An example from Rincon Field, Starr County. Topical report* (DOE/BC/14959--15, 123238; p. DOE/BC/14959--15, 123238). https://doi.org/10.2172/123238

Moore, W. R., Ma, Y. Z., & La Pointe, P. R. (2011). Uncertainty Analysis in Well-Log and Petrophysical Interpretations. In *Uncertainty Analysis and Reservoir Modeling* (pp. 17–28). American Association of Petroleum Geologists. https://doi.org/10.1306/13301405M963478

Peters, E. J. (2012). *Advanced Petrophysics: Geology, porosity, absolute permeability, heterogeneity, and geostatistics*. Live Oak Book Company.

Piava, M., Lupinacci, W., Freire, A., & HansFord, J. (2019). Comparison of methodologies to estimate the clay content – A case study in the Roncador Field, Campos Basin. *Proceedings of the 16th International Congress of the Brazilian Geophysical Society&Expogef*, 1–5. https://doi.org/10.22564/16cisbgf2019.091

Puerta-Ortega, C., Bickel, J. E., & Hovorka, S. (2013). Assessing the value of permeability data in a carbon capture and storage project. *International Journal of Greenhouse Gas Control*, *17*, 523–533. https://doi.org/10.1016/j.ijggc.2013.06.003

Rider, M. H. (1996). *The Geological Interpretation of Well Logs / Malcolm Rider* (2nd ed.). Gulf Publishing.

Sato, K. (2011). Value of information analysis for adequate monitoring of carbon dioxide storage in geological reservoirs under uncertainty. *International Journal of Greenhouse Gas Control*, *5*(5), 1294–1302. https://doi.org/10.1016/j.ijggc.2011.07.010

Satti, H. W., Khan, T., Mahmood, M. F., Manzoor, U., Hussain, M., & Malik, M. B. (2024). Enhancing Reservoir Characterization With High-Resolution Lithofacies Prediction Using Advanced Feature Engineering and Ensemble Classifiers. *Petrophysics - The SPWLA Journal of Formation Evaluation and Reservoir Description*, *65*(05), 813–834. https://doi.org/10.30632/PJV65N5-2024a9

Snedden, J. W., & Galloway, W. E. (2019). *The Gulf of Mexico Sedimentary Basin*. Cambridge University Press.

UIC. (2010). *Title 40 CFR Part 124, 144, 145, 146, and 147: Federal Requirements Under the Underground Injection Control (UIC) Program for Carbon Dioxide (CO2) Geologic Sequestration (GS) Wells*.

Wyllie, M. R. J., Gregory, A. R., & Gardner, L. W. (1956). ELASTIC WAVE VELOCITIES IN HETEROGENEOUS AND POROUS MEDIA. *GEOPHYSICS*, *21*(1), 41–70. https://doi.org/10.1190/1.1438217